

ALMA MATER STUDIORUM · UNIVERSITÀ DI BOLOGNA

---

---

FACOLTÀ DI SCIENZE MATEMATICHE, FISICHE E NATURALI  
DOTTORATO DI RICERCA IN FISICA, XXV CICLO  
Settore Concorsuale di afferenza 02/A1  
Settore Scientifico Disciplinare FIS/04 - Fisica Nucleare e Subnucleare

**Measurement of  $K(892)^{*0}$  resonance  
production in Pb–Pb collisions  
with the ALICE experiment at the LHC**

**Dr.ssa Francesca Bellini**

Coordinatore Dottorato:  
Prof.  
**Fabio Ortolani**

Relatore:  
Chiar.ma.Prof.ssa  
**Luisa Cifarelli**

---

---

**Esame Finale anno 2013**



# Contents

<b>Introduction</b>	<b>1</b>
<b>1 The Quark-Gluon Plasma and heavy-ion collisions</b>	<b>3</b>
1.1 The QCD phase transition . . . . .	4
1.2 The “Little Bang” at the LHC . . . . .	9
1.2.1 Global event properties . . . . .	12
1.2.2 Identified particle spectra and ratios . . . . .	13
1.2.3 Anisotropic flow . . . . .	18
1.3 Resonance production in heavy-ion collisions . . . . .	20
1.3.1 $\phi(1020)$ and $K^*(892)$ production in pp collisions at the LHC	24
1.3.2 $\phi(1020)$ and $K^*(892)$ production in Pb–Pb collisions at LHC	26
<b>2 A Large Ion Collider Experiment at the LHC</b>	<b>31</b>
2.1 The Large Hadron Collider . . . . .	31
2.1.1 The injection chain . . . . .	34
2.1.2 The LHC as heavy-ion accelerator . . . . .	35
2.1.3 LHC operations . . . . .	36
2.2 The ALICE detector . . . . .	38
2.2.1 The Inner Tracking System . . . . .	41
2.2.2 The Time Projection Chamber . . . . .	43
2.2.3 The Transition Radiation Detector . . . . .	46
2.2.4 The Time Of Flight . . . . .	46
2.2.5 V0, ZDC and T0 . . . . .	47
2.2.6 Muon spectrometer . . . . .	49
2.3 ALICE online operations . . . . .	49
2.3.1 Data AcQuisition system . . . . .	49
2.3.2 Data Quality Monitoring online . . . . .	52
2.4 ALICE offline computing . . . . .	56
<b>3 The ALICE Time-Of-Flight detector</b>	<b>61</b>
3.1 The Time Of Flight detector . . . . .	62
3.1.1 The Multigap Resistive Plate Chambers . . . . .	64
3.1.2 The Front-End Electronics . . . . .	68

3.1.3	The readout electronics . . . . .	70
3.2	TOF data quality monitoring online . . . . .	72
3.2.1	The TOF signal . . . . .	73
3.2.2	Monitoring the TOF readout status . . . . .	75
3.2.3	Electronics noise monitoring . . . . .	79
<b>4</b>	<b>TOF data quality assurance, performance and PID</b>	<b>81</b>
4.1	Strategy for calibration and QA . . . . .	82
4.2	The TOF matching efficiency . . . . .	84
4.3	Determination of the interaction time . . . . .	92
4.4	Particle identification performance . . . . .	96
<b>5</b>	<b>Measurement of <math>K^{*0}</math> production in Pb–Pb collisions</b>	<b>103</b>
5.1	$K^{*0}$ reconstruction in Pb–Pb collisions . . . . .	103
5.1.1	Data sample and event selection . . . . .	104
5.1.2	Track selection . . . . .	106
5.1.3	Particle identification with Time Of Flight . . . . .	108
5.1.4	Signal extraction . . . . .	112
5.1.5	Invariant mass fit . . . . .	114
5.2	Efficiency correction . . . . .	116
5.3	Systematic uncertainty on the yields . . . . .	120
5.3.1	Systematic effects related to the yield extraction procedure	120
5.3.2	Systematic effects related to the background . . . . .	122
5.4	$K^{*0}$ transverse momentum spectra . . . . .	125
	<b>Conclusions</b>	<b>135</b>
	<b>Bibliografia</b>	<b>137</b>

# Introduction

This thesis reports a measurement of the  $K^{*0}$  resonance production in Pb–Pb collisions at  $\sqrt{s_{NN}} = 2.76$  TeV. The decay channel  $K^{*0} \rightarrow K^\pm \pi^\mp$  is reconstructed in the ALICE detector through the identification of the resonance decay products by the Time-Of-Flight system.

Quantum Chromo Dynamics (QCD), the theory of strong interactions between coloured charges, is very well known in its perturbative regime, but still not fully understood in the non-perturbative domain, that is the playground of two of the most important characteristics of hadronic matter: the generation of hadron masses and the confinement. The gluon self-coupling described by QCD is responsible for the asymptotic freedom of the interaction and confinement. At high momentum transfer the theory is asymptotically free, meaning that the coupling between partons is very small, but when low momentum is exchanged a strong potential keeps quarks and gluons confined into hadrons. Although the QCD properties provide good arguments for confinement, there is yet no rigorous proof why this is a property of the strongly interacting matter.

The most recent experimental breakthrough at the LHC seem to have brought new insights in the Higgs sector, where elementary particles acquire mass by coupling with the Higgs boson(s), and quarks among them (via Yukawa's coupling). Still, the sum of the constituent quark masses does not account for the 95% of the hadron mass, that instead appears to be generated dynamically by strong interaction inside the hadrons.

A phase transition between the ordinary nuclear and hadronic matter to a deconfined state, named Quark-Gluon Plasma (QGP), has been predicted on the basis of thermodynamical considerations and QCD calculations. According to the hot Big Bang model of cosmology such a transition must have occurred also in the primordial expanding Universe, where after the electro-weak phase transition, the initial deconfined partons plasma would have reached the hadronic phase about  $1\mu s$  after the Big Bang. The study of the QCD phase transition is therefore necessary to solve the open puzzle of the onset of confinement and the hadron masses. This is done experimentally with ultra-relativistic heavy-ion collisions, where the energy density and temperature reached may be sufficient to form the QGP. During the last two years, these studies have been addressed by the ALICE experiment at the Large Hadron Collider (LHC), where the experimental conditions are favourable to the formation of the deconfined phase. The LHC has been operating since late

2009, delivering pp collisions at several center-of-mass energies ( $\sqrt{s} = 0.9, 2.76, 7$  and  $8 \text{ TeV}$ ) and Pb–Pb collisions at  $\sqrt{s_{\text{NN}}} = 2.76 \text{ TeV}$ . Since then, ALICE has been collecting data and provided information on the properties of the produced medium through the measurement of several observables.

The first chapter of this thesis begins with a review of the properties of the expected phase transition and continues with a selection of the most recent results on particle production in heavy ion collisions at the LHC. The focus is on ALICE studies of the medium properties through the measurement of “soft” observables, such as  $\pi$ , K, p and resonances spectra, flow and strangeness enhancement. The last section of the chapter is dedicated to resonance production studies, as tools to investigate different stages of the medium evolution. The  $K^{*0}$  is a short-lived resonance, whose lifetime is comparable to that of the partonic medium at the LHC. Resonances produced in the neighbourhood of the phase transition may carry information about it, in particular about partial chiral symmetry restoration that is believed to occur nearly the transition from confined to deconfined hadronic matter. Resonances such as the  $K^{*0}$  decay long before reaching the detector, therefore only the reconstruction of their decay channel allows the measurement of their yields and properties. The properties of the produced resonances are accessible in the final state depending on their initial momentum: low momentum resonances have larger probability of undergoing re-scattering and regeneration during the hadronic medium expanding phase, resulting in some loss of information, while intermediate and high- $p_t$  reconstructed particles can be directly used to study partonic medium effects.

After a brief introduction on the LHC, the ALICE experiment is presented in the second chapter. The detector design and performance are discussed, as well as some details of the online and offline operations.

The third chapter is entirely dedicated to the description of Time-Of-Flight (TOF) detector layout and electronics. TOF plays a very important role in ALICE due to its particle identification (PID) capabilities, that allow a  $2\sigma$  separation of  $\pi$  from K and K from p up to  $3.0 \text{ GeV}/c$  and  $4.5 \text{ GeV}/c$  respectively. TOF PID is well suited to be exploited in the resonance analysis, especially for studying the  $K^{*0}$  production through the decay channel  $K^{*0} \rightarrow K^\pm \pi^\mp$ , where kaon identification is crucial. The performance of the TOF system are presented in the fourth chapter, where all the ingredients needed to ensure the required PID performance are discussed in detail.

The last chapter illustrates the study of the  $K^{*0}$  production in Pb–Pb collisions at the LHC, through the  $K^{*0} \rightarrow K^\pm \pi^\mp$  channel, where the decay products are identified by TOF. In the chapter, the resonance reconstruction strategy is described: the raw yields are extracted with an invariant mass analysis and then corrected for selection and reconstruction efficiencies and for detector acceptance. A study of the systematic uncertainty is also presented. The measurement of the  $K^{*0}$  yield is finally shown as function of the resonance transverse momentum and of the centrality of the collision.

# Chapter 1

## The Quark-Gluon Plasma and heavy-ion collisions

The Quantum Chromo Dynamics (QCD) is the theory of the strong interactions between partons, that is responsible for the confinement of quarks inside hadrons and nucleons inside nuclei. Thermodynamic considerations and QCD calculations suggest that strongly interacting matter can exist in different phases, depending on the temperature and the density of the system. A phase transition characterised by a specific critical temperature and baryo-chemical potential brings a system of deconfined quarks and gluons into a state where partons are confined inside hadrons. Confinement is intimately related to the appearance of hadron masses, that are generated dynamically by strong interaction inside the hadrons. Despite the very accurate knowledge of the perturbative regime of QCD, the non-perturbative domain is still not fully understood, and so are confinement and the generation of the hadron masses. The phase transition between the ordinary nuclear matter and the deconfined Quark-Gluon Plasma (QGP) is briefly discussed in section 1.1.

The QCD phase transition can be investigated in laboratory by reproducing the temperature, pressure and energy density conditions that lead to the QGP formation by means of ultra-relativistic heavy-ion collisions. Nucleus-Nucleus (A–A) collisions are followed by an high number of binary nucleon-nucleon collisions taking place in a very small spatial region, therefore providing enough energy density to allow the transition to the QGP state. Systems like those produced in A–A collisions, composed of many degrees of freedom and subject to a collective behaviour, can be described in their thermodynamic phase by equations of state. The product of the collision is a “fireball” in local thermal equilibrium that rapidly expands and cools down. If the collisional energy was sufficient for the QCD phase transition to deconfined matter to occur, the initial state is made of strongly interacting quarks and gluons that hadronise in the later medium expansion phases, when the system cools down below the critical temperature. The development of the fireball after heavy-ion collisions, although much faster, is believed to reproduce the evolution stages of the early Universe, when, after the electro-weak phase transition,

the partonic deconfined matter turned into confined hadrons, nearly  $1\mu\text{s}$  after the Big Bang. Because of this analogy, heavy-ion collisions are often referred to as the “Little Bang”. Heavy-ion collisions have been studied for more than 20 years at several collision energies. The early pioneers of this physics were the experiments started in 1990s at the AGS with heavy-ions (Au or Pb) colliding at a centre of mass energy  $\sqrt{s_{\text{NN}}}=4.6$  GeV per nucleon pair, and the fixed target experiments at the CERN SPS with  $\sqrt{s_{\text{NN}}}=17.2$  GeV (Pb or In). The Relativistic Heavy-Ion Collider (RHIC) at Brookhaven National Laboratory (BNL) was designed and started up in year 2000 to provide pp collisions, d–Au, Cu–Cu and Au–Au at several energies, up to  $\sqrt{s_{\text{NN}}}=200$  GeV for four dedicated experiments: PHENIX, STAR, BRAHMS and PHOBOS. At the Large Hadron Collider at CERN, where by machine design Pb–Pb ions can be accelerated to  $\sqrt{s_{\text{NN}}}=5.5$  TeV in addition to pp, the heavy-ion physics program is carried out by three experiments: ALICE entirely dedicated and optimised for Pb–Pb collisions study, ATLAS and CMS, with their multi-purpose detectors. The first Pb–Pb collisions were recorded in November 2010 at the LHC with an energy  $\sqrt{s_{\text{NN}}}=2.76$  TeV. More details on the LHC and the ALICE experiment will be given respectively in sections 2.1 and 2.2. The properties of the medium produced in heavy-ion collisions at the LHC are discussed in relation to the predicted behaviour and in comparison with the experiments at lower energies in section 1.2, where the most recent ALICE results are also reported. The conclusive section of the chapter is entirely dedicated to the study of resonances production as probe for the evolution stages of the medium and partial chiral symmetry restoration in the QGP.

## 1.1 The QCD phase transition

### Thermodynamics of QCD

Strongly interacting matter can exist in different phases characterized by given temperatures and densities, as summarised by the phase diagram of QCD (see fig. 1.1) in the plane of temperature ( $T$ ) and baryonic chemical potential ( $\mu_B$ ) [1].

The baryo-chemical potential is defined as the energy needed to increase of one unity the total number of baryons and anti-baryons in a system ( $N_B$ ),  $\mu_B=\partial E/\partial N_B$ , and it is introduced to consider that at relativistic energies the particle number in a system may not be conserved due to particle annihilation and creation processes at the microscopic level. Low temperatures and low baryo-chemical potential ( $\mu_B \sim m_p \sim 1$  GeV) in the diagram correspond to the nuclear matter in its ordinary state. By moving towards higher temperature (along the  $y$ -axis, on the left of the plot) or higher potential (along the  $x$ -axis in the lower part of the diagram) we reach a phase of hadronic gas (HG) where nucleons interact and form pions, resonances and other hadrons. The Stefan-Boltzmann law expresses the pressure of the hadronic gas as function of the temperature:

$$P_{\text{HG}} = g \frac{\pi^2}{90} T^4, \quad (1.1)$$

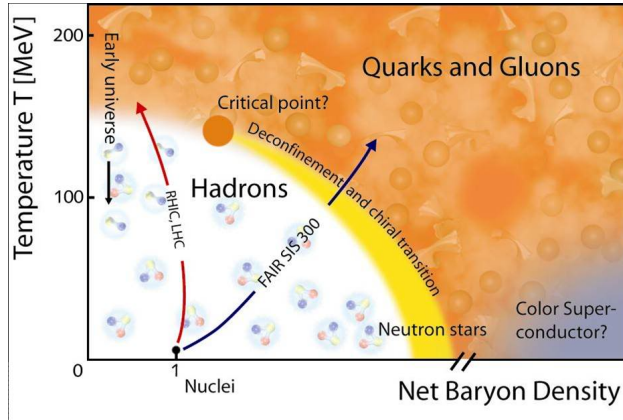


**Figure 1.1** Phase diagram of QCD.

where  $g$  is a factor that accounts for the degeneration of the system degrees of freedom. For a pion gas,  $g=3$ .

A deconfined phase of Quark Gluon Plasma is predicted to be reached by further increasing the temperature and the energy density, so that the partons interact without being confined anymore into hadrons. In the QGP, the number of degrees of freedom increases to include bosonic ( $2 \text{ spin} \times 8 \text{ colour states for gluons}$ ) and fermionic ( $3 \text{ colours} \times N_f \text{ flavours} \times 2 \text{ spin states}$ , to be multiplied by the phase-space factor  $7/4$  due to Fermi-Dirac statistics) degrees of freedom. The pressure can be expressed as

$$P_{QGP} = g \frac{\pi^2}{90} T^4 - \mathcal{B}, \quad \mathcal{B}^{1/4} \simeq 0.2 \text{ GeV}. \quad (1.2)$$

$\mathcal{B}$  is the *bag constant*, that acts as external pressure and is equivalent to some sort of latent heat defined as the difference in energy density per volumic unit between the two phases of the QCD matter.

For extreme values of  $\mu_B$ , nuclear matter should be in conditions of quark-colour superconductivity.

Neutron stars represent a case of very high baryonic density induced by the gravitational collapse of a star, for very low temperatures. In the Early Universe, the matter produced in the Big Bang evolved from very high temperature to hadronisation ( $T \sim 170 \text{ MeV}$ ) featuring only a small quark-antiquark excess of nearly  $10^{-9}$ , that is  $\mu_B \approx 0$ . In ultra-relativistic heavy ion-collisions at the LHC, the nuclear matter is heated and compressed enough in the collision to undergo the transition to QGP, still at low potential,  $\mu_B \sim 0$ .

The order of the phase transition is determined by how fast the free energy of the system varies in a neighborhood of the transition temperature. A first order transition happens with a discontinuous pattern in the first derivative of the free energy and it is accompanied by a discontinuous variation of entropy and the presence of

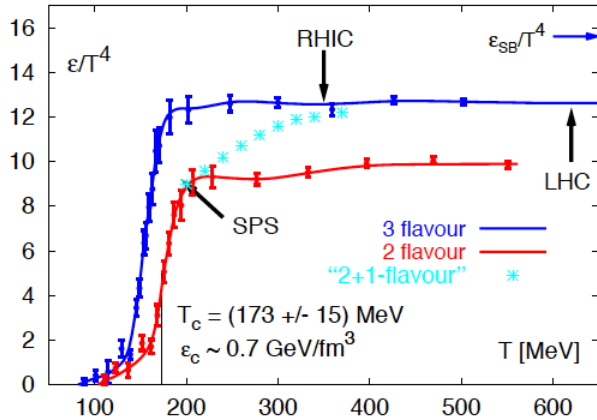


**Figure 1.2** Energy density in units of  $T^4$  as function of the temperature  $T$  from lattice QCD calculations. The three curves refer to different hypothesis on the number of degrees of freedom associated to light quark, that is 2, 2+1 or 3 light flavours [3].

latent heat. A second order transition is instead defined if the derivatives of higher than first order of the free energy are discontinuous. If a phase transition occurs without any fast modification of the parameters of the system, so with a continuous behaviour of the free energy and its derivatives, it is called a “crossover”. The QCD phase transition is supposed to be of the first order until the critical point is reached ( $200 \leq \mu_B \leq 500$  MeV). Critical points are the thermodynamical conditions in which the process becomes from first order to second order transition. Two states of matters can coexist at the critical point.

Lattice QCD calculations predict that the critical temperature at which a first order transition from hadronic gas to QGP can occur is  $T_c=(175\pm 15)$  MeV, corresponding to a critical energy density  $\epsilon_c \sim (0.3 \div 1.3)$  MeV/fm<sup>3</sup> [3]. The curves in fig. 1.2 show the energy density of the system as a function of its temperature from lattice calculation with  $\mu_B=0$  and for 2 and 3 light quarks considered, or with 2 lights and 1 heavier (strange quark). The “2+1” case should be the closest to the physically realized quark mass spectrum . The steep trend of this ratio reflects the increase of the degrees of freedom of the system when in the deconfined phase, as previously described.

### Chiral symmetry and the QCD vacuum

Beside the macroscopic or thermodynamical approach, the phase transitions can also be characterized at the microscopic level by changes in the symmetry of the system. In case a symmetry is broken in a phase transition, it may be necessary to introduce a new “order parameter” to describe the system and allow to identify the order of the transition.

Let's consider the Dirac equation for the u and d quarks represented by the  $q_i$  spinor,

$$(i\gamma^\mu \partial_\mu - m_i) q_i = 0, \quad (1.3)$$

the following expressions define two isospin currents,

$$\partial_\mu (\bar{u} \gamma^\mu d) = i(m_u - m_d) \bar{u} d \quad (1.4)$$

$$\partial_\mu (\bar{u} \gamma^\mu \gamma_5 d) = i(m_u + m_d) \bar{u} \gamma_5 d. \quad (1.5)$$

The first isospin current is conserved, as consequence of the fact that the QCD Lagrangian is invariant with respect to the SU(2) group. Another global symmetry also holds in the limit of massless quarks, represented by the following transformation:

$$q_i \rightarrow \exp(-i\alpha^i \frac{1}{2} \sigma^j \gamma_5) q_i \quad (1.6)$$

where the Pauli's matrices ( $\sigma^i$  have been introduced).  $m_u$  e  $m_d$  are the *current quark masses*. In such case the left-handed and right-handed components of the spinors decouple as  $q_{R,L} = (1 \pm \gamma_5)q$ . In the chiral limit, that is for  $m_q=0$ , the two  $q_{R,L}$  are conserved and associated to the  $SU(2)_L \times SU(2)_R$  symmetry of the Lagrangian, meaning that the number of left and right-handed quarks should be separately conserved in QCD. Because this degeneration is not seen in the hadrons hierarchy and quarks are massive particles, the chiral symmetry has to be spontaneously broken [6]. Massive quarks, indeed, can only be described as a superimposition of helicity eigenstates. Chiral symmetry breaking can occur via the dynamics of the theory itself.

The QCD vacuum ( $|0\rangle$ ) is considered to be unstable with respect the formation of a tightly bound  $q\bar{q}$  condensate. If we consider the field operators that create or destroy a quark when acting on a ket, respectively  $\bar{q}$  and  $q$ ,

$$\langle \bar{q}q \rangle = \langle 0 | \bar{q}_L q_R + \bar{q}_R q_L | 0 \rangle \neq 0. \quad (1.7)$$

Since neither  $|0\rangle$  is annihilated by  $q$ , nor  $\langle 0|$  by  $\bar{q}$ , the vacuum must contain  $q\bar{q}$  pairs. Only the sum of left and right-handed quarks is a conserved quantum number related to the symmetry, not the two separately. A left-handed quark, propagating through the vacuum can be annihilated by its anti-quark. The coupled anti right-handed quark of the vacuum can then create its anti-quark with the same momentum of the first.

With the spontaneous chiral symmetry breaking, a large value for the QCD vacuum is reflected into a large constituent mass with respect to the intrinsic mass of the quarks, due to the dynamical mass generation. The intrinsic masses of the constituent quarks in a proton (uud), for example are  $<20$  MeV/ $c^2$ , accounting for  $<6\%$  of the proton mass ( $\sim 1$  GeV/ $c^2$ ). The constituent mass of u and d quarks is of the order of 300 MeV, that of the strange quark is around 450 MeV. In the passage between the hadronic phase of the nuclear matter and the deconfined state, the chiral symmetry should be restored and with it, the independent conservation on

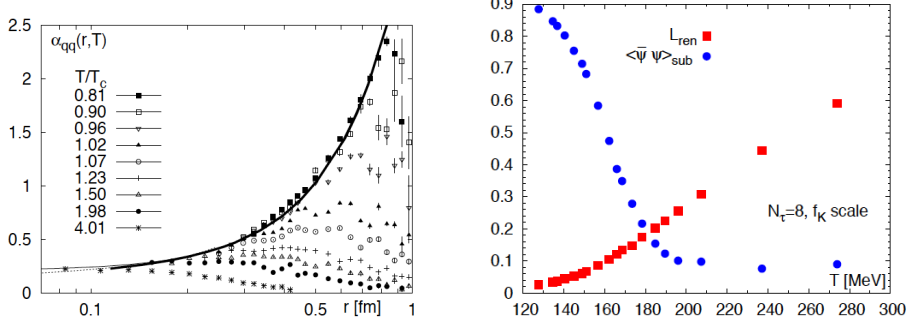


**Figure 1.3** On the left: coupling of the strong interaction as a function of the distance between two partons, for several values of the critical temperature of the system ( $T/T_c$ ) [4]. As the temperature increases, the coupling becomes smaller and seems to allow a transition to a deconfined state. On the right: reduced chiral condensate compared to the renormalised Polyakov loop as function of the temperature from lattice QCD calculations [5] for “2+1” quark flavours. The reduced chiral condensate is considered instead of  $\langle \bar{\psi} \psi \rangle$  to include the effect of the non-zero mass of the third quark. More details can be found in [5].

left and right-handed quarks. As quarks become deconfined, the light quark masses go back to the bare values,  $m_{u,d} \sim$  a few MeV/ $c^2$ ,  $m_s \sim 150$  MeV/ $c^2$ . This effect is usually referred to as “partial restoration of chiral symmetry”, because the masses do not go exactly to zero.

Two independent order parameters are associated to the QCD phase transition: the chiral condensate,  $\langle \bar{\psi} \psi \rangle$ , and the Polyakov loop,  $L(T)$ . The former refers to the chiral symmetry breaking (or restoration), the latter to confinement (or deconfinement). The Polyakov loop  $L(T)$  [7] is related to the free energy of quarks at large distances.

The interacting potential of quark-antiquark pairs as a function the radius of the hadrons from lattice QCD calculations is reported in fig. 1.3. The potential seems to decrease till zero values when the temperature increases, allowing a deconfined phase where partons are still interacting but not constraint within hadrons anymore. The critical temperature where this should happen is about  $T_c = 179$  MeV [4]. At low temperatures, when the quark potential energy,

$$V(r) \sim kr \left[ \frac{1 - e^{-\mu/r_D}}{\mu/r_D} \right] \rightarrow \infty \quad (1.8)$$

the Polyakov loop  $L(T) \rightarrow 0$  (confined phase). In the above equation  $k$  is the “string constant”, is expressed in energy density units ( $k \simeq 0.9$  GeV/fm), and  $r_D$  represents the Debye radius, that is the range of the effective force between the colour charges. At high temperatures,  $L(T)$  assumes finite values and so does the quark energy. The Polyakov loop is suited to discriminate between confined and deconfined phase.

Its dependence from temperature is compared by lattice QCD calculations with the analogous distribution of the chiral condensate in fig. 1.3 (right). The rapid decrease of the chiral condensate and the increase in the Polyakov loop happen in the same temperature region, suggesting that the passage between the confined and deconfined phase is also accompanied by a chiral transition [5]. The temperature range when this occurs is  $160 \leq T_c \leq 180$  MeV (from fig. 1.3), that is compatible with the temperature at which the interacting potential between quarks vanishes.

## 1.2 The “Little Bang” at the LHC

Heavy nuclei accelerated to ultra-relativistic energies appear as Lorentz contracted pancakes while travelling along the beam axis. Their transverse dimension is larger than longitudinal dimension, so that their collision can be considered as the superposition of binary nucleon-nucleon collisions. The nucleons that participate in the collisions are defined “participants” ( $N_{part}$ ) while those that do not interact are called “spectator” ( $N_{spect} = 2A - N_{part}$ ). The schematic picture of the collision as seen from the  $y - z$  plane and in the transverse  $x - y$  plane is reported in fig. 1.4.

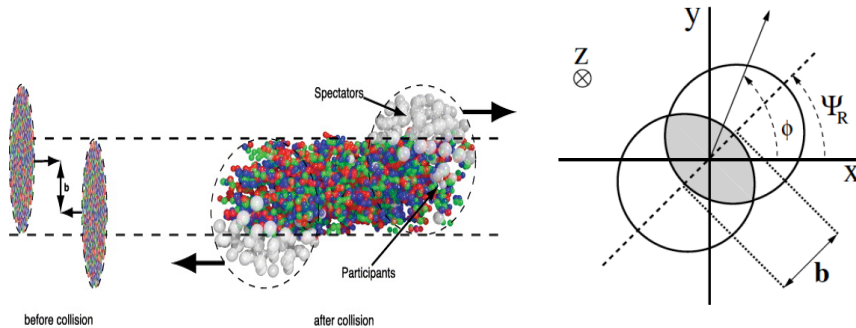


**Figure 1.4** Ultra-relativistic heavy ions collision as seen from the  $yz$  plane (left) and the transverse ( $xy$ ) plane.  $b$  is the impact parameter,  $\Psi_R$  is the reaction plane angle and  $\phi$  the generic azimuthal angle.

The impact parameter  $b$  is defined as the vector between the centres of the two nuclei in the transverse plane and quantifies the overlap region of the colliding nuclei. A central collision is characterized by a small impact parameter, the two nuclei collide almost head-on and almost all nucleons within the nucleus participate in the collision. As it will be shown later, the largest particle multiplicity is also produced. On the contrary, a peripheral collision has large impact parameter and only a few nucleons participate in the collision. Centrality is one of the main parameters that are used to characterise the collisions. Commonly, centrality classes are defined in terms of percentiles of the nucleus-nucleus hadronic cross section. Measuring centrality means determining the number of participant nucleons and spectators, that are needed to normalise the other measured observables prior to the comparison

with other collision systems (pp, for example). Centrality can be measured in two ways:

- a. from the correlation between centrality and the number of charged particles produced in the collision,
- b. from the measurement of the number of spectator nucleons that are not involved in the collision.

The first method relies on the choice of a geometrical model for the hadronic processes. Starting from the assumption that the impact parameter  $b$  is monotonically related to particle multiplicity, a fit of the particle multiplicity or any other equivalent observable by the model can provide the measurement of  $N_{part}$ , thus the centrality<sup>1</sup>. The Glauber model [10] assumes straight line nucleon trajectories and a nucleons-nucleons cross section independent of the number of collisions that nucleons have undergone before. A Woods-Saxon distribution [9] can be used to model the nuclear density.

The second method for measuring centrality exploits the measurement of the energy of the spectator nucleons in the forward zero-degree calorimeters, located close to the beam pipe. This is in fact a direct count of the number of participants with the advantage of being independent from any model. Because however nuclear fragmentation breaks the simple relation in the measured variables, it has to be correlated with another measurement.

The impact parameter vector is important for the determination of the event plane of the collision, defined by the angle  $\Psi_R$  between the beam direction ( $z$  axis) and the impact parameter vector, as depicted in fig. 1.4.

When measuring particle production in the final state, the rapidity and pseudo-rapidity variables are defined. The rapidity is

$$y = \frac{1}{2} \ln \frac{E + p_L}{E - p_L} \quad (1.9)$$

where  $E$  is the particle energy and  $p_L$  the longitudinal momentum, that is the component of the momentum along the beam axis. The other two components of the momentum are combined to define the transverse momentum as  $p_t = \sqrt{p_x^2 + p_y^2}$ . The rapidity can be approximated by the pseudorapidity in the ultra-relativistic limit, where  $E \simeq p$ :

$$\eta = \frac{1}{2} \ln \frac{p + p_L}{p - p_L} = -\ln[\tan \frac{\theta}{2}], \quad (1.10)$$

with  $\theta$  being the angle of the particle momentum with respect to the  $z$  axis. We notice that the particles produced with high transverse momentum ( $p_t$ ) in hard scattering processes also have  $|\eta| \sim 0$ .

---

<sup>1</sup>This is the strategy used for centrality determination in ALICE, thus it has been used for the analysis presented in this thesis

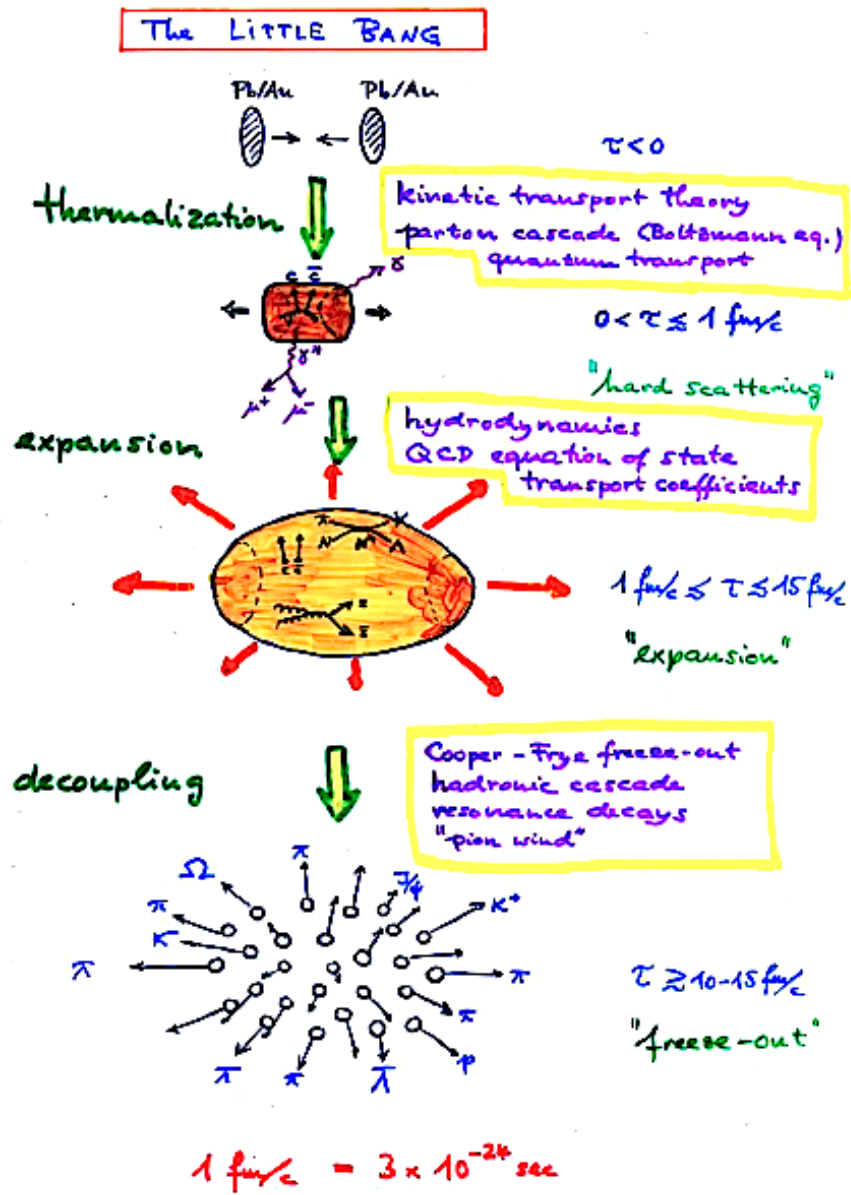


Figure 1.5 Pictorial schema of the QGP evolution [11].

In this section a selection of the most recent ALICE results in heavy-ion collisions at the LHC is presented. The aim is to provide a picture of the evolution phases of the produced medium, schematically drawn in fig. 1.5 [11]. The initial binary collisions between nucleons involve hard scattering between partons with large momentum transfer. The hard scattering processes, belonging to the regime of perturbative QCD, produce high- $p_t$  signatures and the opportunity of inspecting the initial phase through “hard-probes”. The inelastic scatterings produce an high parton density and the formation of the fireball. After the QGP formation, the fireball expands and cools down, for the effect of the exerted pressure on the vacuum surrounding the system. When the temperature goes below the critical temperature of the QCD phase transition, hadronisation takes place. The “chemical” freeze-out is the moment during the expansion when particle abundancies are fixed. The hadronic medium keeps expanding and hadrons keep interacting quasi- elastically, cooling the system until the “kinematic freeze-out” is reached. From that moment on, the momentum spectra of particles can change due to these elastic collisions or due to resonances decay, but ratios of produced particles are fixed. In the following sections, results on soft particle production, including particle abundancies and collective flow will be presented, whereas one can refer to the literature for most recent results on hard probes.

### 1.2.1 Global event properties

The number of charged particles produced per unit of (pseudo)rapidity,  $dN_{ch}/dy$  ( $dN_{ch}/d\eta$ ) in a central, head-on, collisions has been measured right after the first Pb–Pb at  $\sqrt{s_{NN}} = 2.76$  TeV data were delivered at the LHC. The value measured by ALICE,  $dN_{ch}/d\eta \approx 1600$  [?], compares with the last predictions before the LHC startup, that were giving  $dN_{ch}/d\eta \approx 1000 \div 1700$  [17]. From the average particle multiplicity the energy density produced at mid-rapidity in the collision can be estimated through the Bjorken formula relating the energy density to the transverse energy:

$$\varepsilon_B(\tau_0) \geq \frac{1}{\tau_0 S_\perp} \frac{dE_\perp}{d\eta} \quad (1.11)$$

where  $\tau_0$  is the thermalisation time,  $S_T$  is the transverse area of the incident nuclei and  $dE_\perp/d\eta$  the total transverse energy per unit of pseudorapidity [?]. The Bjorken formula assumes the longitudinal boost invariance of the system and the presence of a thermalized central region at time  $\tau_0$ . The transverse energy is related to the charged hadron multiplicity:

$$\frac{dE_\perp}{d\eta} = \frac{3}{2} \frac{1}{\tau_0 S_\perp} \langle E_\perp/N \rangle \frac{dN_{ch}}{d\eta} \quad (1.12)$$

where  $\langle E_\perp \rangle/N$  is the average transverse energy per emitted particle. The value measured at the LHC implies that the initial energy density (at  $\tau_0 = 1$  fm/c) is about 15 GeV/fm<sup>3</sup>, nearly three times higher than in Au–Au collisions at the top RHIC energy [18, 19, 20, 21]. This also corresponds to an increase of the initial

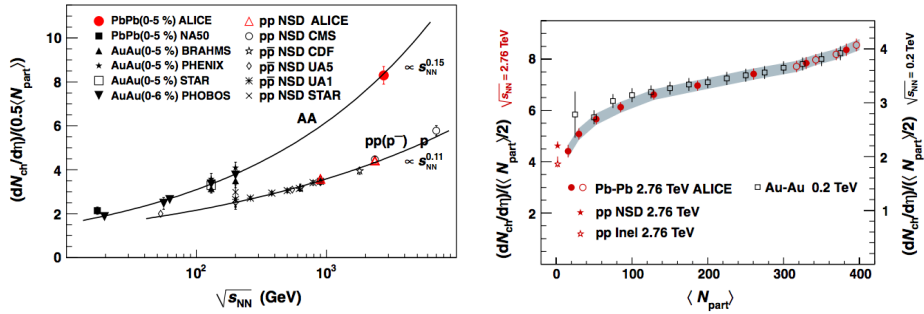


**Figure 1.6** Left: charged particle pseudo-rapidity density  $dN_{ch}/d\eta$  per colliding nucleon pair,  $0.5\langle N_{part} \rangle$  for pp and A–A collisions at several energies [?]. Right: centrality dependence of  $dN_{ch}/\eta$  per colliding nucleon pair,  $\langle N_{part} \rangle$  in Pb–Pb collisions at  $\sqrt{s_{NN}}=2.76$  TeV (red markers) and Au–Au collisions at  $\sqrt{s_{NN}}=200$  GeV (black markers). The scale for the lower-energy data is shown on the right-hand side and differs from the scale for the higher energy data on the left-hand side by a factor of 2.1 [13].

temperature by at least 30% to  $T \approx 300$  MeV, even with the conservative assumption that the medium formation time  $\tau_0$  remains the same as at RHIC.

The charged particle pseudo-rapidity density ( $dN_{ch}/d\eta$ ) per colliding nucleon pair ( $0.5\langle N_{part} \rangle$ ) is shown in fig. ?? (left) in comparison with pp and lower energy central A–A collisions (typically 0–5% or 0–6% centrality). The energy dependence is steeper for heavy-ion collisions than for pp and  $p\bar{p}$  collisions. A significant increase of about a factor 2.2 is observed in Pb–Pb collisions at LHC, with respect to Au–Au collisions at  $\sqrt{s_{NN}}=200$  GeV at RHIC [?]. Fig. ?? (right) shows that the centrality dependence of  $dN_{ch}/d\eta/\langle N_{part} \rangle$  at  $\sqrt{s_{NN}}=2.76$  TeV is very similar to that at  $\sqrt{s_{NN}}=200$  GeV, for which the measurements are reported with a scale that differs by a factor of 2.1 on the right-hand side [13].

### 1.2.2 Identified particle spectra and ratios

The expansion of the hadrons emitted in Pb–Pb collisions is characterized by the appearance of collective flow in the soft region of the spectrum. Collective flow implies a strong correlation between position and momentum variables and arises in a strongly interacting medium in the presence of local pressure gradients. Collective motion can be studied in the framework of hydrodynamic models, where the momentum spectra and the motion patterns are determined by the fluid properties (viscosity, equation of state, speed of sound) and the boundary conditions in the initial and in the final state (collision geometry, pressure gradients, freeze-out conditions). Radial flow is the component of the collective motion isotropic (or angle averaged) with respect to the reaction plane. It determines the expansion in the radial direction and can be estimated by measuring the primary hadron transverse momentum ( $p_t$ ) spectra.

Primary identified  $\pi/K/p$   $p_t$  spectra have been measured in the central rapidity

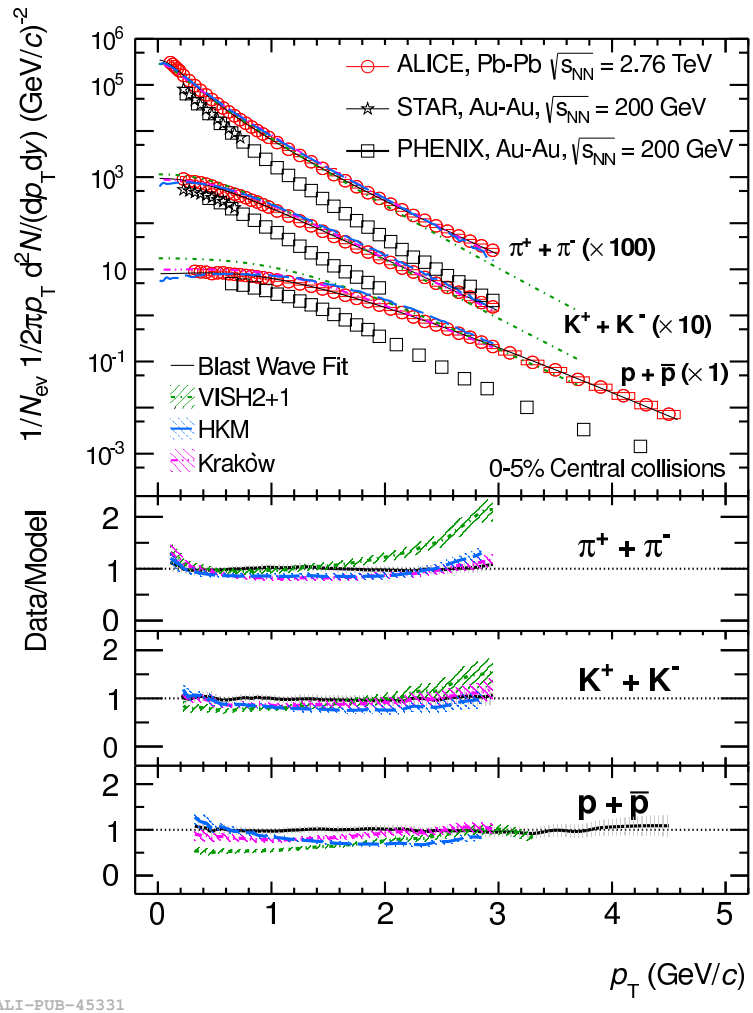


**Figure 1.7**  $\pi/K/p_t$  spectra in the 0–5% most central Pb–Pb collisions, measured by ALICE at  $\sqrt{s_{NN}} = 2.76$  TeV and compared with RHIC results [26, 27] and hydrodynamic-based model prediction [23, 24, 25].

region,  $|y| \leq 0.5$ , in ALICE for different collision centrality intervals. Primary particles are defined as the prompt particles produced in the collision. This includes the decay products, except those resulting from the weak decay of the strange hadrons. ALICE results are reported in Fig. 1.7 (red circles) for the most central collisions (0–5%), in comparison to a similar measurement performed at RHIC in Au–Au collisions at  $\sqrt{s_{NN}} = 200$  GeV [26, 27] (black markers in Fig. 1.7). The average  $p_t$  is higher at LHC than at RHIC and the spectral shapes look flatter at low  $p_t$ . In a hydrodynamic picture, harder spectra indicate that the medium expansion at LHC is driven by a significantly stronger radial flow. The radial flow velocity ( $\langle \beta_T \rangle$ ) can be estimated by fitting simultaneously the  $\pi$ , K and p spectra with a hydrodynamic-inspired function, called a Blast Wave [30]. For the most central collisions ALICE measures  $\langle \beta_T \rangle = 0.66 c$ , which corresponds to a value about 10% higher than the one measured by STAR [26]. Fig. 1.7 also shows the comparison of the data with different viscous hydrodynamic-based models, VISH2+1 [23], HKM [24] and Krakow[25]. In HKM, a hadronic cascade model (UrQMD [28]) description follows the hydrodynamic phase and adds a contribution to the radial flow mostly due to elastic interactions. In the Krakow model, the transition to the hadronic phase is described by non-equilibrium corrections due to viscosity which change the effective  $T_{ch}$ . HKM and Krakow better describe the data, suggesting the importance of taking into account the contribution from the hadronic phase on the measured flow. More details can be found in [29] and references therein.

### Strangeness enhancement

The measurement of strangeness production in heavy-ion collisions has been of great interest after the prediction [48] that the presence of a hot and dense medium allows the thermal production of strange quarks, leading to a strangeness enhancement in the final state. As a consequence of the restoration of chiral symmetry at the phase transition (see section 1.1), the threshold for the production of a  $s\bar{s}$  pair reduces from twice the mass of the constituent strange quark ( $\sim 900$  MeV) to twice the intrinsic mass of the quarks ( $\sim 300$  MeV). A copious production of  $s\bar{s}$  pairs, mostly by gluon fusion, is expected in the high energy density fireball. The deconfined phase can also enhance the production of multi-strange baryons due to recombination mechanisms. An enhanced production of hyperons is therefore expected to be a signal of a deconfined phase [48]. The enhancement is defined as the ratio between the yields in Pb–Pb collisions and the yields in pp collisions, where the former must be appropriately scaled by the number of participant nucleons to account for the increased interaction volume.

Strange particle and multi-strange baryon production at mid-rapidity has been measured in ALICE [31] via the topological reconstruction of the following decays:  $K_S^0 \rightarrow \pi^+ \pi^-$ ,  $\Lambda \rightarrow \pi^- p$ ,  $\Xi^- \rightarrow \pi^- \Lambda$ ,  $\Omega^- \rightarrow K^- \Lambda$  (and similarly for the anti-particle decays). The  $\Lambda$  spectra have been feed-down corrected for the contribution of  $\Lambda$  coming from the weak decays of  $\Xi^-$  and  $\Xi^0$ . The measured anti-baryon to baryon ratio is compatible with unity, confirming that the baryo-chemical potential

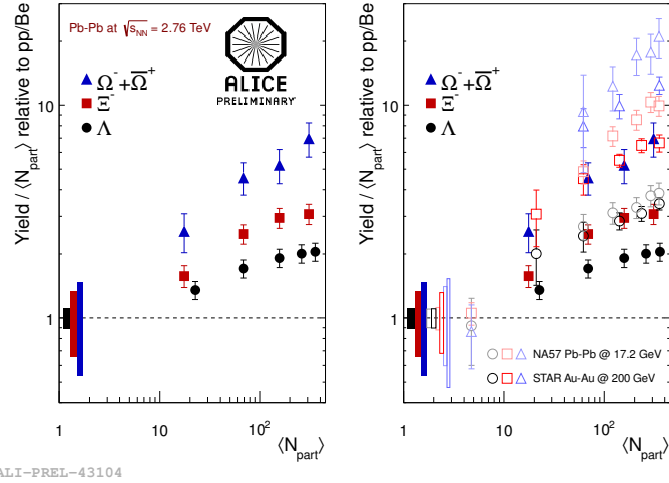


**Figure 1.8** Hyperon yields in Pb–Pb collisions scaled by the number of participant nucleons, relative to the yields in pp (p–Be) collisions, measured at mid-rapidity and for different centrality intervals. ALICE results (filled points), are compared with SPS and RHIC data (open points). The vertical bars indicate the quadratic sum of statistical and systematic uncertainty.

is close to zero, as expected at the LHC (see 1.1). The measured enhancement factors of baryons with increasing strangeness content ( $|S| = 1, 2, 3$ ) are reported in Fig. 1.8 as a function of the number of participant nucleons,  $\langle N_{part} \rangle$ , in comparison with similar measurements at SPS (WA97/NA57 [33, 34],  $\sqrt{s_{NN}} = 17.2$  GeV) and RHIC (STAR [35],  $\sqrt{s_{NN}} = 200$  GeV). For p–Pb collisions there is no evidence of enhancement. For Pb–Pb collisions the enhancement increases with centrality and the effect is larger for particles with higher strangeness content, up to a factor  $\sim 20$  for  $\Omega$ s. No hadronic model has reproduced these observations and they can be interpreted as clear signal of QGP state formation. The comparison with results from the previous experiments shows that the relative enhancements decrease with increasing collision energy. An explanation of this behaviour is given in terms of a statistical model, with canonical strangeness conservation. In a small system, with small particles multiplicities, quantum numbers conservation laws (such as strangeness) must be applied locally, event-by-event, whereas in a large system, with many degrees of freedom, they can be applied in average, by means of the corresponding chemical potential. The conservation of quantum numbers is known to reduce the phase space available for particle production. This canonical suppression factor decreases with lower energy in the centre of mass of the collisions and could explain the larger enhancement for lower energy systems [16].

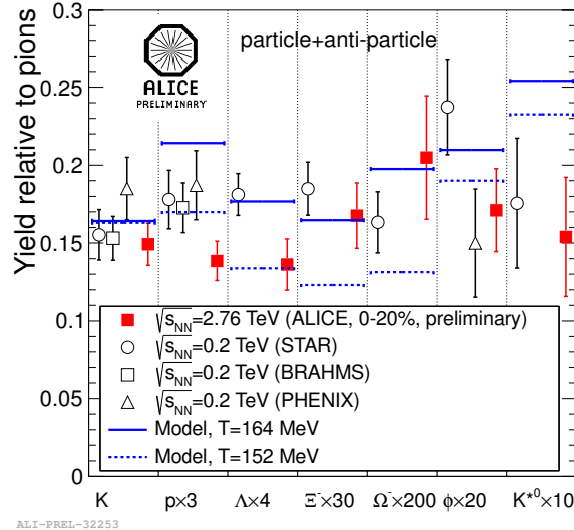


**Figure 1.9** Integrated yields at mid-rapidity relative to pions in central (0-20%) Pb–Pb collisions compared to RHIC measurements and thermal model predictions.

### Particle ratios

The identified particle yields measured by ALICE in Pb–Pb collisions at  $\sqrt{s_{NN}} = 2.76$  TeV have been used to compute particle ratios to be compared with the prediction of the thermal model [22], which has been proven to successfully describe the data in a broad range of lower collision energies. This model assumes that particles are created in thermal equilibrium and are governed by a scale parameter, defined as the chemical freeze-out temperature ( $T_{ch}$ ). The production of a particle with mass  $m$  is suppressed by a Boltzmann factor  $e^{-m/T_{ch}}$ . Conservation laws introduce additional constraints, like the baryochemical potential  $\mu_B$  which accounts for baryon number conservation. An additional parameter,  $\gamma_s$  is introduced to describe the observation that in some collision systems particles containing strange quarks are suppressed compared to the grand canonical thermal expectation (see also the previous section). The temperature  $T_{ch}$ , the volume ( $V$ ) and the baryo-chemical potential ( $\mu_B$ ) have been extracted by performing a thermal model fit [22] of the measured integrated yields at mid-rapidity for the 0-20% central collisions. The extracted temperature is  $T_{ch} = 152 \pm 3$  MeV. Thermal model predictions of particle ratios with this value of  $T_{ch}$  are close to the  $p/\pi$  and  $\Lambda/\pi$  ratios measured by ALICE, but do not agree with  $\Xi/\pi$  and  $\Omega/\pi$ , as shown in Fig. 1.9. A model where the  $T_{ch}$  is extracted from a fit to the RHIC data,  $T_{ch} = 164$  MeV, instead, seems to agree with the ratios involving multi-strange baryons, missing  $p/\pi$  and  $\Lambda/\pi$ . The deviation from the thermal model is still under discussion, after the suggestion that particle interactions during the hadronic phase, and in particular antibaryon-baryon annihilation, may affect the measured yields and ratios.

### 1.2.3 Anisotropic flow

When two nuclei collide with non-zero impact parameter, the spatial asymmetries due to the initial shape of the nuclear overlapping region are reflected into azimuthal anisotropies of particle emission. Due to larger pressure gradient, matter expands faster in the direction where the fireball size is smaller. Since these anisotropies are generated before matter reaches the critical temperature and hadronises, the elliptic flow is sensitive to the equation of state of the QGP phase. Large anisotropies indicate a strong collective behaviour and early local thermal equilibrium of the fireball. Re-scattering processes among the produced particles transfer the spatial deformation onto momentum space, or, in other words, the initially locally isotropic transverse momentum distribution of the produced matter begins to become anisotropic.<sup>x</sup>The magnitude of the anisotropic flow depends strongly on the friction of the strongly interacting matter, characterized by the viscosity over entropy density ratio ( $\eta/s$ ). The anisotropy is quantified in terms of the azimuthal Fourier coefficients of the transverse momentum spectrum:

$$E \frac{d^3N}{d^3p} = \frac{1}{2\pi} \frac{d^2N}{p_T dp_T dy} \left( 1 + 2 \sum_{N=1}^{\infty} v_n \cos[n(\varphi - \Psi_n)] \right) \quad (1.13)$$

where  $n$  is the order of the harmonic,  $\varphi$  indicates the particle azimuthal angle and  $\Psi_n$  is the angle of the spatial plane which maximises the expectation value of  $v_n$  in each event, the harmonic symmetry plane. The flow coefficients are  $p_t$  and  $\eta$ -dependent and are given by  $v_n(p_t, \eta) = \langle \cos[n(\varphi - \Psi_n)] \rangle$ , where the brackets denote an average over particles in a given  $p_t$  bin and over events in a given centrality class. Event-by-event fluctuations of the positions of the participating nucleons inside the nuclei, affect the shape of the initial energy density of the heavy-ion collision, that in general is not symmetric with respect to the reaction plane.  $\Psi_n$  may deviate from the reaction plane, giving rise to non-zero odd harmonic coefficients<sup>2</sup>. It also contributes to the difference in flow coefficients calculated from two- or multi-particle azimuthal correlations, and also to the difference in measured  $v_n$  with respect to different harmonic symmetry planes.

The elliptic flow magnitude was measured RHIC, where  $v_2$  reaches a value compatible with the one predicted by hydrodynamics for a “perfect fluid”, that is a fluid without internal friction and vanishing shear viscosity [41]. At LHC, the elliptic flow has been studied by ALICE [42] as function of centrality and found to reach its maximum between 30% and 50% centrality, where the asymmetry of the collision is more enhanced. In comparison to RHIC, the integrated  $v_2$  of charged particles increases by about 30%, indicating that the hot and dense matter created at LHC still behaves like a fluid with almost zero viscosity.

Besides  $v_2$  [42, 44], ALICE has measured triangular,  $v_3$ , and quadrangular,  $v_4$ , azimuthal anisotropic flow with respect to both second and fourth order event planes,  $v_{4/\Psi_2}$  and  $v_{4/\Psi_4}$ . The difference between the two is due to fluctuations in

---

<sup>2</sup>For details see [40], and references therein.

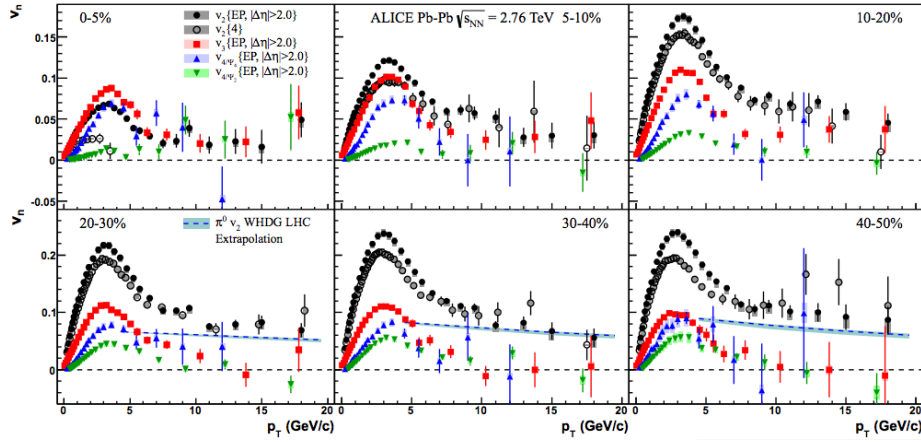


**Figure 1.10**  $v_2$ ,  $v_3$  and  $v_4$  coefficients measured for unidentified charged particles as a function of  $p_t$  for various centrality classes [40]. The dashed line represents the WHDG model calculations for neutral pions  $v_2$  [43] extrapolated to the LHC collision energy. For clarity, the markers for  $v_3$  and  $v_4/\psi_2$  results are slightly shifted along the horizontal axis. Error bars (shaded boxes) represent the statistical (systematic) uncertainties.

the fourth order harmonic flow, providing important constraints on the physics and origin of the flow fluctuations. The flow coefficient, shown in fig. 1.10 have been measured for unidentified charged particles in  $|\eta| < 0.8$  and  $p_t$  up to 20 GeV/c for different event centralities [40]. Significant non-zero elliptic flow as well as  $v_3$  were found up to the highest transverse momenta. The elliptic flow for  $p_t > 10$  GeV/c is well described by the WHDG model [43] extrapolation to the LHC energies, that considers also re-scattering and radiative energy loss in the expanding medium.

The shape of the  $p_t$ -differential anisotropic flow suggests the presence of different underlying mechanisms in different momentum regions. At  $p_t < 1 \div 2$  GeV/c the flow pattern is mostly determined by hydrodynamical flow exhibiting typical mass splitting, whereas for  $p_t > 10$  GeV/c, the anisotropy is believed to be defined by the jet quenching mechanism. In the intermediate  $p_t$  region ( $3 \div 6$  GeV/c) hadron production via quark coalescence is probed by measuring  $v_2$  of identified hadrons scaled by the number of constituent quarks ( $n_q$ ) as a function of the transverse momentum normalized to the same quantity ( $p_t/n_q$ ). Such a scaling finds a natural explanation in the quark coalescence picture, the so-called Number of Constituent Quark (NCQ) scaling [45, 46]. The measured elliptic flow scaled by the number of constituent quarks for identified particles is reported in fig. 1.11. The ALICE results show approximate (within 20%) scaling of  $v_2$  vs.  $p_t$  with  $n_q$  at  $p_t 1.2$  GeV/c [?]. As the quark anisotropic flow and hadronisation via coalescence means the system being in a deconfined stage, the observation of such a scaling is very important.

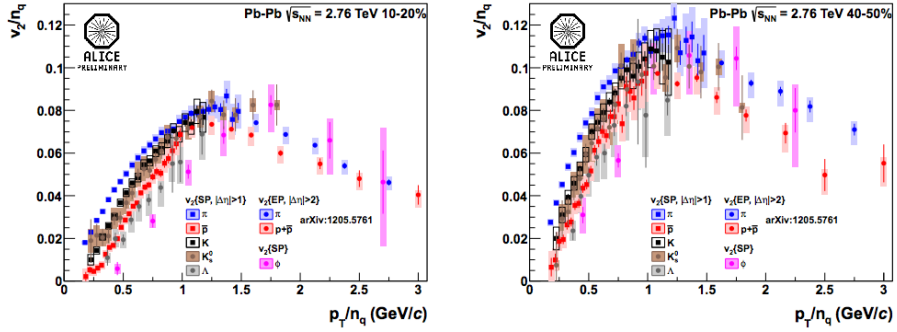


**Figure 1.11** Elliptic flow scaled by the number of constituent quarks  $v_2/n_q$  for identified particles as a function of  $p_t/n_q$  for events with 10-20% (left) and 40-50% (right) centrality measured by ALICE in Pb-Pb collisions [?].

### 1.3 Resonance production in heavy-ion collisions

Resonances are particles with higher mass than the corresponding ground state particle with the same quark content. Hadronic resonances decay strongly, thus with a short lifetime,  $\tau \sim$  few tenths of  $\text{fm}/c$ . The resonance natural width is given by  $\Gamma = \hbar/\tau$ , that is inversely proportional to the lifetime. Broad states with finite  $\Gamma$  decay very shortly after being produced and can be measured only by reconstruction of their decay products (or “daughters”) in a detector. In heavy-ion collisions, hadronic resonances are produced within the bulk of the expanding medium, where they can decay while still traversing its volume. Decay products may interact with the other particles of the medium (mostly pions at the LHC), resulting in the impossibility of reconstructing the resonance, because the invariant mass of the daughters does not match that of the parent particle. Conversely, resonances may be regenerated as a consequence of pseudo-elastic collisions in the time lapse between the chemical ( $T_{ch}$ ) and the kinetic freeze-out ( $T_{kin}$ ). Re-scattering and regeneration depend on the individual cross section, hence lifetime, of the resonances and affect the measurement of their yield and momentum spectrum. The yield is decreased if the re-scattering dominates, viceversa the regeneration feeds the system with more particles. The two effects may even compensate.

The hadronic phase following the chemical freeze-out can be simulated in a hadronic cascade model, such as UrQMD [47], based on the known hadron masses and cross sections. The time evolution of the chemical composition of an expanding fireball, initiated at the phase transition critical temperature  $T_c$  with chemical equilibrium particle abundances, is shown in fig. 1.12 for Au–Au collisions at  $\sqrt{s_{NN}}= 200$  GeV as at RHIC [47]. Hyperons and resonances, decay, while the stable hadrons reach their asymptotic yields. The unstable particle abundances are not frozen at the chemical freeze-out, because of the re-scattering and regeneration processes. The hadron cross sections are in fact dominated by resonances, which

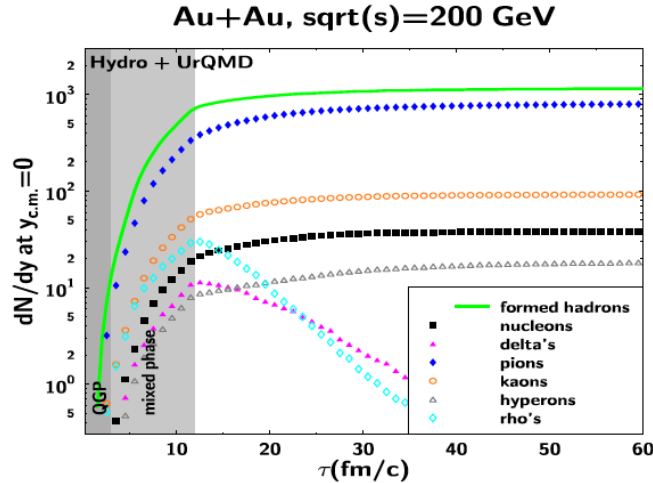


**Figure 1.12** Evolution of the chemical composition of an expanding hadronic fireball produced in Au+Au collisions at  $\sqrt{s_{NN}}= 200$  GeV as function of the medium proper time, from a UrQMD simulation. The expansion was started at the phase transition critical temperature  $T_c$ , with chemical equilibrium particle abundances [47].

means that processes like  $\pi+N \rightarrow \Delta \rightarrow \pi+N$ ,  $\pi+\pi \rightarrow \rho\pi+\pi$ ,  $\pi+K \rightarrow K^* \rightarrow \pi+K$ , and so on, happen frequently in the hadronic medium. These processes contribute to equilibrate the hadron momentum distribution with the decreasing temperature. Their abundances do not decrease with a exponential decay law, but more slowly thanks to resonance regeneration [11]. A resonance with larger pionic interaction cross section, would decouple from the medium later (so at a lower temperature) with respect to those with smaller pionic decay width. In addition, it has to be stressed that because most of the resonances tend to decay into the same hadrons from which they were formed (and viceversa), the yields of stable hadrons are not modified. In section 1.2.2 the thermal model [22] was briefly discussed. There, under the assumption that particles of the bulk freeze-out at the same time, particle ratios can be predicted by fixing model parameters such as the temperature ( $T_{ch}$ ) and the baryo-chemical potential ( $\mu_B$ ). If re-scattering and regeneration do not compensate exactly, the measured resonance yields are expected to differ from the prediction of the thermal fit of the stable hadron yields for  $T_{ch}$ , for example

$$\frac{K^*}{K} |_{measured} \neq \frac{K^*}{K} |_{thermal,T_{ch}}. \quad (1.14)$$

Different resonances with different lifetimes can probe different stages of the fireball expansion. The lifetime of some short-lived resonances is reported in table 1.1. The ratios between resonances and stable hadrons can be compared for resonances with different lifetimes and provide insights on the role of the re-scattering effect between the two freeze-out phases. For example, the model [?, 49] shown in

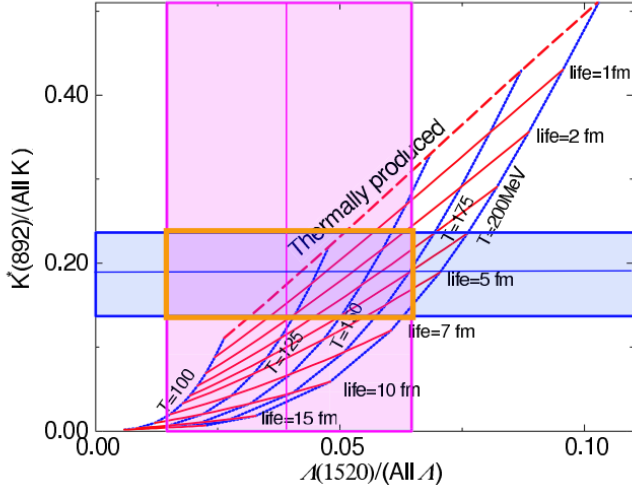


**Figure 1.13** Hadronic medium lifetime and chemical freeze-out temperature dependence from particle ratios  $K^*(892)/K$  and  $\Lambda(1520)/\Lambda$ , from the model in [?]. The magenta and blue lines mark the particle ratios measured by STAR in Au–Au collisions at RHIC [49].

fig. 1.13, determines the dependence of lifetime and  $T_{ch}$  from two particle ratios,  $K^*(892)/K$  and  $\Lambda(1520)/\Lambda$ . The blue and magenta lines mark the values of the two ratios measured by STAR in central Au–Au collisions at  $\sqrt{s_{NN}} = 200$  GeV. The shaded area therefore represents all the possible values that  $\tau_0$  and  $T_{ch}$  could assume to lead to the measured particle yields. Because however this model does not include regeneration, it is applicable only if re-scattering dominates and predicts a lower limit for the time span between the two freeze-out stages.

$\rho(770)$	$\tau_\rho = 1.3 \text{ fm}/c$
$\Delta(1232)$	$\tau_\Delta = 1.7 \text{ fm}/c$
$K^*(892)$	$\tau_{K^*} = 4.0 \text{ fm}/c$
$\Sigma(1385)$	$\tau_\Sigma = 5.5 \text{ fm}/c$
$\Lambda(1520)$	$\tau_\Lambda = 10.3 \text{ fm}/c$
$\phi(1020)$	$\tau_\phi = 46 \text{ fm}/c$

**Table 1.1** Lifetime of hadronic resonances [50].

Beside the study of the hadronic medium evolution, resonance production measurement addresses the issue of in-medium modifications of the intrinsic particle properties and partial chiral symmetry restoration.

It has been shown [51] that light resonances containing strange quarks, such as the  $K^*$ ,  $\phi$ ,  $\Delta$  and  $\Lambda^*$  have very short formation time and large probability to be produced within the QGP phase [52]. The hadronic formation time as function of

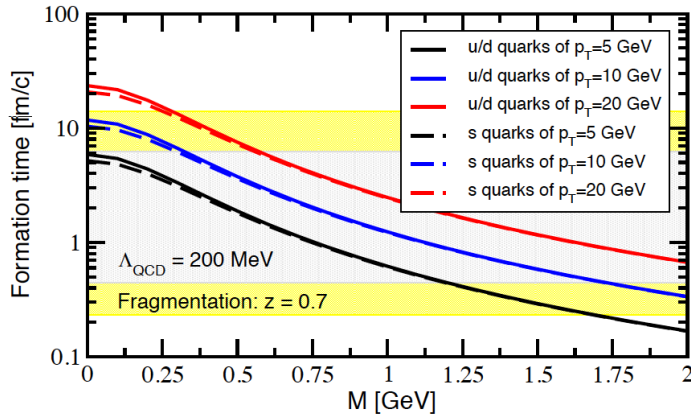


**Figure 1.14** Hadronic formation time as function of the particles mass  $M$ , for different quark  $p_t$  and fixed fractional momentum ( $z$ ). The yellow shaded areas indicate the upper and lower limits for the medium lifetime of the partonic phase at RHIC and LHC, respectively [51].

the particle mass for several quark transverse momenta is qualitatively reported in fig. 1.14 [51]. At the LHC, hadron formation happens within the medium lifetime, measured to be  $\sim 10$  fm/ $c$  from HBT interferometry [?]. Hadronic states that are formed and decay within the lifetime of the partonic medium, experience in-medium interactions with the surrounding QGP system and decay off-shell if chiral symmetry restoration reduces its mass. As previously discussed in section 1.1, the chiral phase transition takes place nearly when the confined-deconfined matter transition occurs. This is suggested by the dependence from the critical temperature of the Polyakov loop and chiral condensate plotted in fig. 1.3. The presence of a partial chiral symmetry restoration can be investigated by studying intermediate momentum resonances, which are formed early and decay into particles that escape the partonic medium ad suffer of only little re-scattering and regeneration during the subsequent hadronic medium expansion phase. According to UrQMD calculations [?], hadronic re-interactions affect only low momentum ( $0 < p_t < 2$  GeV/ $c$ ) resonances. Medium-induced effects may appear experimentally as reduced production rates, modification of the branching ratios, mass shifts and broadening of the widths in the QGP phase, that are expected to be detectable. No evidence for these effects has yet emerged from the preliminary analysis of resonances production at the LHC, therefore leaving room for more detailed study of resonance production and decay and experimental searches.

The study of the  $\phi(1020)$  and  $K^*(892)$ <sup>3</sup> production is of particular interest, given the fact that both are mesonic resonances with close mass values (and close

<sup>3</sup>For the sake of brevity, in the following  $\phi$  will substitute  $\phi(1020)$ ;  $K^{*0}$  will indicate both the  $K^*(892)$  and its antiparticle. When discrimination is necessary, the latter will be indicated as  $\bar{K}^{*0}$ .

to the proton mass) but their lifetime differ of about a factor 10, being  $\tau_\phi = 46 \text{ fm}/c$  and  $\tau_{K^*} = 4.0 \text{ fm}/c$ . Also, their strangeness content differs by one unit. Among the two, the  $K^{*0}$  is expected to be more sensitive to the re-scattering effects in the hadronic medium, because of the much shorter lifetime. On the other hand, the  $\phi$  escaping the medium with almost no re-scattering are good candidates to look for hints of partial restoration of the chiral symmetry at the formation time. In addition, the  $\phi(1020)$  is a good candidate to probe strangeness production, being the lightest vector meson composed of sea quarks ( $s\bar{s}$ ) only. In pp collisions,  $s\bar{s}$  pair production was found to be significantly suppressed in comparison with  $u\bar{u}$  and  $d\bar{d}$  [?, ?]. In Pb–Pb the strangeness suppression effect is reduced, as described in section ???.  $\phi$  and  $K^{*0}$  have been measured in pp collisions at  $\sqrt{s} = 7 \text{ TeV}$  and  $\sqrt{s_{NN}} = 2.76 \text{ TeV}$  by ALICE. Results are discussed in the next sections.

### 1.3.1 $\phi(1020)$ and $K^*(892)$ production in pp collisions at the LHC

Results on  $\phi(1020)$  and  $K^*(892)$  resonance production in pp collisions at  $\sqrt{s} = 7 \text{ TeV}$  have been recently published by ALICE [53]. Since the decay products of resonances represent a large fraction of the final state particles, their study in pp collisions contribute to the understanding of the hadron formation mechanisms. In addition, measurements in pp collisions provide a reference for tuning QCD-inspired event generators and, mostly important, constitute a baseline for the measurements in Pb–Pb collisions.

$\phi$  and  $K^{*0}$  have been measured at mid-rapidity, through the following hadronic decay channels:  $\phi \rightarrow K^+ K^-$  (branching ratio  $\sim 49.5\%$ ) and  $K^{*0} \rightarrow K^\pm \pi^\mp$  (branching ratio  $\sim 66.6\%$ ) [50]. The invariant mass distributions before and after background subtraction are reported in fig. 1.15 for  $K^{*0}$  of  $p_t \sim 1 \text{ GeV}/c$  (left) and  $\phi$  of  $p_t \sim 1.2 \text{ GeV}/c$  (right). Details of the analysis can be found in [53].

The measured transverse momentum spectra are reported in fig. 1.16 in comparison with QCD-inspired Monte Carlo event generators like PHOJET [?] and PYTHIA [54], that simulate multi-particle production using the Lund string fragmentation model (see [53] and references therein). Different PYTHIA tunes were obtained by adjusting the model parameters to reproduce existing data and have been compared. None of the models provides a fully satisfactory description of the data. The best agreement is found for the PYTHIA Perugia 2011 tune, which reproduces both the  $K^{*0}$  spectrum and the  $\phi$  spectrum for  $p_t > 3 \text{ GeV}/c$  rather well, as well as it provides a satisfactory description of kaon production in pp collisions at 7 TeV[?].

The transverse momentum spectra have been fitted with a Lvy-Tsallis function in order to extract the yields. The measured yields for both mesons have been found to increase by about a factor of two from the previous measurements at  $\sqrt{s} = 200 \text{ GeV}$ , while the average  $p_t$  is about 30% larger. Finally the  $K^{*0}/K$  and  $\phi/K^{*0}$  ratios (and consequently the  $\phi/K$  ratio) have been measured and found to be independent of the collision energy up to 7 TeV. Also the  $\phi/\pi$  ratio, which increases in both pp and A–A collisions up to at least RHIC energies, saturates and becomes

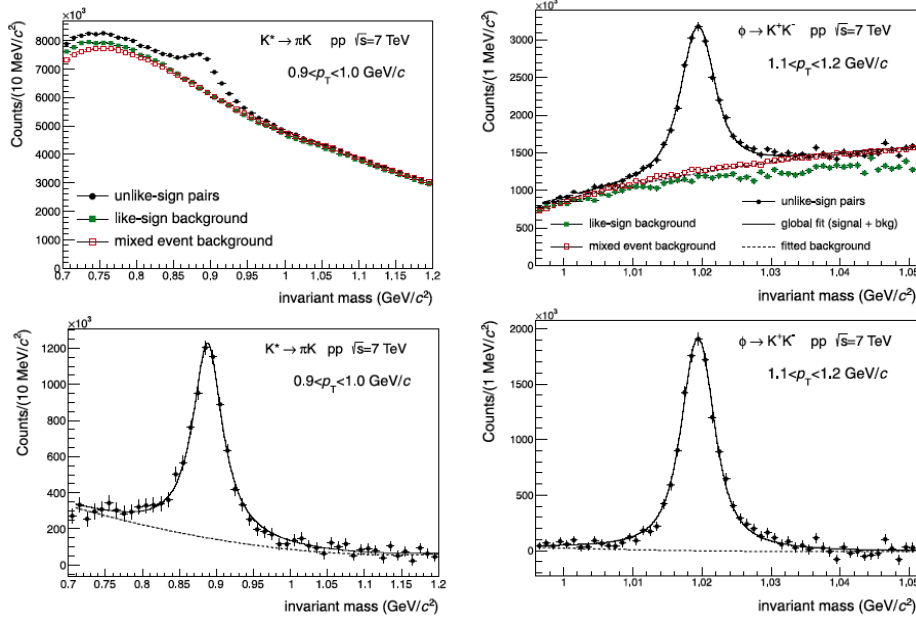


**Figure 1.15** Invariant mass distribution for the  $K^{*0}$  (left)  $\phi$  (right) before (top) and after (bottom) background subtraction. The background with from like-sign and event mixing techniques is shown. The solid black line represent the result of the fit of the signal and residual background shape. In particular, the  $\phi$  peak is shaped by a Voigtian function, the  $K^{*0}$  signal is fitted with a relativistic Breit-Wigner function multiplied by a Boltzmann factor [53].

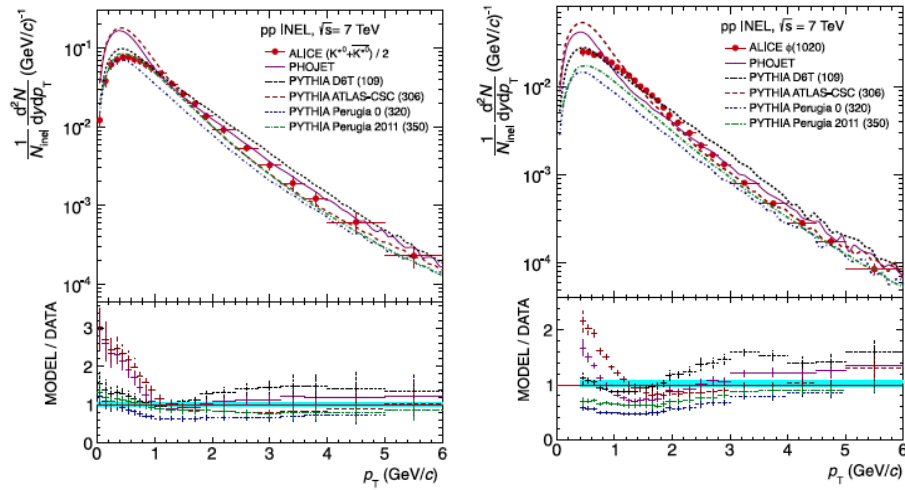


**Figure 1.16** Comparison of the  $\phi$  (left) and  $K^{*0}$   $p_T$  spectra measured in inelastic pp collisions at  $\sqrt{s} = 7$  TeV with PHOJET and PYTHIA tunes D6T (109), ATLAS-CSC (306), Perugia 0 (320), and Perugia 2011 (350). See [53] and references therein.

independent of energy above 200 GeV.

### 1.3.2 $\phi(1020)$ and $K^*(892)$ production in Pb–Pb collisions at LHC

At the beginning of the section it was discussed that the production of resonances can occur during the transition from the QGP to the hadronic phase and during the hadronic phase, due to regeneration. Having lifetimes comparable to that of the expanding medium, many resonances decay during the hadronic phase. As a consequence, their decay products tend to be re-scattered in the hadronic medium, making experimental reconstruction of the resonance hard, if not impossible. The contribution of re-scattering and regeneration to the resonant yield are affected by the temperature, density and lifetime of the medium, and so do the measured ratios of resonance yields to non-resonance yields [?]. It was also discussed in section 1.2.2 how particle ratios can be predicted by thermal models, as functions of the chemical freeze-out temperature and the elapsed time between chemical and thermal freeze-out [22]. Moreover, the model presented in fig. 1.14 showed how, in principle, the chemical freeze out temperature and the medium lifetime can be extracted from the measurement of two different particle ratios<sup>4</sup>.

Measurements of resonances production at RHIC can be found in [?, ?, ?] and references therein. A preliminary measurement of  $\phi$  and  $K^{*0}$  in Pb–Pb collisions at  $\sqrt{s_{NN}} = 2.76$  TeV with the ALICE detector has been presented in few recent occasions[?, 56]. As for the pp analysis [53] presented in the previous section, resonances produced at mid-rapidity ( $|y| < 0.5$ ) have been reconstructed through their hadronic decay channels,  $\phi \rightarrow K^+ K^-$  (branching ratio  $\sim 49.5\%$ ) and  $K^{*0} \rightarrow K^\pm \pi^\mp$  (branching ratio  $\sim 66.6\%$ ) [50]. The decay products have been selected in the rapidity region  $|\eta| < 0.8$  and identified thanks to the measured energy loss in the ALICE Time-Projection Chamber. The interested reader can refer to [?, 56] for more details on the analysis strategy. The resonance signal has been studied with an invariant mass analysis in several event centrality classes and as function of the resonance momentum. The invariant mass distributions after combinatorial background subtraction are shown in fig. 1.17 for most central collisions (0-10% for  $\phi$  and 0-20% for  $K^{*0}$ ).

The invariant mass distributions exhibit a peak and a residual background, that is partly due to an imperfect description of the combinatorial background but mainly caused by a real correlated background, usually attributed to correlated  $\pi K$  or  $KK$  pairs or to misidentified particle decay products (for example, misidentified kaons from a  $\phi$  decay or misidentified  $\pi$  from the  $\rho^0$  decay for the  $K^{*0}$ ). A fit with a Breit-Wigner and a polynomial function is performed to extract yields and resonance intrinsic parameters. The mass and width of both  $K^{*0}$  and  $\phi$  are reported as function of  $p_t$  in fig. 1.18 and 1.19 for central and peripheral collisions. The measured values of the  $\phi$  mass are within  $5 \text{ MeV}/c^2$  from the nominal value. For  $K^{*0}$ , the measured mass is consistent with the values measured in pp collisions at

---

<sup>4</sup>In practice, many measured ratios are used to obtain a best-fit value for these model parameters.

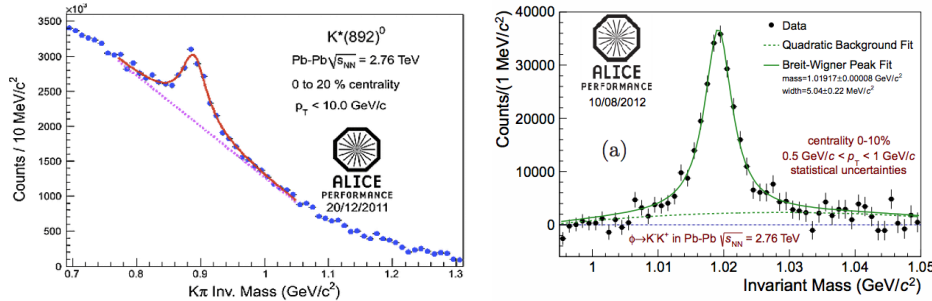


**Figure 1.17** Invariant mass distribution for  $K^{*0}$  (left) and  $\phi$  (right) in central Pb–Pb collisions at  $\sqrt{s_{NN}}=2.76$  TeV. For each particle, the combinatorial background has been subtracted and the residual background is shown. The peak is fitted using a Breit-Wigner function summed to a polynomial that shapes the residual background. The solid curves represent the total functions. For  $\phi$ , the plot refers to 0–10% central events and  $0.5 < p_t < 1$   $\text{GeV}/c$ ; the residual background is a second degree polynomial function. For  $K^{*0}$ , the plot refers to the centrality class 0–20% and  $p_t < 10$   $\text{GeV}/c$ ; a first-order polynomial is used to fit the residual background.

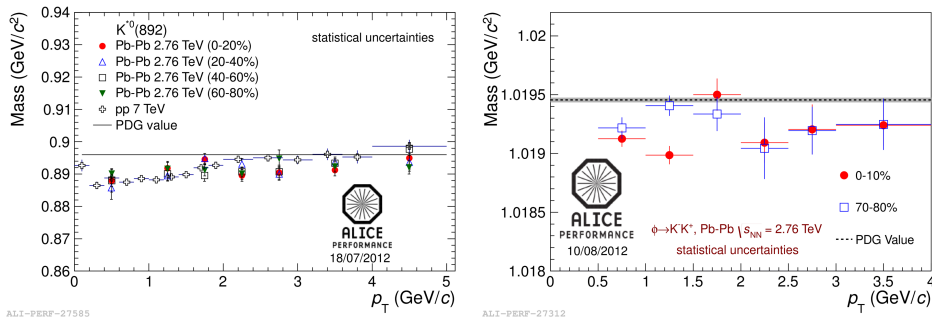


**Figure 1.18** Mass of  $K^{*0}$  (left) and  $\phi$  (right) in Pb–Pb collisions at  $\sqrt{s_{NN}}=2.76$  TeV, for different centralities.

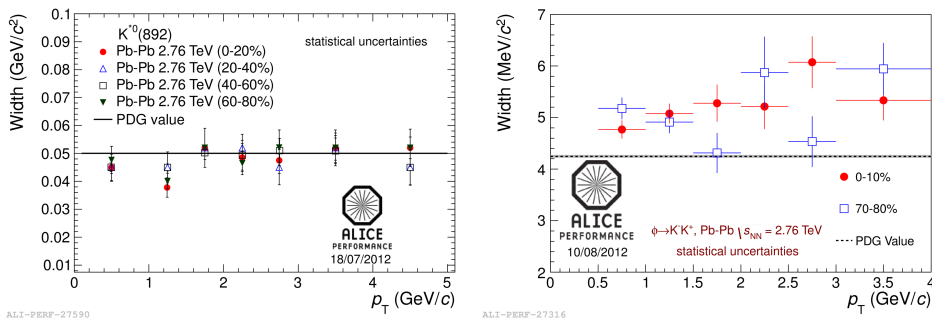


**Figure 1.19** Width of  $K^{*0}$  (left) and  $\phi$  (right) in Pb–Pb collisions at  $\sqrt{s_{NN}}=2.76$  TeV, for different centralities.

$\sqrt{s} = 7$  TeV, which suggests that the observed  $\sim 8$  MeV/ $c^2$  deviation from the nominal value is not a hot QCD matter effect, but most likely an instrumental effect. The measured values of the width for the  $\phi$  are within 2 MeV/ $c^2$  from the nominal value. For the  $K^{*0}$  width, no significant difference with respect to the nominal value is found. The measurements show that there is no obvious centrality dependence in either the mass or the width.

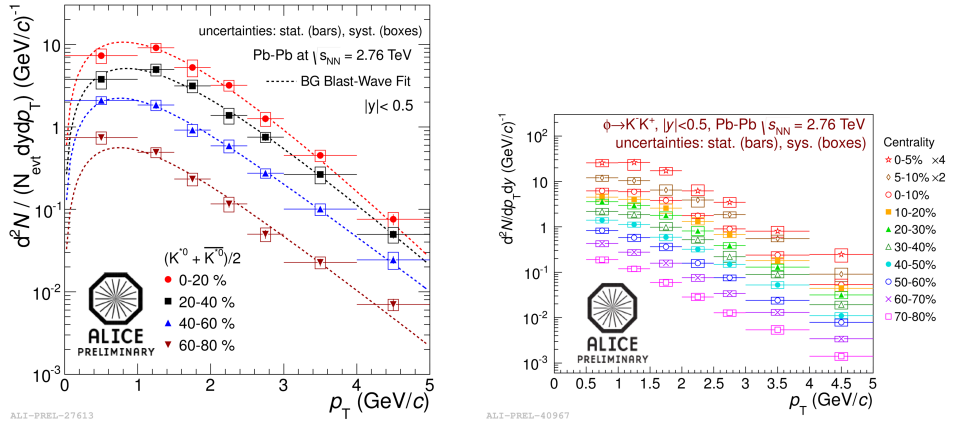


**Figure 1.20** Transverse momentum spectra of  $K^{*0}$  (left) and  $\phi$  (right) in Pb–Pb collisions at  $\sqrt{s_{NN}} = 2.76$  TeV, for different centralities.

Preliminary measurements of the resonance yields, corrected for efficiency and detector acceptance, are reported in fig. 1.20 as function of transverse momentum (for  $p_t < 5$  GeV/ $c$ ) and centrality.

The total yields  $dN/dy$  of both mesons are calculated by integrating the spectra and using the result of a Blast Wave fit [?] to estimate the yields for  $p_t < 0.5$  GeV/ $c$  and  $p_t > 5$  GeV/ $c$ . Particle ratios are then built by using the yields of charged pions and kaons measured in Pb–Pb collisions by ALICE (see section 1.2.2). The  $\phi/\pi$  and  $\phi/K$  ratios, shown in fig. 1.21, are independent of collision energy and colliding system, from RHIC to LHC. The  $\phi/\pi$  ratio measured by ALICE is also below the prediction from a thermal model with  $T_{ch} = 164$  MeV (see also fig. 1.9 and section 1.2.2). No dependence from the centrality of the collisions is seen for the  $\phi/\pi$  and  $\phi/K$  ratios. The results for  $K^{*0}$ , shown in fig. 1.22 instead show that the  $K^{*0}/K^-$  ratio is dependent of the average number of participant nucleons, that is, it decreases with centrality. Given their different lifetimes, the different behaviour of the  $\phi/K$  and  $K^{*0}/K^-$  ratios could be interpreted as due to increasing re-scattering effects in the medium in central collisions. This result is however still under discussion, as the system properties, such as the density and expansion time have to be taken into account before proposing a final interpretation.

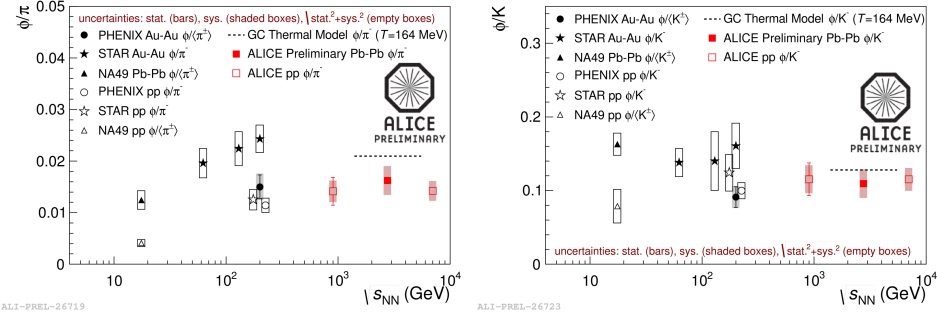


**Figure 1.21**  $\phi/\pi$  and  $\phi/K$  ratios measured in Pb–Pb collisions at  $\sqrt{s_{NN}} = 2.76$  TeV by ALICE, compared to the measurement in different collision systems.

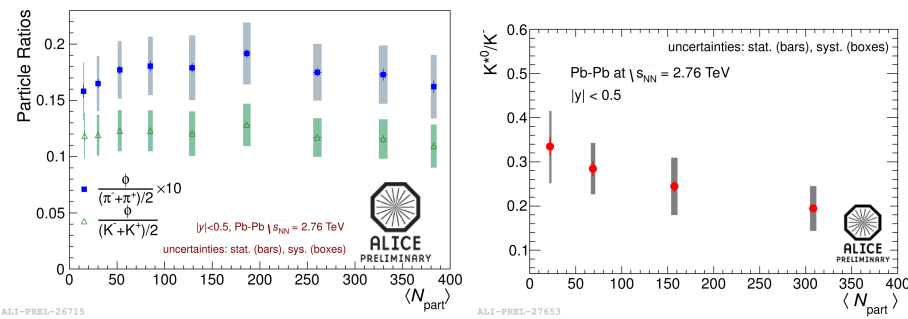


**Figure 1.22** Left:  $\phi/\pi$  and  $\phi/K$  ratios as function of the average number of participant nucleons. Right:  $\phi/K^-$  as function of  $N_{part}$  in Pb–Pb collisions at  $\sqrt{s_{NN}} = 2.76$  TeV. All ratios are measured by ALICE in Pb–Pb collisions at  $\sqrt{s_{NN}} = 2.76$  TeV.



## Chapter 2

# A Large Ion Collider Experiment at the LHC

ALICE (A Large Ion Collider Experiment) has been collecting data during the whole first phase of the Large Hadron Collider operations, from its startup on the 23 November 2009 to the beginning of the first long technical shutdown in February 2013. During the first three years of operations LHC provided pp collisions at 0.9, 2.76, 7 and 8 TeV, Pb–Pb collisions at 2.76A TeV and finally p–Pb collisions at 5.02 TeV. The first section of this chapter focuses on the LHC performance during this phase and includes details on the accelerator parameters that allow the LHC to perform as a lead ion collider. A detailed description of the ALICE detector follows in the section 2.2. ALICE has been designed and optimized to study the high particle-multiplicity environment of ultra-relativistic heavy-ion collisions and its tracking and particle identification performance in Pb-Pb collisions are discussed. The attention is drawn in particular on the central barrel detectors. Section 2.3 describes the ALICE Data Acquisition (DAQ) system, that also embeds tools for the online Data Quality Monitoring (DQM). The final part of the chapter is dedicated to the offline computing and reconstruction system based on the GRID framework.

### 2.1 The Large Hadron Collider

The Large Hadron Collider (LHC) [57], [58] is a two-ring-superconducting hadron accelerator and collider installed in the 26.7 Km tunnel that hosted the LEP machine and it completes the CERN accelerator complex together with the PS and SPS, among the others shown in fig. 2.1. Four main experiments are located in four different interaction points along its circumference. ATLAS and CMS, the biggest ones, are multi-purpose detectors built to discover the Higgs boson and hints of new physics beyond the Standard Model. LHCb is dedicated to the physics of the flavour, focusing on the study CP-violation using B meson decay channels. The phenomena that these three experiments aim to observe have production cross section of the order of a hundred of pb or lower, therefore a large number of collision

events is required to the machine in order to fulfill the LHC pp physics program. ALICE, on the contrary, is dedicated to the physics of Quark Gluon Plasma through the observation of high-energy heavy-ion collisions, although a shorter physics program with pp collisions has been carried out.

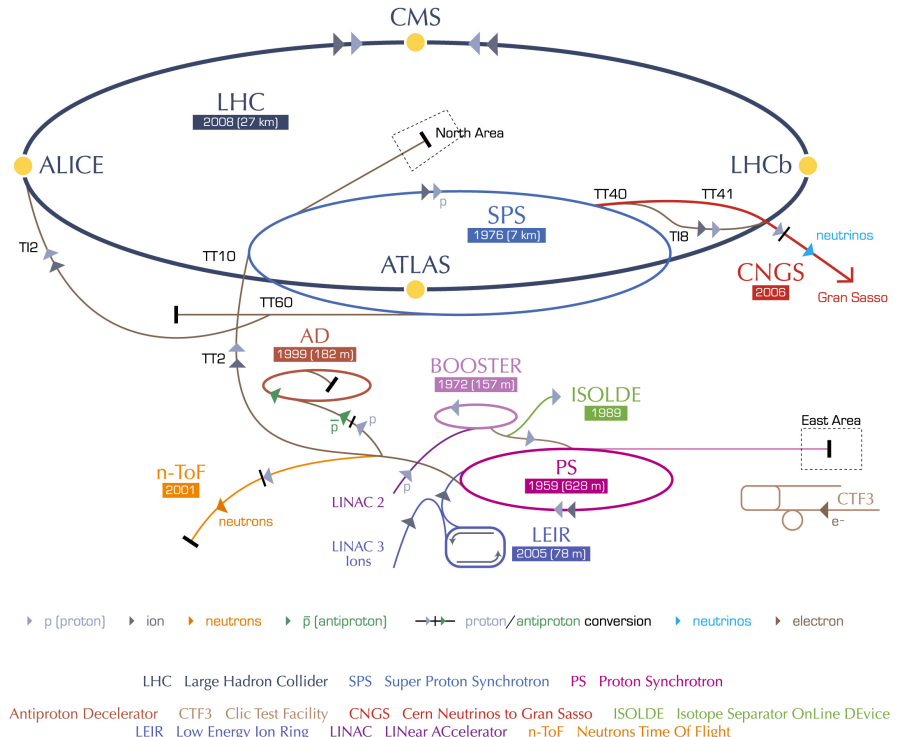


**Figure 2.1** Schema of the CERN accelerator complex.

The LHC was initially designed to provide pp collisions at the energy of  $\sqrt{s} = 14$  TeV and Pb–Pb collisions at  $\sqrt{s_{NN}} = 5.5$  TeV. However, after the technical incident of 2008 [59] due to the quenching of a magnet, in 2010 [60] and 2011 the LHC run at half of the design energy, thus providing pp collisions at  $\sqrt{s} = 7$  TeV and Pb–Pb collisions at  $\sqrt{s_{NN}} = 2.76$  TeV. The excellent performance of the machine lead to the decision of increasing the center of mass energy to  $\sqrt{s} = 8$  TeV for pp collisions during the 2012 run.

Besides energy, the most important accelerator parameter is the instantaneous (often the “peak” value within a fill is reported) luminosity,  $L$ , which is the proportionality factor between the event rate  $R$  and the interaction cross section of the process under study ( $\sigma_{int}$ ):

$$R = L\sigma_{int} \quad (2.1)$$

The instantaneous luminosity depends only on the colliding beam parameters at

the interaction point and can be determined as

$$L = \frac{N_b^2 n_b f \gamma}{4\pi \epsilon_n \beta^*} F \quad (2.2)$$

where

$N_b$  is the number of particles per bunch,  
 $n_b$  the number of bunches per beam,  
 $f$  the revolution frequency,  
 $\gamma$  the relativistic gamma factor,  
 $\epsilon_n$  the normalized transverse beam emittance,  
 $\beta^*$  the amplitude function at the interaction point (IP),  
 $F$  the geometrical reduction factor that accounts for the crossing angle at the IP.

It is worthy to remind that the transverse emittance and the amplitude function are related to the bunch cross-sectional size ( $\sigma_L$ )<sup>1</sup> by the relation:

$$\sigma_L^2 = \frac{1}{\pi} \beta \epsilon. \quad (2.3)$$

The transverse emittance tells us how successful was the process of “packing” protons into bunches during the injector chain: a low emittance particle beam is such that the particles are confined to a small distance and have nearly the same momentum. This is important to keep the particle confined in their orbit all along the beam transport and accelerating chain that is optimised for a given design momentum. The  $\beta$  function is determined by the accelerator magnet configuration, more precisely by the quadrupole focusing strength. If the amplitude is small, the beam is squeezed. The value of the amplitude function at the interaction point, referred to as  $\beta^*$  is the most significant. In order to achieve higher luminosity, it is important to keep the emittance low and  $\beta^*$  as small as possible, depending on the capability of the beam-focusing hardware near the interaction point. Moreover, in order to have  $\beta^*$  small at the interaction point,  $\beta$  is kept at larger values along the orbit. Since the emittance changes as a function of the beam momentum during the acceleration, the normalised emittance,  $\epsilon_n = \gamma \beta \epsilon$ , which does not vary during the acceleration is most commonly considered, as in equation 2.2.

If it is assumed that the particles in each bunch are distributed in the three spatial directions according to Gaussian distributions with  $\sigma_{xy}$  and  $\sigma_z$  being respectively the size in the transverse plane and in the longitudinal direction (along the beam pipe), the  $F$  factor can be obtained from the total crossing angle at the IP,  $\theta_c$ , as

$$F = \left[ 1 + \left( \frac{\theta_c \sigma_x}{2 \sigma_{xy}^*} \right)^2 \right]^{-1/2}. \quad (2.4)$$

The bunch transverse and longitudinal sizes are the same for both beams, as well

---

<sup>1</sup>This is also referred to as “luminous region”, because the emittance and amplitude parameters enter directly in the luminosity definition of eq. 2.2.

as the number of particles per bunch. The latter is limited to be lower than  $N_b = 1.15 \times 10^{11}$  because of the linear beam-beam tune, which measures the interaction that each particle undergoes when two bunches collide, and by the mechanical aperture of the LHC that also constrains the acceptable transverse emittance to  $\varepsilon_n = 3.75 \mu\text{m}$  for a  $\beta = 180$  m in the LHC arcs. The number of bunches per beam instead has been varying according to the definition of different filling schemes during the machine operations. The beam parameters,  $\varepsilon$  and  $\beta^*$  in particular, have been optimized in order to tune the luminosity in the different interaction points, allowing all experiments to exploit their different capability. The two higher luminosity experiments, ATLAS and CMS run at a peak luminosity of the order of  $L \sim 10^{33} \text{cm}^{-2}\text{s}^{-1}$  while LHCb run at the design luminosity value of  $L \sim 10^{32} \text{cm}^{-2}\text{s}^{-1}$ . The maximum luminosity sustainable by ALICE in pp collisions is limited to the value  $L \sim 10^{30} \text{cm}^{-2}\text{s}^{-1}$  in order to avoid pile-up in the main tracker detector, being ALICE an experiment not optimised for data taking at high rate in pp.

		<b>Injection</b>	<b>Collision</b>	
Energy	[GeV]	450	7000	
Luminosity	[ $\text{cm}^{-2}\text{s}^{-1}$ ]		$10^{34}$ $2.5 \times 10^{34}$	
Number of bunches			2808	3564 bunch places
Bunch spacing	[ns]		24.95	
Intensity per bunch	nominal ultimate	[p/b] $1.70 \times 10^{11}$	$1.15 \times 10^{11}$	
Beam current	nominal ultimate	[A]	0.58 0.86	
Transverse emittance (rms, normalized), nominal & ultimate	[ $\mu\text{m}$ ]	3.5	3.75	Emittances equal in both planes, small blow-up allowed in LHC
Longitudinal emittance, total	[eVs]	1.0	2.5	Controlled blow-up during accel.
Bunch length, total ( $4\sigma$ )	[ns]	1.7	1.0	has to fit into 400 MHz buckets
Energy spread, total ( $4\sigma$ )	[ $10^{-3}$ ]	1.9	0.45	

**Figure 2.2** Nominal beam parameters.

### 2.1.1 The injection chain

The LHC is supplied with protons from the pre-existing CERN accelerators, that have been partially upgraded to meet the requirements of the brand new machine for unprecedented high intensity proton bunches, small transverse and well defined longitudinal emittance, and finally bunch spacing of 25 ns. Several other conditions needed to be taken into account, such as the limit on the beam intensity that comes from the capacity of the cryogenic system to absorb the synchrotron radiation, the space-charge effect in the injectors, the requirement for the beam emittance to fit the aperture of the LHC superconducting magnets, among others. These considerations lead to the “nominal” running parameters reported in fig. 2.2, which however were not applied during the first two years of operations. The actual parameters are

instead reported in section 2.1.3.

The proton source is a hydrogen tank from which the protons are extracted and injected in the Linear Accelerator 2 (Linac2), where they are accelerated up to 50 MeV. In the 4-rings Proton Synchrotron Booster (PSB) protons reach momentum of 1.4 GeV before being accelerated up to 25 GeV in the Proton Synchrotron (PS) accelerator, where a multiple splitting technique is used to generate the bunch trains. The four PSB rings accelerate one proton bunch per ring to a momentum of 1.4 GeV. A two-batch filling scheme allows to inject into the 8-slot PS three plus three (or alternatively four plus two) bunches from the PSB. Once in the PS the six bunches are split into three still at the injected energy of 1.4 GeV. Then the beam is accelerated up to 25 GeV before each bunch is split twice in two via 20 MHz and 40 MHz RF systems which have been installed during the LHC construction. A last RF system, playing at 80 MHz, splits the bunches into 4 ns long ones, to fit into the 200 MHz SPS buckets. After the debunching-rebunching procedure in the PS, the outgoing train contains 72 filled and 12 consecutive empty bunches for a total 84 buckets. The empty gap covers 320 ns, which also corresponds to the rise-time of the injection and extraction kickers. When the protons pass to the Super Proton Synchrotron accelerator (SPS) they finally reach 450 GeV and then they are injected at the threshold energy into the LHC. After the injection of all bunches from the SPS to the LHC is completed, the energy ramp up procedure starts and accelerates the beams to the final energy. The LHC RF cavities operate at 40 MHz. In the ultimate LHC filling pattern, each of the available bunch slots is split in 10 buckets, each of them being 2.5 ns long. Only one out of 10 is filled with a bunch, thus leaving us with the minimum bunch separation of 25 ns. Considering the empty slots, the injection scheme explains why 2808 is the maximum number of bunches that can be arranged in the 3564 available 25 ns slots of the LHC. Most of the buckets end up not containing an actual bunch, however the nominally empty buckets can in fact contain small populations of particles, which are called “satellite” or “ghost” bunches, depending on the fact that they may be within the same 10-bucket slot as a nominal bunch or in slot supposed to be empty, respectively. As it is detailed in section 2.1.3, the satellite bunches have also been used to provide collisions to ALICE during the pp run, whenever luminosity needed to be kept under control and to lower values, avoiding dangerous pile-up in the detector.

### 2.1.2 The LHC as heavy-ion accelerator

Since its early stages, LHC was designed to perform as well as heavy ion collider, in particular to feed ALICE with data, although also CMS and ATLAS included the study of ion collisions with similar luminosities in their physics program<sup>2</sup>.

The particle source is a 3 cm lead cylinder, which is heated to about 500°C in order to vaporise a small number of atoms that, once partially ionised by a strong electric field, are accelerated in a linear device, in order to strip off the remaining electrons,

---

<sup>2</sup>LHCb did not participate in the Pb–Pb run in 2010 and 2011.

until the ions become  $^{208}\text{Pb}^{82+}$ . Lead ions are then injected and accumulated in a Low Energy Ion Ring (LEIR) and then are sent to the PS, from which they follow the same injection chain as the protons. With the nominal magnetic field of 8.33 T in the dipole magnets, the ions can reach a beam energy of 2.76 TeV/nucleon, yielding to  $\sqrt{s_{\text{NN}}} = 5.5$  TeV or a total centre-of-mass energy of 1.15 PeV. The nominal luminosity value is  $1.0 \times 10^{27} \text{ cm}^{-2} \text{ s}^{-1}$ , while for early operations a two-orders of magnitude lower value was foreseen.

### 2.1.3 LHC operations

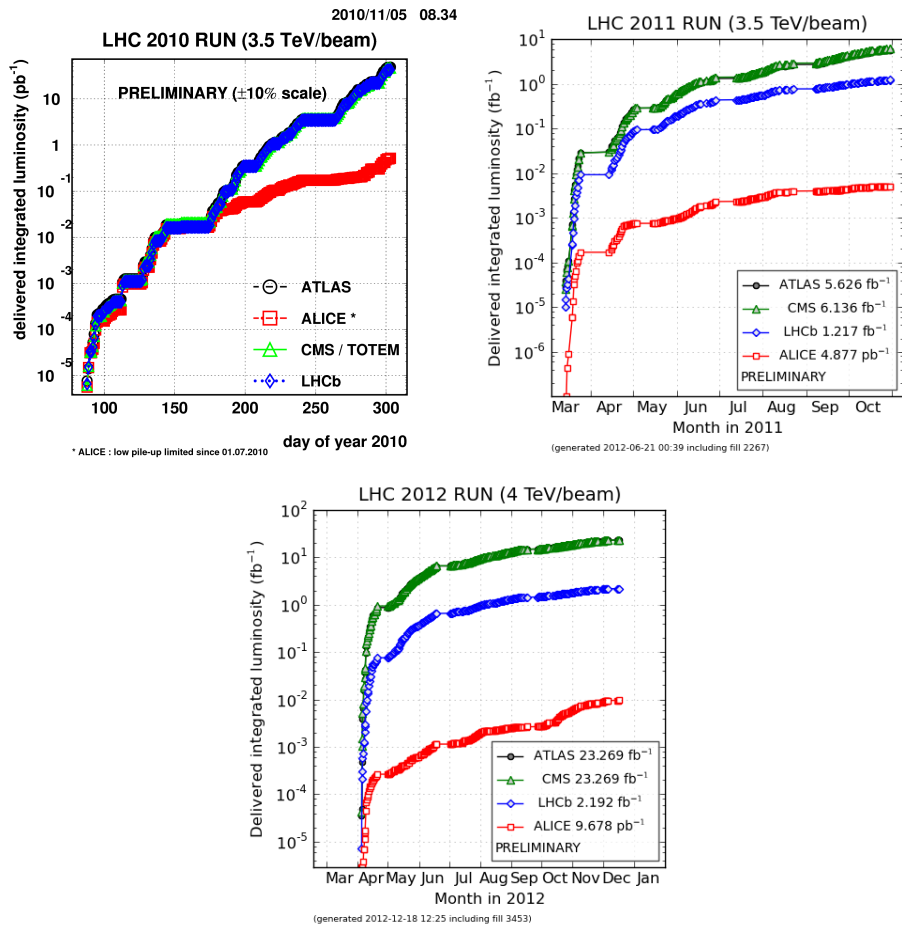


**Figure 2.3** Total integrated luminosity recorded by the LHC experiments during 2010 (top left), 2011 (top right) and 2012 (bottom center) in pp collisions at  $\sqrt{s} = 7$  TeV and  $\sqrt{s} = 8$  TeV (in 2012 only).

### 2010, 2011 and 2012 pp runs

The total number of recorded collision events is most commonly expressed in terms of integrated luminosity ( $L_{int}$ ) with units of inverse cross section and is reported as function of time for the different experiments and periods in figs. 2.3.

### 2010 and 2011 Pb–Pb runs

The first collisions between stable beams of  $^{208}\text{Pb}^{82+}$  took place on the 7th November 2010, after a very short period of nearly 50 hours of commissioning [61]. The beam energy was 3.5 Z TeV, corresponding to a center-of-mass energy of  $\sqrt{s_{NN}}=2.76$  TeV per nucleon pair. Despite this value represented half of the nominal center-of-mass energy, still it was 13.8 times higher than the energy ever reached in heavy-ion collisions. By the end of the run on 6 December 2010, an integrated luminosity of  $L_{int}=10\ \mu\text{b}^{-1}$  had been delivered to ALICE, ATLAS and CMS, with a peak luminosity of  $L=3.0\times10^{25}\text{cm}^{-2}\text{s}^{-1}$ . Table 2.4 reports the effective parameters (averaging over bunch-to-bunch and horizontal-vertical variations) recorded during the 2010 fill with the peak luminosity.

Beam energy	$E = 1.38\text{A TeV} = 3.5\text{Z TeV}$
No. of bunches/ring	$k_b = 137(62)$
Ions/bunch	$N_b = 11.2\times10^7(7\times10^7)$
Normalised emittance	$\varepsilon_N = 2.(1.5)\ \mu\text{m}$
Optical function	$\beta^* = 3.5\ \text{m}$
Luminosity	$L = 3.\times10^{25}\ \text{cm}^{-2}\text{s}^{-1}$

**Figure 2.4** Effective parameters at peak luminosity in 2010 Pb–Pb run (fill 1541). Values in blue are the design parameters.

A second Pb–Pb run was performed in November 2011 at the same collision energy but increased peak luminosity. Figure 2.5 summarizes the integrated luminosity as function of data-taking time for the three experiments in 2010 and 2011. The increase of the statistics by more than a factor 10 is clearly visible.

### Special runs

Short periods of pp collisions at lower energy of 0.9 and 2.76 TeV were performed respectively at the end of year 2009 and in April 2011. Finally, a p–Pb data taking is planned at the beginning of year 2013. A long technical shutdown is planned for 2013–2014, during which minor hardware upgrades to the machine, including magnet’s splice consolidation, will be performed to prepare a longer run at the nominal energy.

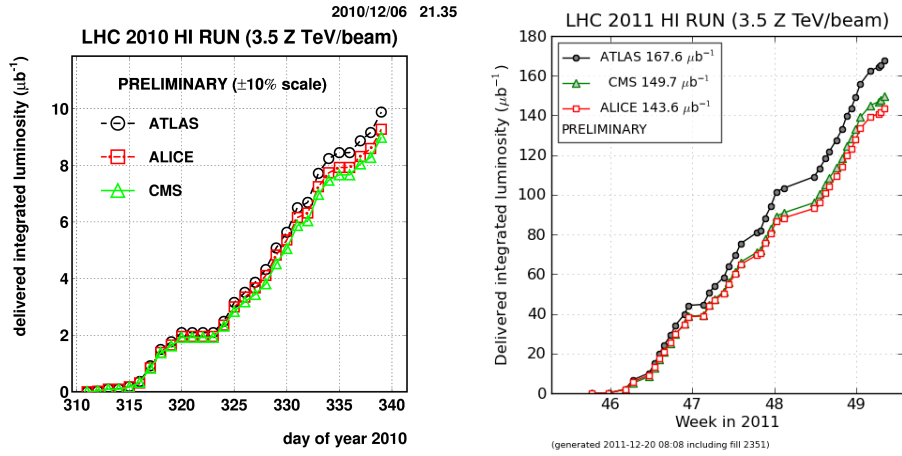


**Figure 2.5** Total integrated luminosity recorded by the LHC experiments during 2010 (left) and 2011 (right) in Pb–Pb collisions at  $\sqrt{s_{\text{NN}}}=2.76 \text{ TeV}$ .

## 2.2 The ALICE detector

A Large Ion Collider Experiment [62], [63] is mainly addressed to study the Quark Gluon Plasma produced in heavy-ion collisions at the LHC. The detector, located at the interaction point 2 along the LHC ring, has been designed to cope with a high particle multiplicity environment and to provide unique particle identification (PID) performance that allow a comprehensive study of hadrons, electrons, muons, and photons produced in the collision, down to very low transverse momentum (0.1 GeV/c). As already mentioned, ALICE has been taking data also during proton-proton runs at low and top reached LHC energy, that provided reference data for the Pb–Pb measurements, as well as during proton-ion run that instead completes the heavy-ion physics program of the experiment. In fig. 2.6 a scheme of the full ALICE detector is depicted. The projection of the central barrel in the transverse plane is reported in fig. 2.7, with details on the installed sub-detector modules as at the end of 2012.

ALICE is composed by a central barrel part, enclosed in the L3 solenoid magnet which provides a 0.5 T magnetic field, and by a forward muon spectrometer, which also includes a dipole magnet providing a 0.67 T field. The central barrel detectors cover the mid-rapidity region  $|\eta| \leq 0.9$  and include, going from the beam pipe outward, a six-layer silicon Inner Tracking System (ITS) that provides precise tracking and vertex determination, a large-volume Time Projection Chamber (TPC) that is responsible for the global tracking and PID through the measurement of the specific energy loss in gas, a Transition Radiation Detector (TRD) and a Time-Of-Flight system which respectively allow the identification of electron and charged hadrons. Because of its relevance for the analysis presented in this work, the entire chapter 3 is dedicated to the TOF.

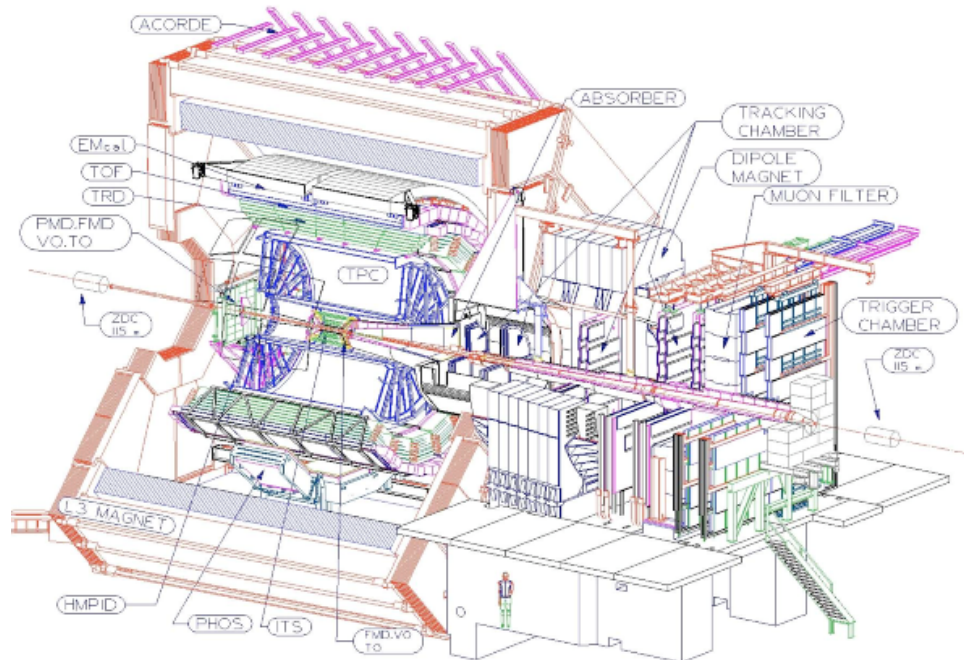


**Figure 2.6** Scheme of the ALICE detector.

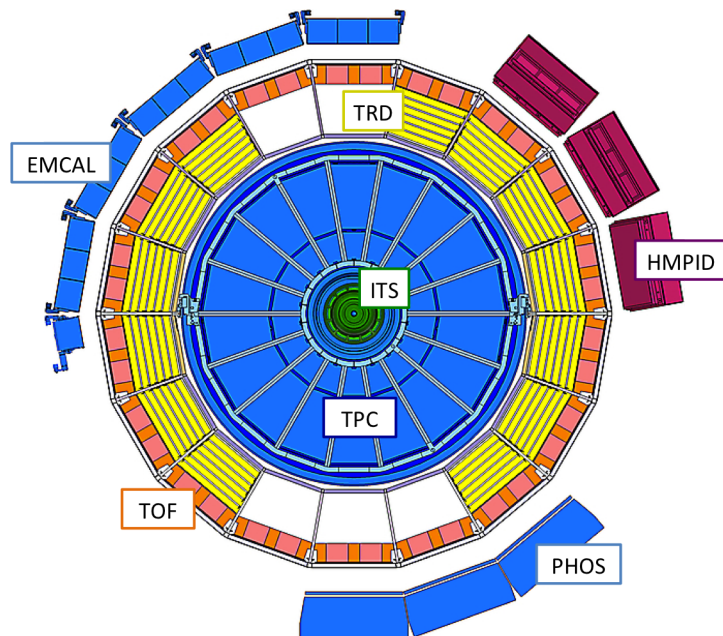


**Figure 2.7** Transverse plane schematic view of the ALICE central barrel detectors as at the end of 2012.

In addition to the mentioned detectors, that grant  $2\pi$  azimuthal coverage, some limited acceptance detectors are located inside the L3 magnet, outside the TOF:

- the High Momentum Particle Identification Detector (HMPID) is dedicated to the identification of charged hadrons with  $p_t \geq 1$  GeV/c. It is based on Ring Imaging Cherenkov (RICH) counters, arranged in seven modules of about  $1.5 \times 1.5$  m<sup>2</sup> size each, to cover a geometrical acceptance of 5% of the central barrel. The momentum threshold for the emission of Cherenkov photons in the C<sub>6</sub>F<sub>14</sub> liquid radiator is  $p_{min} = 1.21m$ , where  $m$  is the particle mass. Photons are then detected by a photon counter with a thin layer of CsI deposited onto the pad cathode of a MultiWire Pad Chamber (MWPC);
- the ElectroMagnetic CALorimeter (EMCAL) is a large Pb-scintillator sampling calorimeter with the purpose of measuring jet properties and providing trigger on jets and high-momentum photons and electrons, in addition to electrons identification. The EMCAL is located at a distance of 4.5 m from the beam line with a geometrical coverage of  $|\eta| \leq 0.7$  and  $\Delta\phi = 170^\circ$ ;
- the PHOton Spectrometer (PHOS), a high-resolution electromagnetic spectrometer, made of dense scintillator material crystals (PbWO<sub>4</sub>). It is positioned at a distance of 460 cm from the interaction point, azimuthally opposed to the EMCAL, and covers a limited acceptance ( $|\eta| \leq 0.12$  and  $\Delta\phi = 100^\circ$ ). PHOS is dedicated to the detection of low- $p_t$  direct photons that can probe the initial phase of the collisions, and to the study of the jet quenching effect through the measurement of high- $p_t$   $\pi^0$  and  $\gamma$ -jet correlations.

The forward pseudorapidity region is covered by a single-arm muon spectrometer in the range  $-4.0 < \eta < 2.5$  and a few smaller acceptance detectors. A Photon Multiplicity Detector (PMD) measures the multiplicity and spatial distribution of photons at  $2.3 < \eta < 3.7$ . It consists of two planes of gas proportional counters preceded by two lead converter plates. A silicon strip-based Forward Multiplicity Detector (FMD) extends the pseudorapidity region where the ITS provides information on particle multiplicity to  $-3.4 < \eta < -1.7$  and  $1.7 < \eta < 5.0$ . The FMD3 and FMD2 rings of this detector are located on either side of the ITS detector (at about 75cm from the IP) while a third ring, FMD1, is placed at 320 cm from the IP on the opposite side with respect to the muon spectrometer. Finally two arrays of segmented scintillator counters are used to define the minimum bias trigger, beam-gas background rejection and the centrality (V0) while two arrays of Cherenkov counters have also been installed asymmetrically with respect to the interaction point to measure the start time of the collision (T0) and combine this information with the time-of-flight measurement from the TOF detector. The centrality in ion collisions has been alternatively measured by the Zero-Degree Calorimeter (ZDC), namely constituted by two sets of neutron and proton calorimeters located nearly symmetrically at about 116 m from the interaction point. Finally, an array of 60 scintillators is installed on top of the magnet to provide cosmic rays trigger for calibration and alignment purpose and for cosmic ray physics (ACORDE).

### 2.2.1 The Inner Tracking System

The Inner Tracking System (ITS), as the closest tracking detector to the LHC beam pipe, is the main responsible for measuring the primary vertex of the collision. Its six concentric cylindrical layers are based on three different technologies of silicon detectors: pixels, drifts and strips, as schematized in fig. 2.8. The ITS is located at radius between 4 and 43 cm, surrounding the LHC beryllium beam pipe that is  $800\mu\text{m}$  thick and has a radius of 2.9 cm. The detector layout has been designed taking into account the high multiplicity environment foreseen for central Pb–Pb collisions (a few thousands of particles per unit of rapidity were expected at the top energy), so that the occupancy is kept on the order of few percent.

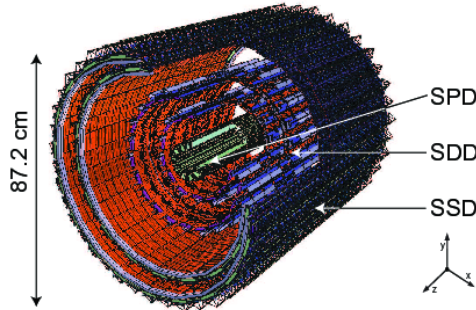


**Figure 2.8** The ALICE Inner Tracking System layers.

The two innermost ITS layers constitute the SPD, Silicon Pixel Detector. A total of  $9.8 \times 10^6$  readout channels receive signals from the 20 half-staves of the SPD, each of them consisting of 240 modules with 1200 readout chips. Thanks to the high-granularity the SPD has also been used for the trigger system, especially for the minimum bias event selection. The SPD is mainly used to determinate the primary vertex position, with a resolution of the order of  $100\mu\text{m}$ .

The Silicon Drift Detector (SDD) is based on modules with a sensitive area of  $70.17(r\phi) \times 75.26(z)\text{ mm}^2$ , divided into two drift regions where electrons move in opposite directions under a drift field of approximately  $500\text{ V/cm}$ . The SDD modules are mounted on a linear structure called ladder. The SDD inner layer is made of 14 ladders with 6 modules each, the outer layer has 22 ladders, each of them with 8 modules. The position of the particle along  $z$  is reconstructed from the centroid of the collected charge along the anodes, while the position along the drift  $r$  coordinate is obtained from the measured drift time with respect to the trigger time. This reconstruction requires a precise knowledge of the drift speed, that is measured during frequent calibration runs, given its strong dependence from the humidity and temperature gradients in the SDD volume.

The Silicon Strip Detector (SSD) building block is a module composed of one double-sided strip detector connected to two hybrids hosting the front-end electronics. The sensors are  $300\mu\text{m}$  thick and with an active area of  $73(r) \times 40(z)$

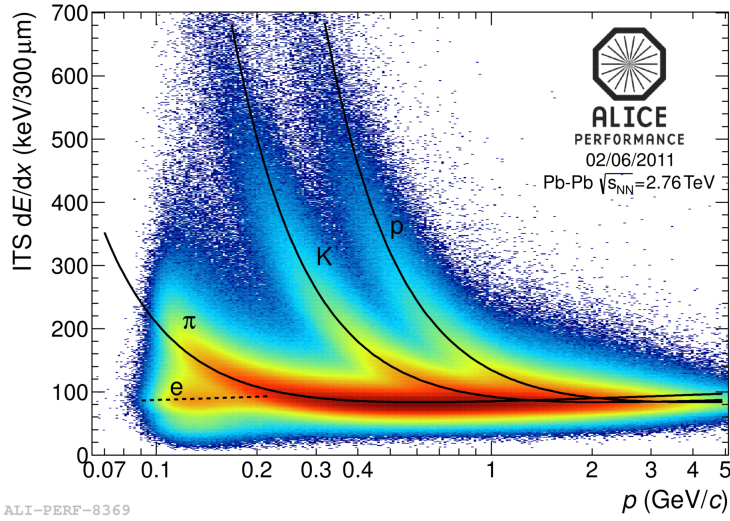


**Figure 2.9**  $dE/dx$  distribution of charged particles as function of their momentum, both measured by the ITS alone, in PbPb collisions at 2.76 TeV. The lines are a parametrization of the detector response based on the Bethe-Bloch formula.

$\text{mm}^2$ . Each sensor has 768 strips on each side, almost parallel to the  $z$  beam axis direction, with a pitch of  $95\ \mu\text{m}$ . The innermost SSD layer is composed of 34 ladders, each of them grouping 22 modules along the beam direction, while the other SSD layer is made of 38 ladders, each of them with 25 modules. Since the four outer layers have analogue readout, they are used for particle identification via energy loss ( $dE/dx$ ) measurement in the non-relativistic region for low momentum particles (down to  $p_t=100\ \text{MeV}$ ). An example of the particle identification capabilities of the ITS is shown in figure 2.9 for heavy-ion collisions: electrons can be identified from  $80\ \text{MeV}/c$  up to  $160\ \text{MeV}/c$  with a  $2\sigma$  separation from  $\pi$ . Pions are separated from kaons up to  $0.6\ \text{GeV}/c$  and kaons from protons up to  $0.8\ \text{GeV}/c$ . A high resolution on the impact parameter is important to reconstruct secondary vertices from hyperons and heavy-flavour (B and D mesons) hadrons decay. The material budget in the active volume has been kept to a minimum, to avoid worsening of the impact parameter resolution due to multiple-scattering effects. Fig. 2.10 shows the transverse impact parameter resolution as function of  $p_t$ , as measured in 2010 Pb–Pb collisions. The resolution in the  $r\phi$  plane is nearly  $50\ \mu\text{m}$  for  $1\ \text{GeV}/c$  particles and decreases at higher momentum. A small improvement in the resolution is reached in Pb–Pb collisions with respect to pp, as the high multiplicity of central Pb–Pb collisions implies a better primary vertex resolution.

The ITS can improve the momentum and angular resolution for tracks reconstructed by the TPC and allows to reconstruct tracks traversing dead TPC regions or very low momentum tracks that do not reach the TPC. ALICE exploits the ITS capability only with a dedicated tracking algorithm to recover very low momentum

particles. The main difference with respect to the global tracking, is the starting point. The ITS StandAlone (ITS SA) tracking starts from the primary vertex and it reconstructs tracks, matching the clusters coming from the different ITS layers through selected angular windows.

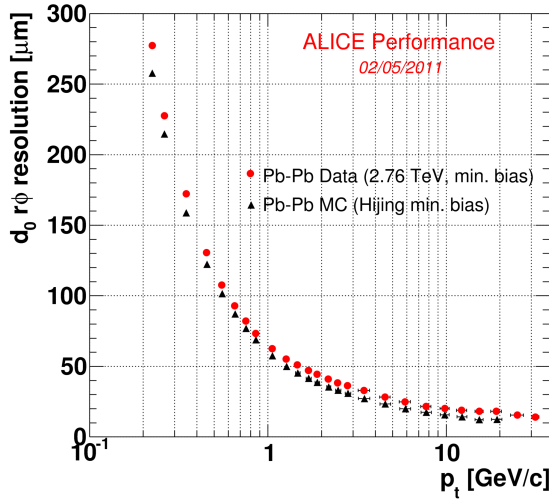


**Figure 2.10** Transverse impact parameter resolution as function of the particle transverse momentum, obtained for well reconstructed tracks having two measured points in the SPD. The resulting impact parameter resolution is the convolution of the track-position and the primary-vertex resolutions. Data (red dots) come from 2010 Pb–Pb dataset. Comparison with Monte Carlo simulation (black triangles) is also shown.

### 2.2.2 The Time Projection Chamber

The Time Projection Chamber (TPC) is the main tracking detector of the central barrel, covering the pseudorapidity range  $|\eta| < 0.9$  and the full azimuthal angle. The detector design was optimized given the necessity to provide excellent tracking performance in a high multiplicity environment, to keep the material budget as low as possible in order to have low multiple scattering and secondary particle production, to limit the detector occupancy at the inner radius but still guarantee a good momentum resolution for high- $p_t$  particles. The TPC is cylindrical in shape with an inner radius of 80 cm, determined by the maximum acceptable track density, and an outer radius of 250 cm, determined instead by the minimum track length for which the resolution on  $dE/dx$  is lower than 10%. The overall length along the beam direction is 500 cm. The TPC volume is filled with 90 m<sup>3</sup> of a mixture of C<sub>2</sub>H<sub>2</sub>F<sub>4</sub> (90%), i-C<sub>4</sub>H<sub>10</sub> (5%) and SF<sub>6</sub> (5%), optimized for drift velocity, low electron diffusion and low radiation length. A central cathodic plane divides the TPC in two drift regions. After ionization by a charged particle, the electrons drift toward the endcap readout planes. The electron drift velocity of 2.7 cm/s over 250 cm (each of

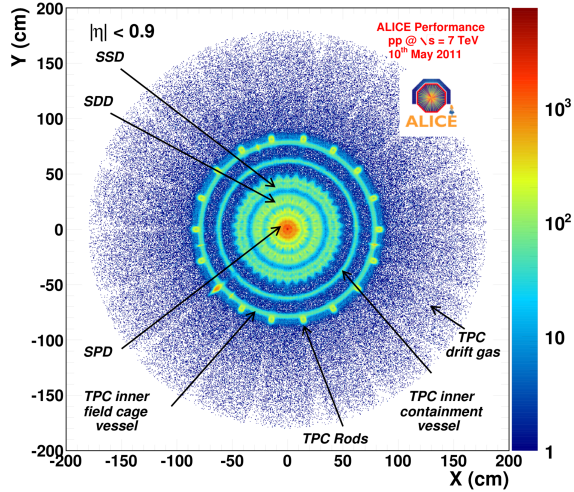


**Figure 2.11**  $x$ - $y$  distribution of reconstructed photon conversions measured in pp collisions. The measured data points correspond to the point of the conversion of a photon into a  $e^+e^-$  in the transverse plane, the counts indicating how often they converted at this point.

the two TPC drift region separated by the central cathode) gives a maximum drift time of  $88 \mu\text{s}$ , therefore setting a limit on the event rate sustainability of the TPC. At high interaction rate the pile-up effect becomes relevant. Although tracks from pile-up events can be rejected using cuts on the primary vertex position and arrival time, this is one of the main factors that also forces ALICE to run at lower instantaneous luminosity with respect to the other LHC experiments. Another limiting factor is the long TPC dead time, that slows down the readout frequency despite the fact that the slowest detector (in terms of readout electronics) is the SDD, with a busy time of 1 ms. The endcap planes are divided in 18 sectors along the azimuthal angle and house the multiwire proportional readout chambers (with cathod-pad read-out). The radial thickness of the TPC is of 3.5% of the radiation length,  $X_0$  at central rapidity and grows to 40% towards the acceptance edges. Figure 2.11 illustrates the  $x$ - $y$  distribution of reconstructed photon conversions measured in pp collisions. This is a “radiography” of the innermost region of the ALICE central barrel: the measured data points correspond to the point where a photon converted into a  $e^+e^-$  in the transverse plane, the counts indicating how often they converted at this point. Wherever the highest material budget, there the highest number of conversions.

The TPC is able to track particles in a wide momentum range, from about  $p_t \sim 0.1 \text{ GeV}/c$  up to  $p_t \sim 100 \text{ GeV}/c$  with good momentum resolution and efficiency  $> 90\%$  for  $p_t > 100 \text{ MeV}/c$ , where the limiting factor are the interactions in the ITS material. Measuring the deflection in the magnetic field, the ITS and the TPC are able to determine the momentum of the charged particles with a resolution better than 1% at low  $p_t$  and better than 20% for  $p_t \sim 100 \text{ GeV}/c$ , as reported in fig. 2.12.

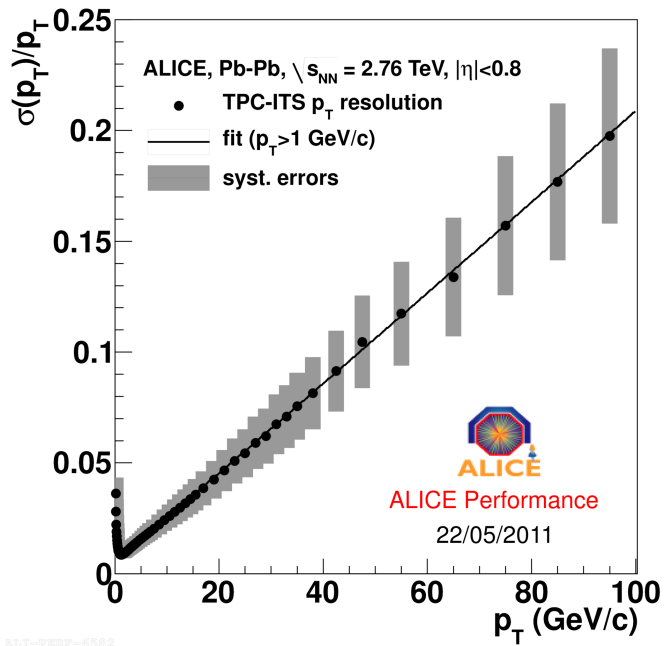


**Figure 2.12** Relative transverse momentum resolution for TPC+ITS combined tracking in Pb–Pb collisions at  $\sqrt{s_{NN}}= 2.76$  TeV.

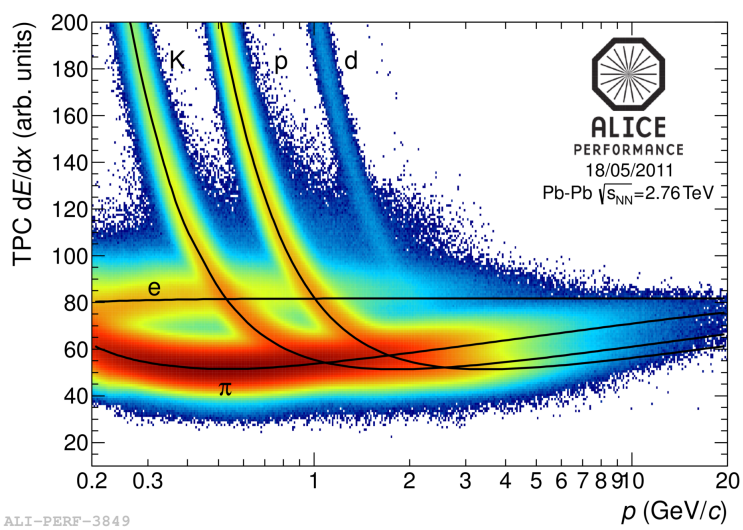


**Figure 2.13** Energy loss in TPC in Pb–Pb collisions at  $\sqrt{s_{NN}}= 2.76$  TeV.

The charge collected in the TPC readout pads is used to measure particle energy loss. The momentum measurement and the  $dE/dx$  information allow to separate the various charged particle species in the low momentum region: thanks to its good  $dE/dx$  resolution, the TPC can identify particles with  $p_t < 1$  GeV/c. An example of the TPC PID performance is shown in fig. 2.13, where the energy loss distribution for the different species is fitted by a Bethe-Bloch function, similarly to the ITS case.

### 2.2.3 The Transition Radiation Detector

The Transition Radiation Detector (TRD) is dedicated to the electron identification for  $p_t > 1$  GeV/c, below which electrons can be identified by the TPC via  $dE/dx$  measurement. When relativistic charged particles cross the interface of two media of different dielectric constant, transition radiation is emitted, with photons in the KeV range. Electrons with momentum above the threshold radiate differently with respect to pions, so the TRD can extend the pion rejection capability of the TPC up to very high momenta. The electron identification is crucial for the study of electrons  $p_t$  spectrum and light and heavy vector meson resonances ( $J/\Psi$ ,  $\Upsilon$ ,  $\Upsilon'$ ,...) through their leptonic channel decay.

The TRD is segmented along the azimuthal angle in 18 sectors, each containing 30 modules arranged in five stacks along  $z$  and six layers in radius. Each detector element consists of a radiator of 4.8 cm thickness, a drift section of 30mm thickness and a multiwire proportional chamber with pad readout. At present 13 TRD modules are installed (three of which were installed at the beginning of 2012) and cover the azimuthal angle  $0^\circ < \phi < 80^\circ$ ,  $120^\circ < \phi < 260^\circ$ ,  $300^\circ < \phi < 360^\circ$ .

### 2.2.4 The Time Of Flight

The Time of Flight (TOF) detector is dedicated to charged particle identification in the pseudorapidity region  $|\eta| \leq 0.9$ , by combining the measurement of the particle time-of-flight with the momentum information provided by the TPC. A total time resolution lower than 100 ps is needed in order to identify and separate pions and kaons up to 2.5 GeV/c and protons up to 4 GeV/c. Chapter 3 and 4 are entirely dedicated to TOF and its performance and more details are given there.

The TOF detector is a large double-stack Multi-gap Resistive Plate Chamber (MRPC) array covering the full azimuthal angle. The intrinsic time resolution of the MRPC is lower than 50 ps (from test beam studies) and it is dominated by the jitter in the electronics and the time resolution of the TDCs. The MRPC efficiency was measured to be close to 100%. The geometrical structure of the TOF is similar to that of the TRD, in such a way that the dead zones are superimposed: the detector is segmented in 18 7.5m long azimuthal sectors, or supermodules (SM), each of them containing five gas-tight modules displaced along the beam direction. The external and intermediate modules contain 19 MRPC, while the central contains only 15. The MRPC are also referred to as “strips”, due to their geometry. Each

supermodule contains the MRPC, the cooling and gas distribution system and the front-end readout boards. In each module, the strips are tilted with different angles, to minimize the dead zones and to be perpendicular to the trajectories of the particles coming from the IP, so to limit the occupancy and reduce the time resolution. Since each MRPC is composed of 96 readout pads, the TOF detector consists of 152928 readout channels ( $2.5 \times 3.5 \text{ cm}^2$  each) covering a total area of  $141 \text{ m}^2$ . This highly segmented structure allow to have a low occupancy and good performance also in a high multiplicity environment, such that of Pb–Pb collisions.

### 2.2.5 V0, ZDC and T0

The V0 detector is a small angle detector consisting of two arrays of scintillator counters, named V0A and V0C, installed on both sides of the ALICE detector at a distance of 340 cm from the IP on the side opposite to the muon spectrometer (V0A) and 90 cm from the IP (V0C) on the other side. Each array is segmented into 32 individual counters distributed in four rings and each connected with 1mm diameter Wave-Length Shifting (WLS) fibre, that guide the light to an Hamamatsu photo-multiplier.

The V0 provides the minimum bias trigger for the central barrel detectors in pp and Pb–Pb collisions together with the SPD, the centrality triggers (implemented since 2011) and an early “wake-up” signal for the TRD, prior to the level 0 trigger. V0 is also used to remove the collision background due to particles of the beam that interact with residual particles in the beam pipe, the so-called “beam-gas” background. Starting from the measurement of the number of particles reaching the scintillators, which is directly proportional to the ADC counts and correlated with the number of primary particles, the V0 provides an estimation of the centrality of the collision [13]. The correlation between the amplitude of the signal in the V0 detector and the track multiplicity in the TPC is reported in fig. 2.14, left. The V0 amplitudes are fitted with a model based on a Glauber description of nuclear collisions [?], in order to extract the average number of participant nucleons, needed by many measurements that aim to compare Pb–Pb and pp results. The model assumes that particles are produced according to a binomial distribution and the particle-producing sources are given by  $f \times N_{\text{part}} + (1 - f) \times N_{\text{coll}}$ , where  $N_{\text{part}}$  is the number of participant nucleons,  $N_{\text{coll}}$  the number of binary nucleon-nucleon collisions and  $f$  quantifies their relative contribution. The nuclear density for  $^{208}\text{Pb}$  is modeled by a Woods-Saxon distribution for a spherical nucleus with radius of 6.62 fm. The curve resulting from the fit of the V0 amplitudes is shown in fig. 2.14 right; more details can be found in [?].

The centrality of the collision can be alternatively estimated by detecting the spectator nucleons that keep their trajectory in the forward direction along the beam pipe. For this purpose two Zero-Degree Calorimeters (ZDC) are placed at 116 m on either side of the interaction point, very close to the beam pipe. The ZDC are also used to estimate the reaction plane in nucleus collisions and to reject parasitic

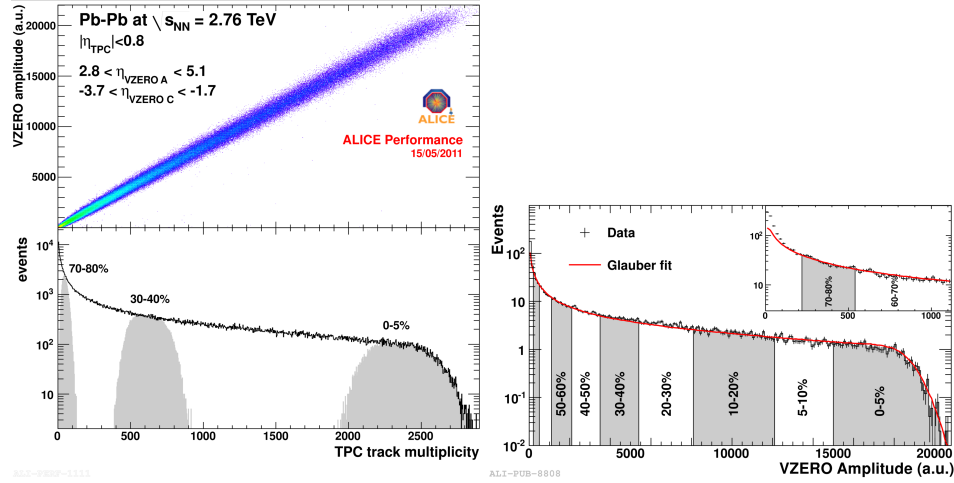


**Figure 2.14** Correlation between the amplitude of the signal in the V0 detector and the track multiplicity in the TPC, on the left. A Glauber model fit to the measurement is shown as the red curve on the right plot [?].

collisions<sup>3</sup>. Each ZDC is made of two calorimeters: one, for the spectator neutrons (ZN), is placed between the beam pipes; one, for the spectator protons (ZP), is located externally to the outgoing beam pipe where positive particles are deflected and separated by the neutrons by the magnets in the LHC beam pipe. Two small electromagnetic calorimeters (ZEM) are placed at about 7 m from the IP, on both sides of the LHC beam pipe, on the opposite side with respect to the muon spectrometer. The ZDCs are quartz-fibre sampling calorimeters, with passive element absorbers. The ZEM are used in particular to distinguish central from peripheral and ultra-peripheral collisions: in central collisions a small amount of energy is deposited in the ZDC, but similarly it could be the case for very peripheral collisions, where spectator nucleons can bind into fragments which don't get out from the beam pipe and cannot be detected from the hadronic calorimeters. The ZEM allow to discriminate between events with different centrality by measuring the energy of the particles emitted at forward rapidity that increases with the collision centrality.

The Time Zero (T0) detector consists of two arrays (T0A and T0C) of Cherenkov counters, 12 counters per array. Each counter is based on a fine-mesh photomultiplier tube, optically coupled to a quartz radiator with 20 mm diameter and 20 mm thickness. Like the V0, T0A is placed at 375 cm from the IP on the opposite side respect to the muon spectrometer, while T0C is located just in front of the absorber, at 72.7 cm from the IP. The Time Zero's main purpose is that of generating a start time ( $t_0$ ) for the TOF detector. This time corresponds to the real time of the colli-

<sup>3</sup>The ALICE detector is placed close to the injection line from SPS to LHC. At the injection between SPS and LHC, some small fragments of the bunch of the beams can fall in the wrong radio frequency bucket. When these fragments collide with the main bunch of the second beam, they can produce parasitic collisions displaced about 30 cm from the centre of the experiment.

sions and it is independent of the interaction point position. The T0 is used also for the online monitoring of the luminosity and to generate an early “wake-up” signal for the TRD, prior to the L0 trigger.

### 2.2.6 Muon spectrometer

The Forward Muon Spectrometer (FMS) has been designed to identify heavy-flavour vector mesons ( $J/\Psi$ ,  $\Upsilon$ , ...) as well as the  $\phi$  at forward rapidity, through their leptonic decay to  $\mu^+ \mu^-$  pairs. Quarkonia states exhibit invariant mass peaks very close to each other, which require a good mass resolution of the apparatus. The simultaneous measurement of all the quarkonia species allows a direct comparison of their production rate as a function of different parameters such as the collision centrality and  $p_t$ . Heavy-flavour production can also be studied through open charm and open beauty states semi-leptonic decay, that generate low momentum muons.

The muon spectrometer is located externally to the central barrel and covers the pseudorapidity region  $-4.0 < \eta < -2.5$ . A 3.5m long carbon conic-shaped absorber has been placed in front of the spectrometer, still inside the L3 magnet, to screen the detector from most of the primary and secondary particles produced in the interaction point. A high-granularity tracking system is composed by 5 chambers perpendicular to the  $z$  with two cathodic planes each, providing a spatial resolution of  $100 \mu\text{m}$ . Two out of 5 chambers are placed between the L3 magnet and the dipole. These are highly segmented in order to get a precise measurement of the exit point of the muons from the beam pipe and to keep the occupancy within 5%. One of the tracking chambers is housed by a large dipole magnet, that provides a 0.67 T horizontal field perpendicular to the beam axis. The last four tracking planes are placed outside the dipole. The trigger system (MTRG) is given by four planes of Resistive Plane Chambers (RPC) operating in streamer mode. The MTRG is placed after a 1.2 m thick iron filter-wall, that allow only muons with  $p > 4 \text{ GeV}/c$  to reach the trigger chambers. Finally an inner beam shield protects the spectrometer from secondaries produced at large rapidity.

## 2.3 ALICE online operations

### 2.3.1 Data AcQuisition system

The data taking activities are controlled by the central online systems: the Detector Control System (DCS) allows to operate the detector hardware from a central interface, the Data Acquisition (DAQ) system is responsible of defining the configuration of the detectors during data taking and it is interfaced with the Trigger (TRG), and High-Level Trigger (HLT) systems. All the operations of the central systems are coordinated by the Experiment Control System (ECS). The detectors can operate individually, in “standalone mode”, to perform commissioning, calibration and debugging activities, while during the physics data taking, the detectors

are grouped in “partitions” that can operate concurrently and independently, receiving a given set of trigger inputs. The ECS has several components, among which the Detector Control Agent (DCA) handles the acquisition in standalone mode, the detector electronics setup and the calibration procedures and the Partition Control Agent (PCA) handles the partition structure, allowing to include and exclude the detectors in the partition, with the limit that a detector can active in one partition at a time. The ECS monitors the detector DCS status, interacts with the DAQ and the HLT processes and links the partition with the Central Trigger Processor (CTP), in case of a global partition, or with the detector Local Trigger Unit (LTU) in case of a standalone mode.

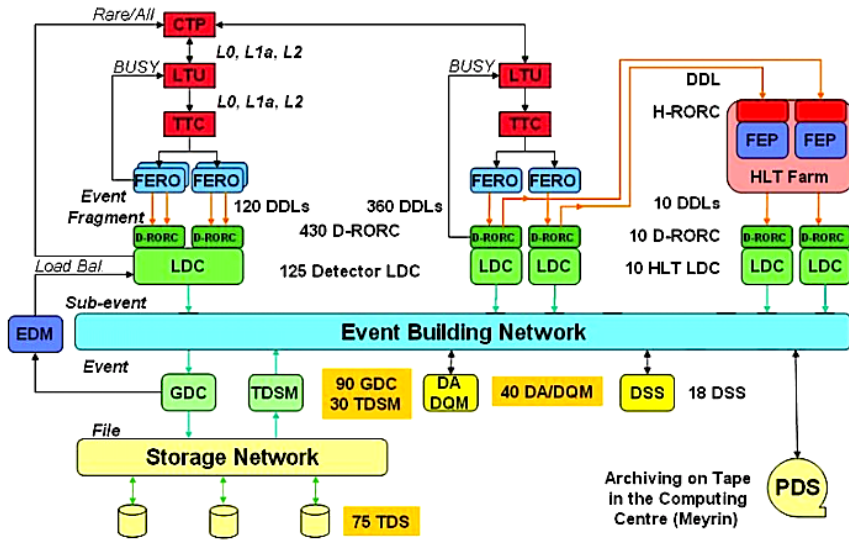


**Figure 2.15** Schema of the ALICE DAQ data flow.

The physics program of ALICE implies the study of a large variety of physical observables, with very different beam conditions. The whole system needs to be flexible enough to record central collisions, which generate large data size events, and to acquire the largest possible fraction of rare events at the same time. The interesting events are selected and characterised by a large number of trigger classes, divided in two broad categories, frequent or rare, for which a different fraction of the total data acquisition bandwidth has been allocated. Minimum bias and centrality triggers are so frequent that the limiting factor is the performance of the data acquisition system. These triggers use the largest fraction of the bandwidth. Rare triggers such as di-muon or di-electron events, use less bandwidth and are limited by the detector live-time and the luminosity. The ALICE DAQ [62, 64] was designed to give different observables a fair share of the trigger and DAQ resources, with a bandwidth of 1.25 GB/s to mass storage, considering 8kHz interaction rate at the nominal luminosity. A combination of higher selective triggers, data compression and partial readout strategy has also been applied to satisfy the

physics requirements with this bandwidth. The scheme of the Data Acquisition system flow is depicted in fig. 2.15. The throughput can be easily scaled in order to maximize the recording of rare events and the modifications can be applied in short time without any modification of the architecture. The system layout is designed so that the event loss for the detector readout dead time and for the transfer limitations through the buffer chain are due uniquely to the hardware properties of the detectors.

During the data taking, the detectors receive the trigger signal from the CTP through the LTU that is interfaced to the Timing Trigger Control (TTC) system. The data collected by the detector modules are sent from the detector electronics to the DAQ Readout Receiver Card (D-RORC) through the Detector Data Link interface (DDL). The D-RORCs are FPGA1 readout boards that interface each DDL with the Local Data Concentrators (LDC). Each detector's front-end system (FERO2) or D-RORC is responsible for sending a “busy” signal to the CTP. The data are sent in fragments from the DDLs to the LDCs, where they are put together in sub-event structures. If the data has to be analysed by the HLT, they are sent via the H-RORC, the HLT Readout Receiver Card, from the LDCs to the Front-End Processors (FEP), where, after the online analysis, a decision about the event is taken and, in the positive case, the data are transferred back to the LDCs via the D-RORC. The LDCs dispatch the sub-events to the Global Data Collectors, the GDCs, whose task is to build the full events in the format of ROOT files and to store the data in the Transient Data Storage (TDS), from where they are exported to the computing centre and recorded to the Permanent Data Storage (PDS).

The DAQ system exploits the feature of the Data Acquisition and Test Environment software, DATE [65]. As described above, the data flow is organised in parallel data streams processed independently in every node (LDC or GDC) and followed by an event builder stage where data are merged and recorded as completed events. The DATE framework has been designed to run on several machines with the Scientific Linux CERN operating system and it consists of a collection of software packages that are in charge of the data flow formatting, the event building, the data recording, the management of the configuration states, the error and log messages report, the electronic logbook and the monitoring.

Finally, the DAQ system includes a special framework that is dedicated to perform detector calibration procedures online, to allow a faster data analysis once offline. The interested detectors are allowed to run the calibration code on DAQ machines, through processes that are called Detector Algorithms (DA) . The DAs are connected with the data sources (LDCs processes or files) using the same monitoring libraries that enable the data readout (from files or from the LDCs). When the run is taken in a standalone mode, the data are recorded locally on the LDCs and analysed at the end of the run; when the calibration data are collected during a physics run, the DAs run on a particular machine called monitoring server. In this case, histograms of the distribution of calibration parameters are created by the DAs. The results can be sent immediately to the interface called File eXchange Server (FXS) or stored in the LDCs for configuring the electronics of the given detector or

exported to the DCS via the FXS. After the DA output is transferred from the DAQ system to the FXS, from there data can be archived in the offline database (Offline Condition DataBase - OCDB) by the SHUTTLE framework [66]. The SHUTTLE acts as interface between the online systems and the offline computing resources. It processes the condition data<sup>4</sup> present in the FXS, converting them into ROOT format and archiving them in the OCDB on the Grid where they can be retrieved during data reconstruction or analysis offline. In particular, the OCDB contains all the information about the detector status and the environment variables that have to be available at the beginning of the reconstruction.

### 2.3.2 Data Quality Monitoring online

Given the sophistication of the detectors and the variety of running conditions, Data Quality Monitoring (DQM) online is an important aspect of all the experiments at the LHC, aiming to avoid recording low quality data and help early recognition of potential issues. The ALICE DQM [?, 68] framework provides an online feedback on the quality of the data being recorded by analysing and visualising the produced monitoring information. The Data Quality Monitoring is part of the ALICE Data Acquisition (DAQ) system (see fig. 2.15), where the DQM software runs on dedicated servers connected to the event building network. In particular, the DQM processes can be fed with data from LDCs if data coming from a specific detector equipment need to be monitored, or from GDCs if the interest is on global observables of the whole event, such as trigger rates and event data size.

#### The Automatic MOnitoRing Environment software

The DQM software is named AMORE, acronym for Automatic MOnitoRing Environment. It is a flexible and modular software written in C++ and based on the DATE monitoring library and the ROOT [69] data analysis framework. The modules optionally include the ALICE offline framework (AliRoot) libraries, which allows to run the same analysis online and offline, as for example it happens with the AliRoot libraries needed to decode the raw data. The DAQ software, DATE, provides a low-level monitoring package which forms the basis of any high-level monitoring framework for ALICE. The access to raw data online on the DAQ nodes is possible via an Application Programming Interface (API), that is in also in charge of selecting the event sampling strategy.

AMORE is based on a publisher-subscriber paradigm (see fig. 2.16) where a large number of processes, called “agents”, execute detector specific decoding and analysis on data samples. Data samples are represented by sub-events coming from LDCs, GDCs or raw data files. The analysis results are usually ROOT histograms encapsulated in Monitoring Objects (MO), together with the additional information that allow their proper handling by the framework. Each detector’s specific

---

<sup>4</sup>The condition data represent the information on the current data taking, including beam information, trigger and data taking configuration, detectors calibration parameters or thresholds, ... .

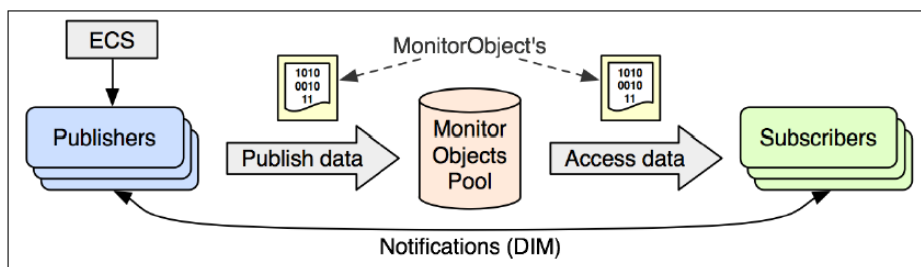


**Figure 2.16** The publisher-subscriber paradigm of AMORE.

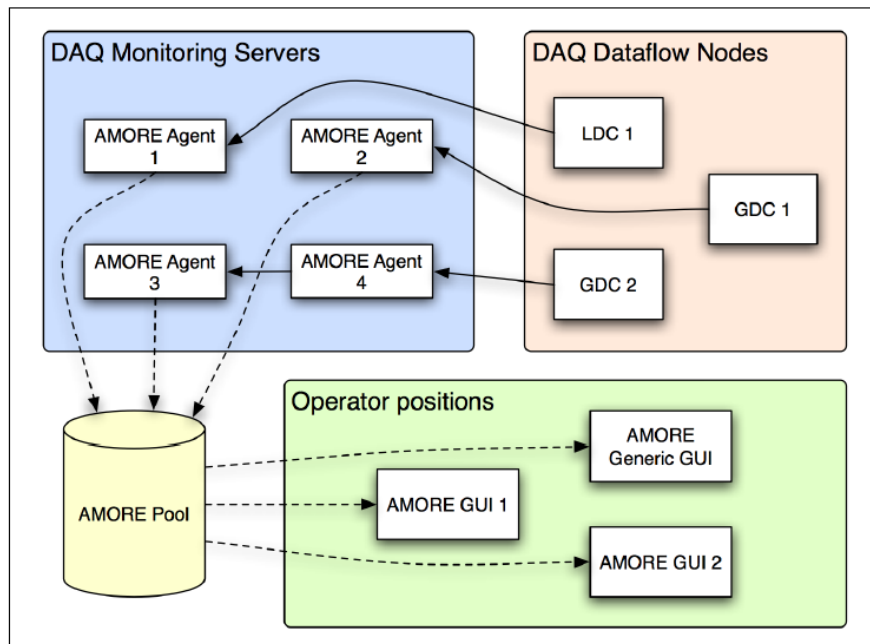


**Figure 2.17** The AMORE interaction with the DAQ nodes. The AMORE agents on the DAQ monitoring servers retrieve data from the LDCs or GDCs and send the output monitoring objects to the AMORE pool. The Operator position retrieves the information from the pool and visualises the results on the GUI.

code is built within dynamic libraries, defined “modules”, that are loaded at run-time by the framework only if needed. The modules are typically split into two parts corresponding to the publishing and the subscribing sides of the framework. The modules publisher can be instantiated several times, to collect more statistics per instance, each instance corresponding to an agent. The publishers analyze the raw data and publish them in a pool. The client consists of a ROOT-based Graphical User Interface (GUI) in which the MOs retrieved from the pool are displayed as drawn in fig. 2.17. The MOs are then displayed in a GUI to the operators. The communication between publishers and clients consists of notifications by means of the Distribution Information Management (DIM) [70] service. A similar strategy is used for the notifications coming from the ECS.

The data pool is implemented as a MySQL database. It contains several information, including a list of all the available agents and their configuration and the list of machines that host each process. The database contains also the configuration files, listing available options associated with each module that can be used to configure running parameters and/or thresholds for the automatic monitoring checks. Objects published by each agent are stored in a dedicated data table within the database.

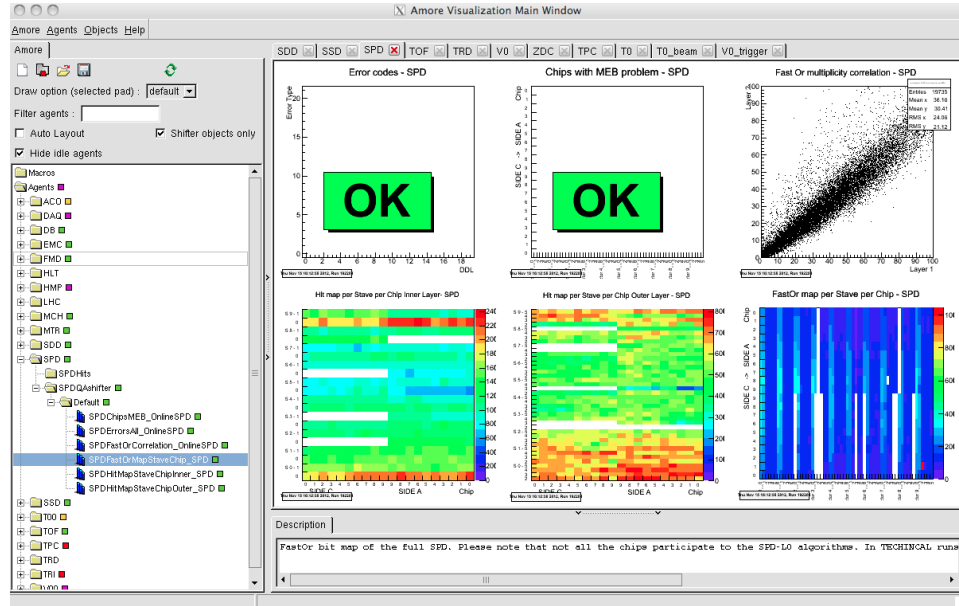


**Figure 2.18** The AMORE Graphical User Interface displaying the SPD monitoring histograms. On the left, the folders in the ROOT tree collect all the available monitoring objects, grouped by event species for each agent of each detector.

Most of the detectors use the AMORE Quality Assurance (QA) module that delegates the data processing to the AliRoot QA framework (see also section 2.4). This implies several consequences:

- the QA framework defines 4 event species: Calibration, Low Multiplicity,

High Multiplicity and Cosmic. For DQM purposes, the species are computed online by accessing the information on beam type, trigger and event type. The plots are duplicated 4 times accordingly but only those belonging to the actual species are filled. Only the “default” species is displayed to the operator and saved in the ALICE logbook. Typically the default corresponds to the species computed online. However, it could be statically associated with one of the four species independently of the value computed online.

- The QA framework includes a QA checker class to assess the quality of an object by comparison with some reference distribution or threshold. The species quality flag is retrieved and displayed in the GUI together with proper alarms and messages for the operator during data taking (see 2.18). The quality is stored within the object and can assume different values such as
  - kNULL, meaning no quality is assessed,
  - kINFO for good quality,
  - kWARNING suggesting that the object should be checked,
  - kERROR for the object that is clearly out of the reference,
  - kFATAL, when the object is so incorrect that measures must be undertaken quickly.
- There are two variants of the QA publisher class : PublisherQA and PublisherQAshifter. The latter inherits from the former and publishes only the subset of histograms that are flagged as dedicated to non-expert in the QA framework.
- The QA framework allows users to split their histograms by trigger classes. The AMORE module provides this feature by means of configuration files, one that defines trigger class aliases for their corresponding trigger classes and one that lists the histograms to be cloned and for which class.
- Thresholds for the automatic checks can be defined in the QA and their value can be changed online via proper configuration files. The QA framework allow to store the threshold values in the OCDB for future use offline.

During data taking the events are sampled by monitor cycles commonly lasting 50 s. At the end of each cycle, when the data collected are analysed by the agents, the DQM histogram are updated in the database and displayed in the GUI, feeding the operator’s attention with new monitoring information nearly every minute. Every hour (plus at Start and End of run), a copy of the MOs is also temporarily archived in the alice Logbook. The objects stays there for a week before being deleted, unless they are marked as permanent. It is indeed important for the experts to be able to check and study the objects even after the data taking has stopped. AMORE has been in production since spring 2008 and since then it has been successfully used, both during commissioning and physics data taking. It proved to

be very useful to test and monitor detector conditions and data format, as well as running conditions and configuration, physics observables and signals, quantities related to beam conditions and trigger patterns. The system has been evolving during all the data-taking phases. Thanks to the continuous interaction between the users and the framework developers the whole DQM system has been adapting and integrating new tools to cope with the circumstantial needs. The example of the Time-Of-Flight online monitoring strategy will be given in the next chapter.

## 2.4 ALICE offline computing

The ALICE offline framework (AliRoot) [71] is an object-oriented software framework, based on the ROOT system [69] and complemented by the AliEn [72] interface which gives access to the computing Grid. Entirely written in C++, except for a few internal modules in FORTRAN, the framework gives to the user the flexibility to perform Monte Carlo simulation, reconstruction, calibration and analysis with the same tool.

Given the unprecedented amount of data collected at the LHC and the computational cost of data processing, the worldwide Grid distributed computing system is the ideal stage to host this unprecedented effort. The ALICE Collaboration has developed the AliEn (ALICE Environment) framework [72] to reconstruct and analyze the data in a distributed environment. AliEn provides a global file system, or catalogue, for data storage and an interface to execute the jobs on the Grid. A distributed system, such as the Grid, allows to split the jobs analysis into many identical subjobs that run in parallel on different computer nodes. Users can implement custom analysis code or run the AliRoot analysis tools on the available datasets by specifying the version of the AliRoot or ROOT packages deployed on the Grid. The AliEn interface can be used to distribute and to monitor the progress of the jobs. The ALICE Virtual Organization (VO) is composed of more than 80 sites distributed all over the world. The software programs run on Worker Nodes (WN) machines, while the Storage Elements (SE) are responsible for managing physical files in the site and providing an interface to the mass storage. The Computing Element (CE) service is an interface to the local WN batch system that manages the computing resources of the site.

### Simulation

The simulation of physics events is of fundamental importance for any preliminary study and for evaluating the performance in terms of efficiency of the algorithms applied to reconstruct and analyse data. The event simulation is also a challenge for the computing resources, especially when simulating certain types of events (for example high-multiplicity or central Pb–Pb collisions) requires a large amount of CPU time and most often the statistic needs to be comparable to that of the data. For this reason, Monte Carlo data production in ALICE is performed on the GRID.

A realistic simulation should include the particles produced in a given collision as well as the propagation inside the detector (material absorption, acceptance, detector configuration, ...) and its response.

AliRoot is interfaced to several Monte Carlo generators, HIJING [73] and PYTHIA [54] among others, that supply particle production in the simulated collision. All the information about the generated particles (type, momentum, production process, decay products) are organized in a kinematic tree, stored in a ROOT file. The framework can also handle the generation of underlying events, rare signals through external generators (if need be), “cocktails” by combination of signals produced with different generators and beam-gas interaction events.

The generated particles are propagated through the sensitive regions of the detector, where they decay, loose energy, or interact with detector material, producing other particles or being absorbed. The detector layout, including geometry, position, structure and material is reproduced by using the ROOT libraries. The interaction of the particle with the material is simulated by the GEANT3 [74], GEANT4 [75] and Fluka [76] packages. Any interactions of particles with sensitive detector elements are recorded as hits, carrying information on position, time, energy deposit and reference to the corresponding track. By combining the detector and the electronic response information, a digital output is associated to a hit and stored as a summable digit. Finally digits are translated into the same format of raw data, ready to be the input for the same tracking process that is followed for real data reconstruction.

### Tracking

The first step of the reconstruction is a local cluster finding procedure, executed by each detector within its own sensitive volume. The signals of particles crossing the sensitive area are usually detected by neighbouring detector elements, that are combined into a single cluster to better estimate the position of traversing particle and reduce the effect of the random noise. The cluster information is saved in temporary trees with the format of “rec points” and is at the basis of the subsequent tracking procedure.

ALICE exploits the Kalman Filter algorithm [77] for simultaneous track finding and track fitting. Each track candidate is represented by a state vector and the algorithm is a recursive procedure to determine the status of the track based on a finite number of measurements at given positions (the active volume of the detector). The evolution of the status between two points along the track is given by a deterministic component, namely a locally linear equation of motion, and by a stochastic component, to account for multiple scattering. For each vector that enters the evolution equations a covariance matrix is defined and evolves accordingly.

The ALICE track reconstruction is based on the following steps [78]:

- the position of the primary vertex is needed to build the “track seeds” that are used as starting points for the Kalman filter. The clusters in the two ITS

inner layers are used for the primary vertex reconstruction. More details on the vertexing algorithm can be found in [79, 80].

- The track finding in the TPC proceeds from the outer to the inner part. The outermost pad rows and the primary vertex position from previous step are used as seed. A limited number of TPC cluster is associated to the track with the “center of gravity” method.
- For each seed the track following is performed: the state vector and the covariance matrix are propagated as mentioned before along the pad rows. At this stage no constraint on the primary vertex is applied, in order to maximize the efficiency for primary tracks.
- Starting from the higher-momentum candidates, the TPC tracks are matched to the SSD layers and with ITS points down to the innermost SPD layer.
- The track is then back-propagation and refitted outward in ITS and TPC, up to the outer radius of the TPC.
- The next step is the extrapolation and track matching in the TRD, followed by the propagation to the outer layer to the PID detectors, TOF, HMPID, PHOS and EMCAL. The track extrapolation to the TOF is discussed with more details in section 4.2, because of its importance for any analysis involving the TOF PID, as the one presented here.
- Reconstructed tracks are refitted inward through TRD, TPC and ITS and re-propagated to the primary vertex. The track parameters are constrained, that is evaluated in proximity of the vertex.
- The primary vertex position is finally recalculated using tracks to obtain the optimal resolution.

The output of the whole reconstruction operation is the Event Summary Data (ESD) which contains all the information about the event both at track or event level. Technically, the ESD is a tree with objects of type AliESDEvent stored in the AliESD.root file. In order to allow a more efficient analysis a summary of the most relevant information is extracted from the ESDs in the format of Analysis Object Data (AOD). For each data sample, the files containing ESD and AOD are stored and distributed worldwide on the Grid, where the users can access them through AliEn, the ALICE Environment framework.

### **ITS+TPC tracking performance**

The prolongation tracking efficiency between TPC and ITS is shown in fig. 2.19, as a function of the transverse momentum. It has been studied in minimum bias Pb-Pb events by using the TPC tracks as a reference and looking for the prolongation in the ITS [81]. The prolongation efficiency is above 97% in the whole momentum

range (black points) when at least two points in the ITS are required. The efficiency exhibits a drop to 85% if one of the two points is constrained to be in the pixels detector (red points), due to the presence of inactive modules in the SPD. Fig. 2.19 also shows an agreement well within 2% between the Monte Carlo HIJING simulation (empty markers) and the data. It is interesting to recall that despite the difference in the event shape and multiplicity, the ITS reaches the same tracking performance in pp and Pb–Pb collisions [80, 81], thanks to the high segmentation and the low material budget.

The performance of the global TPC+ITS ALICE tracking in terms of transverse momentum resolution is reported in fig. 2.12: the resolution is about 10% for tracks of about 50 GeV/c and goes well below 3% for tracks below 10 GeV/c.

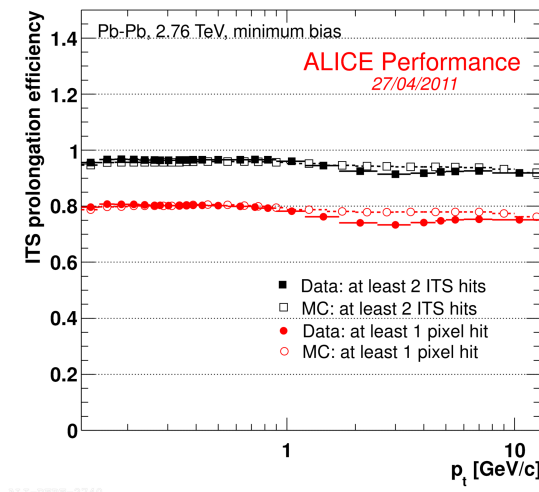


**Figure 2.19** TPC-to-ITS prolongation efficiency Pb–Pb collisions (full markers) compared with Monte Carlo simulation (empty markers). Black points correspond to the efficiency in the case that two points are in the full ITS, red points to the case where one hit in the pixels detector is required.

### Data quality assurance offline

The AliRoot Quality Assurance (QA) framework is aimed to provide an automatic way to assess the quality of the data at various level of Monte-Carlo simulation and Monte-Carlo and real data reconstruction. The various levels include Raw data, SDigits, Digits, RecPoints and ESDs. QA data objects are produced as ROOT histograms and are stored in a ROOT file. The comparison of these objects with either user defined values or with user defined reference result in a quality statement, as already mentioned in 2.3.2. More precisely, the result of the checking is represented per detector as a severity level in a bit map and stored in the QA object (AliQA). Each histogram is automatically cloned for the various Event Species (kLowMult,

kHighMult, kCosmic and kCalib) and for the activated trigger classes. The statistics of the QA data objects is user defined. The number of events to process defines a cycle. A run can include several cycle and a cycle can span over several run. Since a run can include several event species, the filling of the histograms according to the event species is controlled by the framework.

## Chapter 3

# The ALICE Time-Of-Flight detector

The Time Of Flight (TOF) is one of the main detectors of the ALICE central barrel, with a fundamental role in particle identification as well as in the trigger of the experiment. The TOF measures the time needed by the particles produced in the interaction point to travel from the primary vertex to its sensitive surface. This information is combined with that of the particle momentum  $p$ , provided by the tracking detectors to estimate the mass  $m$  of the particle according to the relativistic relation:

$$m = \frac{p}{\beta\gamma} = p\sqrt{\left(\frac{ct_{TOF}}{L}\right)^2 - 1} \quad (3.1)$$

where  $L$  is the measured track length,  $\beta = v/c$  and  $\gamma$  is the Lorentz factor. The corresponding mass resolution is

$$\left(\frac{dm}{m}\right)^2 = \left(\frac{dp}{p}\right)^2 + \gamma^4 \left[ \left(\frac{dt_{TOF}}{t_{TOF}}\right)^2 + \left(\frac{dL}{L}\right)^2 \right]. \quad (3.2)$$

If we consider the track length known with a precision of  $dL/L \sim 0.1\%$  and the momentum with  $dp/p \sim 1\%$ , the mass accuracy is determined by the resolution on the time-of-flight measurement. In order to achieve  $dt_{TOF}/t_{TOF} \sim 1\%$  for a particle that travels a 3 m lenght in 10 ns, a  $\sim 100$  ps resolution on the time-of-flight is needed. At the same time, the separation between two particles with same track length, same momentum, but different masses ( $m_1$  and  $m_2$ ) can be expressed in terms of the number of standard deviations between the two time-of-flight measurements:

$$n_{sd,1-2} = \frac{\Delta t}{\delta t} = \frac{L}{2c} \frac{(m_1^2 - m_2^2)}{p^2 \delta t}. \quad (3.3)$$

$\delta t$  is the total resolution of the TOF detector ( $\delta t = dt_{TOF} = \sigma_{TOF}$ ), given by several contributions:

$$\sigma_{TOF}^2 = \sigma_{MRPC}^2 + \sigma_{TDC}^2 + \sigma_{Cal}^2 + \sigma_{Clk}^2 + \sigma_{t_0}^2 \quad (3.4)$$

where

$\sigma_{MRPC}^2$  is the intrinsic resolution of the Multigap Resistive Plate Chambers (MRPC),

$\sigma_{TDC}^2$  is the intrinsic resolution of the readout boards, due to the signal digitalisation,

$\sigma_{Cal}^2$  summarises the uncertainties on the calibration constants, such as the cable lengths and paths on the readout boards,

$\sigma_{Clk}^2$  accounts for the delay of the trigger signal distribution to the electronics,

$\sigma_{t_0}^2$  is the resolution to the measurement of the interaction time.

The initial time of the collisions, referred to as “time zero” ( $t_0$ ) is obtained in different ways in ALICE, that will be described later (section ??), together with the PID performances. The design of the detector has been optimized as described in section 3.1 by keeping in mind these contributions and constraints. In sections 3.1.2 and 3.1.3 details of the TOF front-end and readout electronics, respectively, will be given. Section 3.2 is dedicated to illustrate the tools for data and detector behaviour online monitoring, while discussing the features on the TOF signal.

### 3.1 The Time Of Flight detector

The TOF [82, 62] is a large MRPC-array located in the ALICE central barrel at a distance of 3.7 m from the beam line, externally to the TRD. Its geometrical acceptance covers the pseudorapidity region  $|\eta| \leq 0.9$  and the full azimuthal angle, as already briefly described in section 2.2.4. The 18 TOF supermodules (SM) are housed in the ALICE “space-frame” structure, as shown in figure 3.1. Each of them is parallel to the beam line and covers approximately  $20^\circ$  of azimuthal angle, correspondingly to each TRD module. Each SM is 9.27 m long (9.5 m including the readout crates), weights of 1.45 metric tons and is divided in 5 gas-tight modules<sup>1</sup> along the beam axis. Two custom VME crates containing the readout electronics are placed at both ends. Figure 3.2 is a picture of a fully assembled TOF supermodule before installation: two out of four readout crates are visible as well as a fraction of the front-end boards.

All the modules have the same width (128 cm) but an increasing length going from the centre to the end of the SM: the two external and two intermediate modules contain 19 MRPC (or strips) each, while the central one includes 15 strips, for a total of 91 MRPC per SM. The strips are oriented parallel to the  $x$  axis and have 96 readout pads, divided in two rows along  $z$ , each of them with 48 pads. In total,

---

<sup>1</sup>The SM covering the azimuthal angle  $240^\circ \leq \phi \leq 300^\circ$  were installed without the central module in order to reduce the amount of material in front of the PHOS calorimeter.

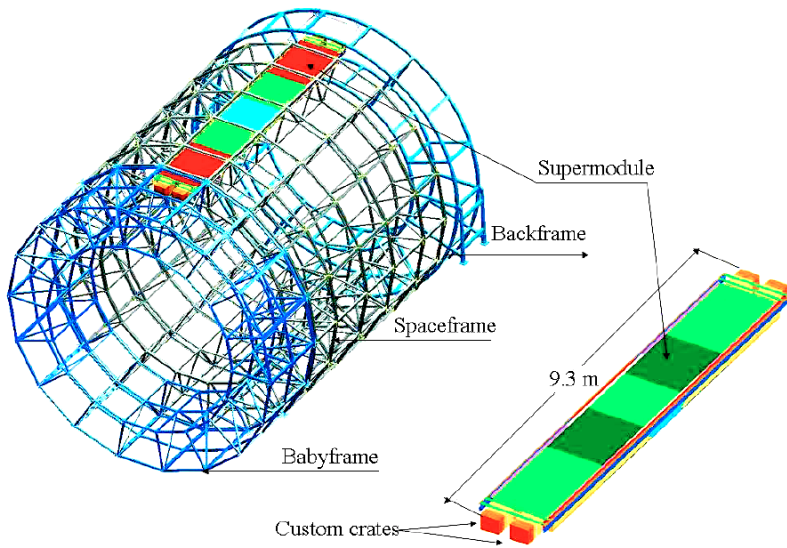


**Figure 3.1** View of a TOF supermodule, housed in the ALICE space-frame. The orange boxes represent the readout crates.



**Figure 3.2** Picture of a TOF supermodule, before installation. Two out of four readout crates are visible, as well as some of the front-end cards, to be enclosed completely by the top aluminum black covers.

the TOF has 152928 readout channels covering a total area of 141 m<sup>2</sup>. A module can be considered as divided in two volumes, one containing the gas and the MRPC, and one containing the Front-End electronics (FEA). Inside each module, the MRPC are displaced in such a way that their active area is overlapped by 2 mm, while they're slightly tilted with respect the horizontal position in order to minimize the dead areas and to be as perpendicular as possible to the direction of the incoming particles produced at the interaction point. An example is reported in fig. 3.3 for one of the intermediate modules; the figure also show how the overlap regions between two adjacent modules ensure good coverage.

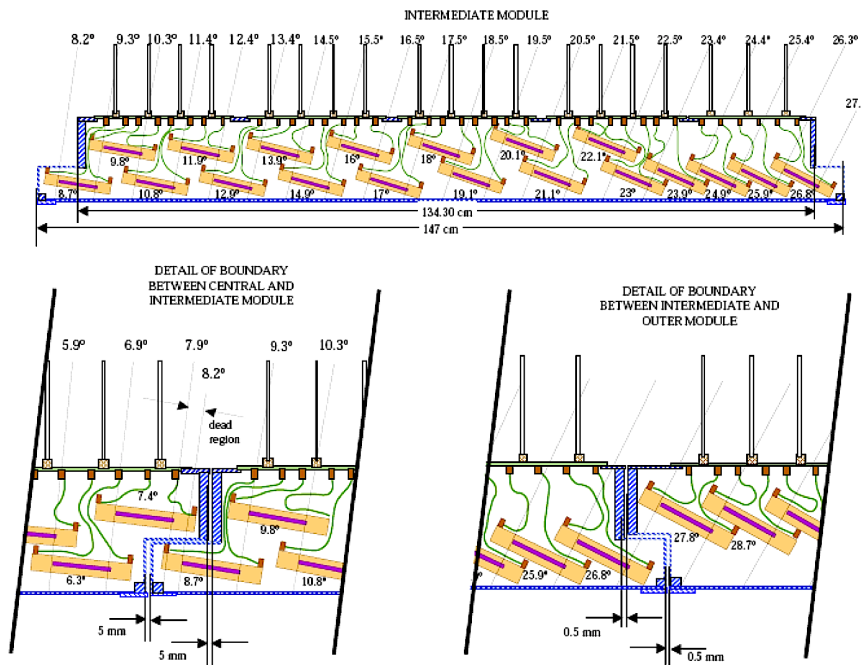


**Figure 3.3** Lateral view of one TOF intermediate module with its 19 strips. The MRPC are tilted by small angles for their plane to be perpendicular to the incoming particles and they overlap by 2 mm in order to avoid dead areas. Similarly, also the strips from two adjacent modules end up being superimposed, granting in this way an optimal coverage also in the boundary zones.

### 3.1.1 The Multigap Resistive Plate Chambers

The choice of using Multigap Resistive Plate Chambers [83] as basic unity for the TOF comes from the possibility of achieving very low intrinsic time resolution, not bigger than  $\sigma_{MRPC} \sim 50$  ps, while operating in presence of a high track multiplicity and potentially high detector occupancy in Pb–Pb collisions at the LHC.

The MRPCs are an evolution of the Resistive Plate Chambers (RPCs). A RPC is constituted by two parallel high-resistivity electrode planes that provide a uniform

electric field, filled with a proper gas mixture. The charged particle that traverses the active area, ionises the gas creating positive ion-electron pairs. In presence of a sufficiently strong electric field, the fast electrons migrating towards the anode can generate an avalanche in the gas. The movement of the charge in the electric field gives the signal that is read by the electronics. The intrinsic time resolution is defined as the indetermination on the time needed by the drift electrons to generate a signal above threshold on the pads. The larger the gap between anode and cathode, the longer the time available for the avalanche formation, the wider the spatial projection of the avalanche on the readout planes, the worse the time resolution for a time-of-flight measurement. The RPC technology, with a parallel plate configuration, already presents some advantages with respect to a traditional wire chamber with a radial electric field: since the field is uniform, the electrons do not have to travel before to reach the region where the field is strong enough to produce an avalanche. This means that there is no time uncertainty related to the primary ionization point in the volume. This however determines the amount of charge produced and therefore it is strongly related to the efficiency.

The fluctuations of the development of the avalanche are given by two factors: on one side the width of the gap or the intensity of the electric field can be adjusted to tune the produced amount of charge. On the other side, the choice of the gas affects instead the poissonian distribution of the primary ion pairs. In presence of abundant particle streams, as it could be the case in Pb–Pb collisions, the spatial charge effect on the resistive planes and the subsequent decrease of the effective electric field are the main causes of inefficiency for the RPCs. To solve this problem one could try to favour the charge dissipation, by using lower-resistivity planes, but that would induce a signal in a larger number of readout pads, therefore worsening the spatial resolution.

A compromise between the time resolution and efficiency requirements has been implemented with the TOF double-stack Multigap RPCs. One MRPC stack is a chamber formed by two parallel resistive planes where the gap between the electrodes is divided in a given number of smaller gaps by electrically floating high-resistivity planes, that are transparent to the fast signals coming with the electrons. The avalanche induced by the passage of ionizing radiation stops at each intermediate plane in such a way that its dimension is constrained and the time resolution is improved. The signal on the pickup electrodes is induced by the movement of the fast electrons towards the the anodic planes and it is the analogue sum of the signals given by each avalanche. The the active volume of the detector is simply the sum of each gap. In a double-stack MRPC, two single MRPCs share the anodic plane: the electrodes are closer so that border effects between adjacent pads are smaller and the number of gaps can be increased while the applied potential difference (ddp) can be half. Figure 3.4 depicts the transverse section of a TOF double-stack MRPC. Each MRPC is a strip of  $7.4 \times 122 \text{ cm}^2$  area, segmented in 96 readout pads as previously mentioned. The external planes are  $550 \mu\text{m}$  thick glasses with surface resistivity  $\rho = 2 \div 25 \text{ M}\Omega/\square$ . The High Voltage (HV) is applied through electrodes connected to their external surface. The Printed Circuit Boards (PCB)

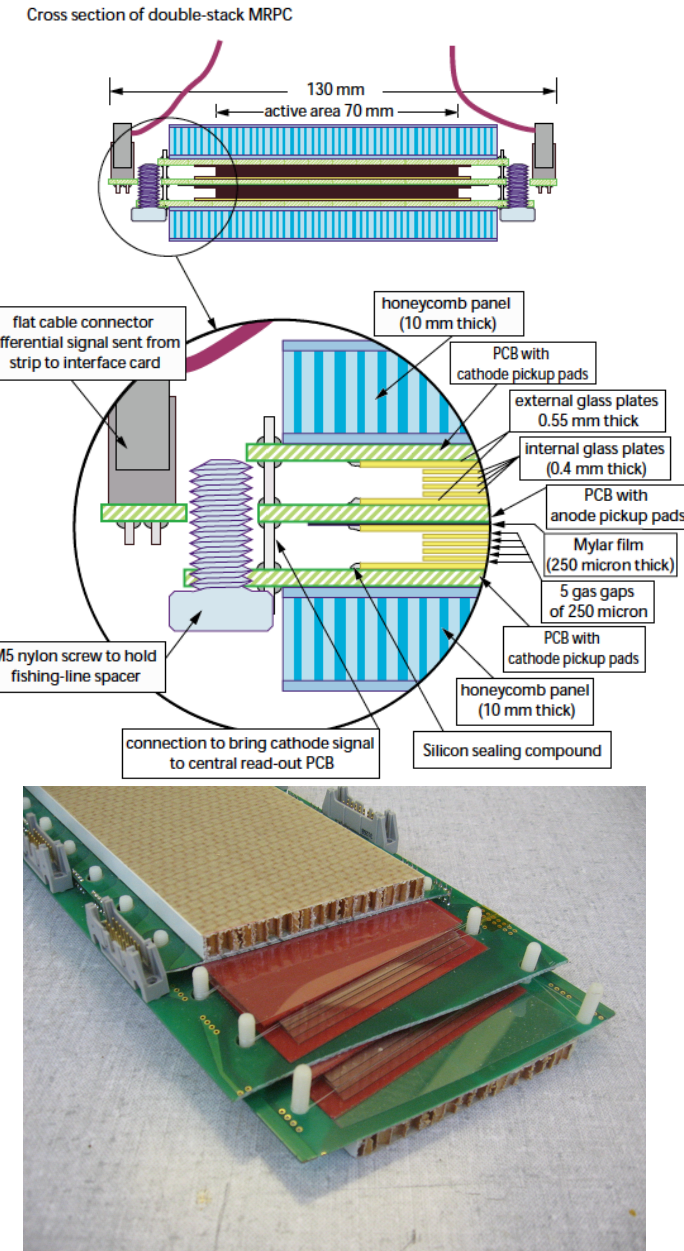


**Figure 3.4** Section of one TOF MRPC.

with the readout pads are layered externally together with the honeycomb panels that maintain the rigidity of the system. The five gaps per stack are created by four internal glasses, 400  $\mu\text{m}$  thick, that are kept at a distance of 250  $\mu\text{m}$  by a Mylar fishing line.

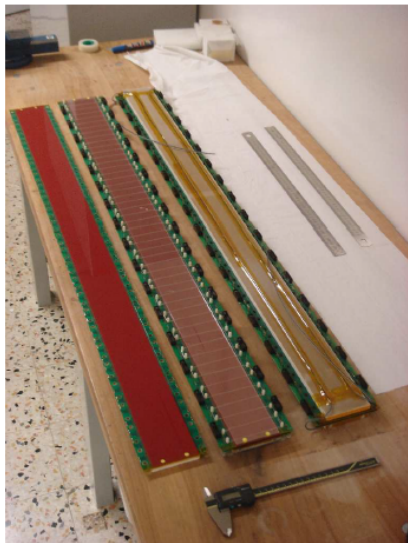


**Figure 3.5** A TOF MRPC before (left) and after construction (right).

The strips are filled with a non-flammable gas mixture made of 93% freon ( $\text{C}_2\text{H}_2\text{F}_4$ ) and 7 %  $\text{SF}_6$ , that allow respectively to

- reach a high ionisation density,
- quench the photons from recombination of the primary ion pairs,
- absorb the electrons that are emitted by the cathod and prevent the production of secondary avalanches.

Despite the fact that the total gas volume is quite reasonable, 16  $\text{m}^3$ , the costs of the gas mixture have lead to design a close circuit for gas circulation in the modules, the flux being approximately 2.7  $\text{m}^3/\text{h}$  and new gas being injected every few days. The MRPCs performance was tested with test beam at CERN with the final readout chain [84, 85] for a sample of mass-production strips. The measured efficiency and intrinsic time resolution are reported as function of the HV applied to the electrodes in fig. 3.6. With a HV of 13.0 kV, the TOF MRPCs have an intrinsic time resolution lower than 50 ps, (including the contribution of the readout electronics, estimated to be nearly 30 ps) and efficiency close to 100%. The operating voltage has been chosen to be this value, that is 13 kV. With the applied configuration, the growth of the avalanches in the gas volume is dominated by space-charge effects and the

MRPC can operate in saturated avalanche mode. The average charge produced by a through-going particle is small, at the level of 2–3 pC. As a consequence, the MRPCs are well suited to work at high rate. The high electric field, and the derived high drift velocity, allows to reach very good time resolution.

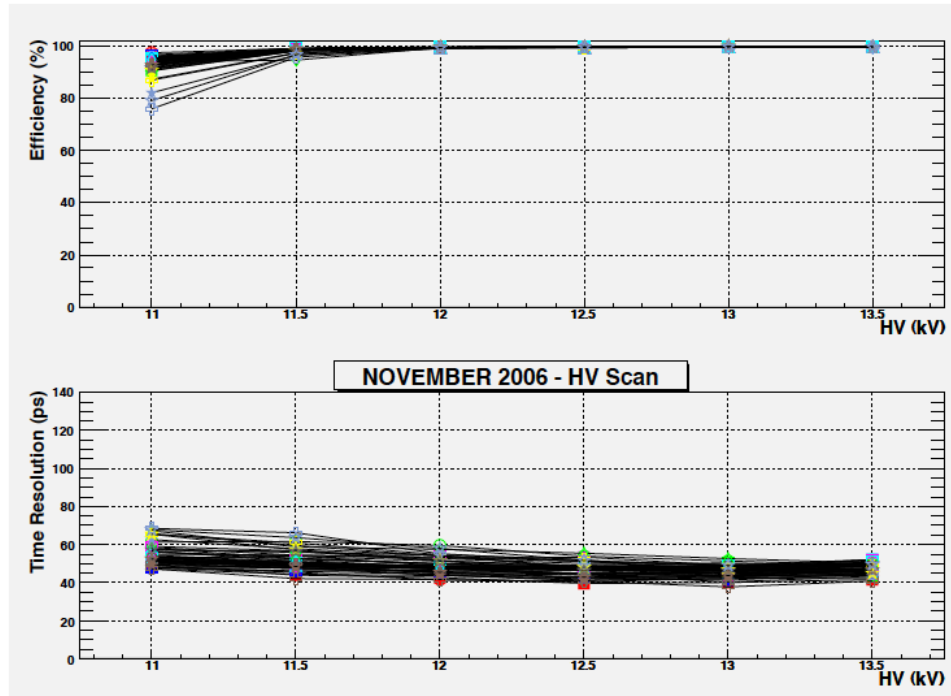


**Figure 3.6** Efficiency and time resolution as a function of high voltage for a sample of mass-production MRPC strips. These data, referring to test beam, have been collected by using a standard gas mixture of C<sub>2</sub>H<sub>2</sub>F<sub>4</sub> (90%), C<sub>4</sub>H<sub>10</sub> (5%) and SF<sub>6</sub> (5%). With this mixture a HV of 12.5kV could be chosen as nominal value. However, the curves shift of about 500 V on the right if an isobutane-free mixture is used. The choice of removing the flammable isobutane component from the mixture when in ALICE, lead to the setting of the nominal value to 13.0 kV.

Nonetheless fig. 3.6 shows a very good uniformity of the strips behaviour, common to several test samples. Finally the response of the detector to high rate and high radiation dose was tested at the Gamma Irradiation Facility (GIF) at CERN. Measurements have shown no degradation of the results up to about 1 kHz/cm<sup>2</sup> and for a radiation dose greater than 3.5 times the dose foreseen in the first 10 years of the LHC operation.

### 3.1.2 The Front-End Electronics

A schema of the front-end and readout electronics of the TOF is reported in fig. 3.7.

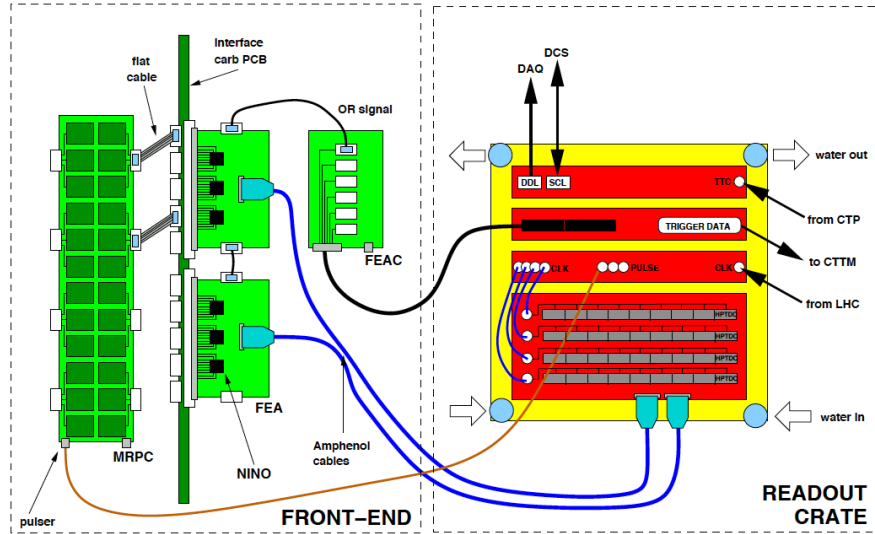


**Figure 3.7** Schema of the TOF front end and readout electronics.

The Front-End Analogue (FEA) cards placed inside the modules (see figure 3.2) are in charge of reading the differential signal coming from the MRPCs. The FEA contains three NINO ASIC chips (see fig. 3.8), that are 8-channel amplifier/discriminator devices with an output width correlated to the charge of the input signal. This width is called Time over Threshold (ToT), because it refers to the charge released during the interval in which the signal is above the threshold. The minimum value of the ToT is 6 ns. The charge information is important to apply the correction for time slewing<sup>2</sup>. Each FEA reads 24 pads displaced in two rows, corresponding to 8 channels  $\times$  3 NINO chips, so that one strip is read by four FEAs. The discriminated signal is sent to the readout component of the system, the TDC Readout Module (TRM) for the time measurement.

Moreover, the OR of two neighbouring FEAs is sent to the FEAC board (still placed inside the SMs). The FEAC supplies a group of 10 or 12 FEAs with the low voltage (2.5V) power, monitors their temperature through a set of sensors, sets the threshold voltages on the discriminator and, as already mentioned, collects the OR signals thanks to a Fully Programmable Gate Array (FPGA). The FEAC output is sent to the Local Trigger Module (LTM). According to this configuration, a “trigger hit” is defined if at least one hit has been recorded by any of the 96 pads of 2 half-strips. The group of half-strips connected to a FEAC is also referred to as “maxi-pad”. The purpose of these signals is twofold: they can be used to send a fast pre-trigger

<sup>2</sup>When two analogue signals that have different amplitudes but arrive at the same time are digitalised, the output values are different, because their leading edge reaches the TDC threshold at different times. The time-of-flight measurement is affected by this as it is obtained on the leading edge of the TDC signal.

to the Transition Radiation Detector and to contribute with a Level 0 (L0) trigger to the physics event selection. The TOF trigger has been widely used to trigger on cosmic muons both for central detectors calibration and for cosmic-ray physics [?, ?], but it also contributed to the selection of minimum bias events in pp collisions. During Pb–Pb data taking in 2010 and 2011, the TOF topological trigger has also played a fundamental role in the trigger for Ultra Peripheral Collisions (UPC) [?]. A large electronics board, the CTTM (Cosmic and Topology Trigger Module), located under the muon spectrometer platform, receives the LTM signals, asserts the L0 and L1 triggers and sends them to the Central Trigger Processor (CTP).

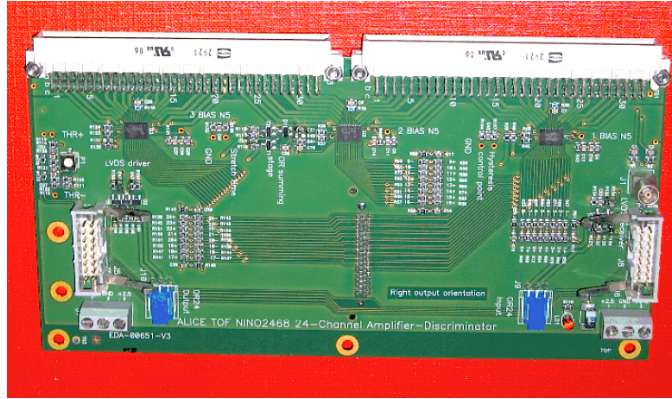


**Figure 3.8** One of the TOF Front End Analogue cards. The three NINO ASIC chips are visible on the top of the picture. The board dimensions are  $(19.0 \times 10.5)$  cm $^2$ .

### 3.1.3 The readout electronics

The discriminated signals are transferred from the front-end electronics to a custom VME crate where the differential signal is digitized into the time data, as anticipated in the previous section. Each side of a supermodule hosts two crates, as shown in fig. 3.1, that contain four types of VME64 modules: the TDC Readout Module (TRM), the Local Trigger Module (LTM), the Clock and Pulser Distribution Module (CPDM) and the Data Readout Module (DRM).

#### The TRM

The TRM manages the TDC readout operations. The left<sup>3</sup> crates house 10 TRMs (slots numbered from 3 to 12), the right crates only 9 (slots from 4 to 12). Each TRM hosts 10 mezzanine cards (piggybacks) with 3 High Performance Time To Digital Converter (HPTDC) chips that can read 8 channels, summing up to 30 HPTDCs that read 240 channels per board. The HPTDC determines the difference between the signal from the FEA and the trigger input, by relating it to a synchronous

<sup>3</sup>Left and right are determined by facing the SM from the ALICE A side.

counter latched to the LHC clock. Only the hits that fall in a valid matching window (MW), starting  $t_{latency}$  before the trigger arrival are transferred in the L1 FIFO of the HPTDC. Both  $t_{latency}$  and the matching window are programmable. During the first three years of the LHC operations, these parameters have been set to MW = 600 ns and  $t_{latency} = 9 \mu\text{s}$ , to be compared to the ALICE L1 trigger latency of  $6.7\mu\text{s}$ . In addition, the TRM deals with:

- HPTDC configuration,
- HPTDC hits reading,
- transfer of the data in temporary buffers embedded in an external RAM memory bank,
- data forwarding to the VME master module in a properly formatted form,
- nonlinearity correction: the TRM board also features an Integral NonLinearity look-up table, that is a correction code needed in the very high resolution mode of the HPTDCs.

### The LTM

The Local Trigger Module is the first level of the TOF trigger, in charge of receiving the FEAC output and transferring it to the CTTM. It is also in charge of setting and monitoring low voltages and temperatures in the FEE section of the SM. Finally, each LTM sets the thresholds for the NINO discriminator on the FEAs and defines a delay to the trigger signals that compensates for the different cable length whenever needed. Only one LTM module per crate is present and housed in the VME crate slot 2.

### The CPDM

The Clock and Pulser Distribution Module receives the LHC clock via an optical fiber and sends the clock as a standard LVDS input to each VME module in a crate pair. The clock received by the CPDM is a dedicated clock parallel to the TTC system in order to reduce the jitter associated with it. In absence of an external clock, the CPDM delivers a clock locked to an internal oscillator. The CPDM also provides 17 LEMO outputs that are connected to the pulse lines of the MRPC strips, for monitoring the readout chain and calibration purposes. For each crate pair, the CPDM occupies the slot 3 in the right crate.

### The DRM

The Data Readout Module installed in the Master VME slot of each crate is the interface between the TOF readout system and the ALICE DAQ and the main responsible for the crate readout. It has several important functions:

- it interfaces to the central ALICE DAQ system via the Detector Data Link (DDL). The TOF is equipped in total with 18 supermodules, read by 4 crates each, for a total of 72 crates, one per DDL. At present, six DDLs are linked to one LDC so that the output rate is not bigger than 5.7 KHz.
- It receives and decodes trigger signals and messages from the TTC system, it propagates to all the VME modules the bunch counter reset, L1 and L2 trigger signals. Part of the trigger information is stored in the data to be sent over the Detector Data Link (DDL) for consistency checks.
- It reads out the data in the LTM and TRMs of the crate and when a Level 2 (L2) trigger is issued it encodes the data stored in its buffer according to the common ALICE format.
- It hosts a single board computer from where it is possible to reprogram the firmware for each of the FPGAs present on the crate.
- It monitors the condition of the readout and sets a busy <sup>4</sup> signal to the Auxiliary Control Module (ACM).
- It receives from the ACM an external pulse signal, for the detector calibration.

Finally, the DRM card is equipped with an additional optical link to a commercial PC which provides extra Slow Control functionalities. The 72 TOF crates are connected to 18 commercial PCs, grouped in such a way that one PC controls one entire SM.

### 3.2 TOF data quality monitoring online

During data taking, the TOF data are monitored online by the DQM operator who is mainly responsible for checking the shape of the signal, the detector and electronics configuration and the hit occupancy. The software tools to accomplish this task have been developed by the Ph.D. candidate.

The general DQM framework has been described in section 2.3.2: AMORE provides the infrastructure to access and analyse the data online while being collected and the graphical tools to display or archive the results. The interplay between the AliRoot QA and the AMORE frameworks has been exploited for the implementation of the TOF monitoring. Two AliRoot classes have been implemented in the QA framework: AliTOFQADataMakerRec and AliTOFQAChecker, that for simplicity will be referred to as the data maker and the checker, respectively. The main advantage of having the data maker as part of the ALICE analysis package is that

---

<sup>4</sup>The busy signal inhibits further triggers from being generated by the central trigger processor during readout.

raw data<sup>5</sup> can be analysed both online and offline, through some interface that invokes the QA framework, being either a custom macro or the detector AMORE agent. Besides, the raw data structure and decoding programs are implemented in AliRoot. The results obtained online are reproducible *a posteriori*, this representing a fundamental resource for the detector experts that may need to investigate the issues spotted online by the DQM operator. Furthermore, the QA framework supports the definition of event species, gives the possibility of cloning the monitoring objects for different trigger classes and of defining thresholds for the checker, whose numerical value are saved for further reference in the OCDB.

### 3.2.1 The TOF signal

The TOF signal is provided by the HPTDC and encoded by the TRMs in the raw data format. The time measured by the TDC is not the time-of-flight of the particle generating the hit, as the interaction time information is not available at that stage. When a HPTDC receives a level 1 (L1) trigger, it searches for hits falling in the

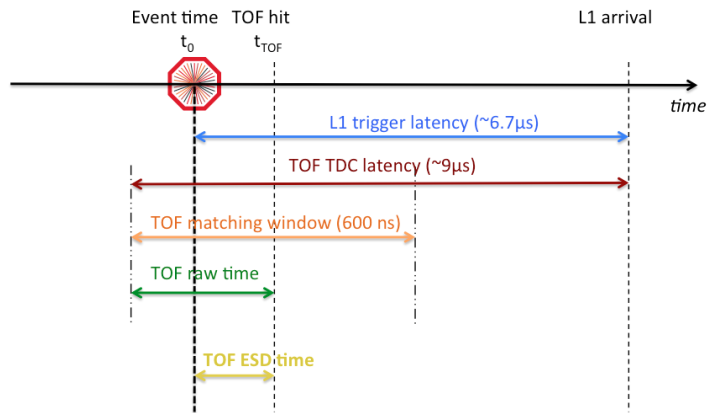


**Figure 3.9** Simplified schema illustrating how the TOF time signal is measured in relation to the L1 trigger arrival after the collision event.

TOF time Matching Window (MW), starting from an amount of time equal to the TOF latency window back in time with respect to the L1 (see fig. 3.9). The raw time is measured in TDC bins unit ( $N_{tdc}$ ), from the beginning of the MW. To obtain the time in ps,  $N_{tdc}$  has to be multiplied by the time resolution of the TDC, that is 24.4 ps. During the reconstruction phase the physical arrival time of the particle is associated to each TOF cluster by correcting the raw signal for several contributions:

<sup>5</sup>The data maker implements methods to inspect data in several formats, as raws, rec points, digits and ESDs (see section ??). As a consequence, the same physical observables could be monitored during the different steps of the reconstruction process. Because the users do not have access to the intermediate stages output of the reconstruction on the Grid, the software has been mainly developed for the raw data analysis, adapting it to the requirements of the DQM online.

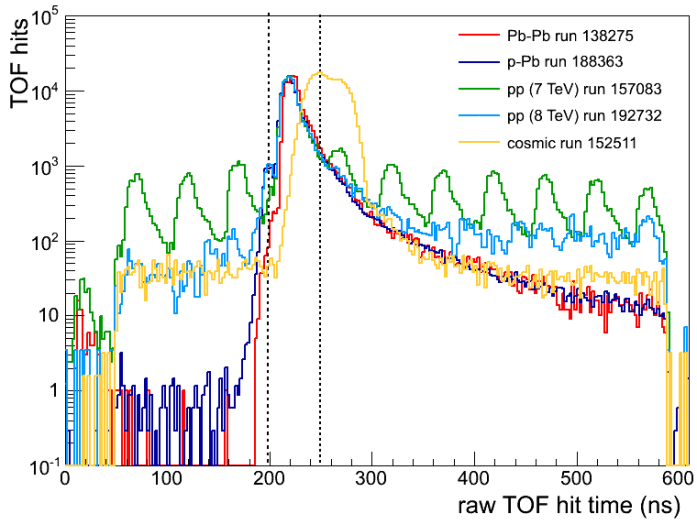


**Figure 3.10** TOF raw time signal in cosmic data taking (orange), pp at  $\sqrt{s} = 7$  TeV (green), pp at  $\sqrt{s} = 8$  TeV (cyan), p–Pb (blue) and Pb–Pb (red) collisions. The pp at  $\sqrt{s} = 7$  TeV distribution is related to a fill where the spacing between consecutive bunches is a train was of 50 ns: the secondary peaks are populated by hits from collisions happening in the bunch crossing (BC) before and after the triggered collision (pile-up from different BC).

L0-L1 trigger latency, TOF TDC latency window, the relative difference between the TRM synchronization latched to the LHC clock measured in number of bunch crossing ( $\Delta BC$ ), the calibration constants and finally the average interaction time of the fill (called  $t_0,fill$ ). The event time can be subtracted event by event during the analysis to improve the overall time resolution.

The TOF raw time signal is monitored online by the DQM operator in the full TOF matching window of 600 ns. Fig. 3.10 compares the raw signal distributions obtained by the QA data maker for cosmics, pp, p–Pb and Pb–Pb data taking. In the first case, the time distribution is clearly different from that of collision events: it exhibits a double peak structure, as the cosmic muons do not come from the interaction point but cross the TOF from above or below, leaving two consecutive hits in the detector. In collision events, the raw time distribution is peaked between 200 and 250 ns and exhibits a tail about 3 BC long, due to slower particles with later arrival time. In fig. 3.10 the two pp distributions refer to runs with different LHC filling scheme. Because the TOF matching window is 600 ns wide, if the bunch spacing is small enough (there 50 ns) not only the hits coming from the triggered bunch crossings (BC) are recorded, but also the following. This is reflected in the multiple peak structure shown in fig. 3.10. The hits populating the secondary peaks will be discarded during reconstruction, because recognized as pile-up from different BC.

A TOF hit is fully defined by a time and a Time over Threshold (ToT) measure-

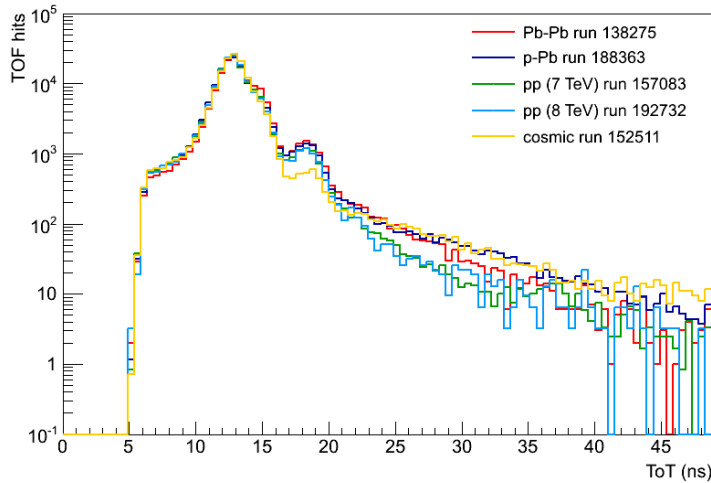


**Figure 3.11** Time over Threshold (ToT) distributions from cosmic data taking (orange), pp at  $\sqrt{s} = 7$  TeV (green), pp at  $\sqrt{s} = 8$  TeV (cyan), p–Pb (blue) and Pb–Pb (red) collisions. The green line, in particular, is related to a run with 50 ns spacing between the bunches of the same train.

ment (see section 3.1.2). Because the ToT is measured between the signal leading and trailing edges, if no trailing edge is seen by the TDC, no ToT measurement is possible. These hits are called “orphans”. The fraction of orphan physical hits is <1%. The ToT is also monitored online, as it can be seen in fig. 3.11. The shape of the distribution is a gaussian, centered around 10 ns. The minimum ToT is 6 ns, due to the characteristics of the NINO ASIC discriminator. There is no difference between the physical hits in different types of collisions. However, if noise is present, its randomness translates into a deformation of the ToT distribution. If a noise hit has a trailing edge, it is likely very close to the leading edge, resulting in a smaller ToT, closer or in most cases smaller than 6 ns. In the latter case, most of the noise hits are recorded as orphans. Viceversa, an anomalous increase in the number of orphan hits suggests the presence of noisy channels or issues with the readout configuration.

### 3.2.2 Monitoring the TOF readout status

The status of the readout electronics is monitored in terms of efficiency, time synchronisation and hardware status, down to the single-channel level (TDC input). The readout efficiency is one of the necessary ingredients for the reproducibility of the detector response in Monte Carlo simulation. Moreover, during reconstruction it is important to remove noise and take into account possible encoding/decoding issues at the TRM level. This is achieved by masking the channels that are flagged as “bad” from the hardware point of view, “noisy” or “inefficient”: if a hit possibly associated to a track propagated to TOF comes from such bad channels, it is dis-

carded. Most important is therefore to verify the correspondence between the map of the recorded hits from the raw data and some reference map, to spot runtime readout or decoding issues that cannot be detected by the Detector Control System.

In fig. 3.12 examples of the enabled and noisy channels maps are reported. The numbering on the horizontal axis is referred to the supermodule index, while on the vertical axis is the strip index along a supermodule. Each bin of the histograms collects 24 channels read by a FEA as described in section 3.1.2. Empty bins in the enabled channels maps are due to issues of different nature. The exclusion of some equipment from data taking has consequences on the effective detector acceptance, especially when a whole crate (1/72 of the entire detector) is off or unavailable, due to power supply problems or the necessity of excluding the associated DDL from the DAQ configuration. A given group of channels may not be receiving data because the corresponding strips or front-end cards are not powered because of issues with the high voltage (HV) or low voltage (LV) power supplies, respectively. The former causes the “holes” marked with a blue rectangle in fig. 3.12, whereas the latter is responsible for the empty bins enlightened in magenta. The remaining white rectangles of fig. 3.12 correspond to disabled TRMs.

The TOF Detector Control System sends via DIM to the TOF Detector Algorithm (DA) the information about the hardware status of the TOF HV, FEE and readout equipment. The DA is in charge of producing the maps of the readout configuration, saving the status of each channel in a OCDB object format that the TOF Pre-Processor [66], a SHUTTLE routine, transfers to the Grid OCDB. This is done at least twice per run, at Start Of Run (SOR) and End Of Run (EOR). If any difference is detected, multiple versions of the OCDB object would be present for that run. The most recent version is retrieved from AliEn during reconstruction of real and simulated data. The hit map relative to the same run is reported in fig. 3.13, as obtained with the QA data maker. The data maker retrieves a valid channel map from the OCDB and while decoding the raw data, masks the channels that have been flagged as bad, noisy or inefficient. When running the QA within the online DQM framework for run number  $N$ , the OCDB entry relative to  $N$  is not yet available, so the reference from the last available run, typically  $N-1$ , is used. If the monitoring is run offline, the OCDB map created at EOR is loaded.

The example map reported in fig. 3.13 exhibits a few differences with respect to the enabled channels map in supermodules 10 and 14. These are understood as readout inefficiencies and included in the reference map reported in fig. 3.14. The latter is the one to be used during reconstruction of raw data to discard hits coming from bad channels. During the simulation of Pb–Pb collisions anchored<sup>6</sup> runs, the reference map is used to take into account properly the TOF readout efficiency. Any discrepancy between the hit map and the reference suggests a possible unde-

---

<sup>6</sup>The Monte Carlo event samples to be analysed for the efficiency studies are simulated by reproducing the same running conditions (and most often statistics), as the real data taking: beam properties, trigger, detector readout configuration and calibration, among others. The simulated runs are commonly called “anchored” runs.

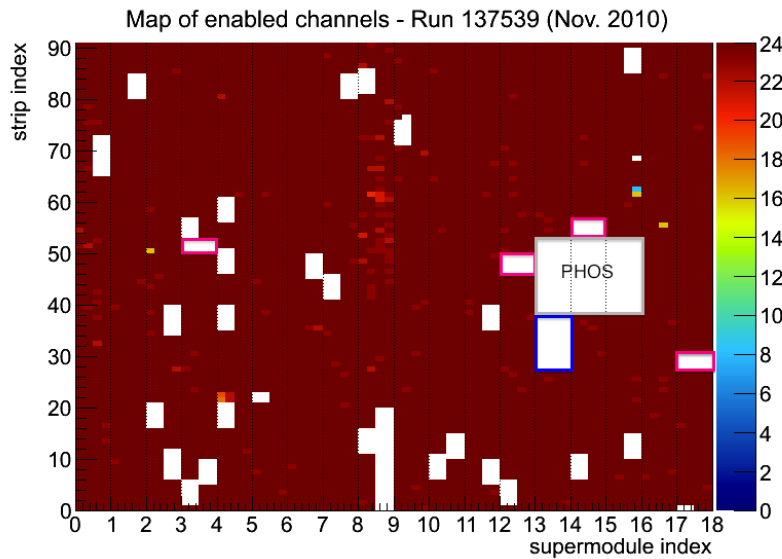


**Figure 3.12** Map of the enabled TOF readout channels in the Pb–Pb physics run 137539 taken on the 14 November 2010. Each bin represents the 24 channels read by a FEA, as described in section 3.1.2. Considering the detector orientation, going from left to right on the x-axis means moving anti-clockwise from 0 to  $2\pi$  rad in azimuthal angle while facing the TOF from the so-called A-side, opposite to the muon spectrometer (that is on the ALICE C-side). The SMs are parallel to the beam axis, so that the first strip is about 3.5 m from the IP on the A side and the last one is placed symmetrically on the C side. In the map, the white rectangles correspond to disabled TRMs; the blue rectangle indicates that a group of strips not powered due to HV problems and the magenta rectangles group disabled FEA with LV problems. Other holes are disabled HPTDC or single problematic channels. The grey rectangle replaces the central modules of sectors 13, 14, 15 that were never installed due to the presence of PHOS. The enabled channels to be masked during reconstruction because inefficient are not yet removed from this map.

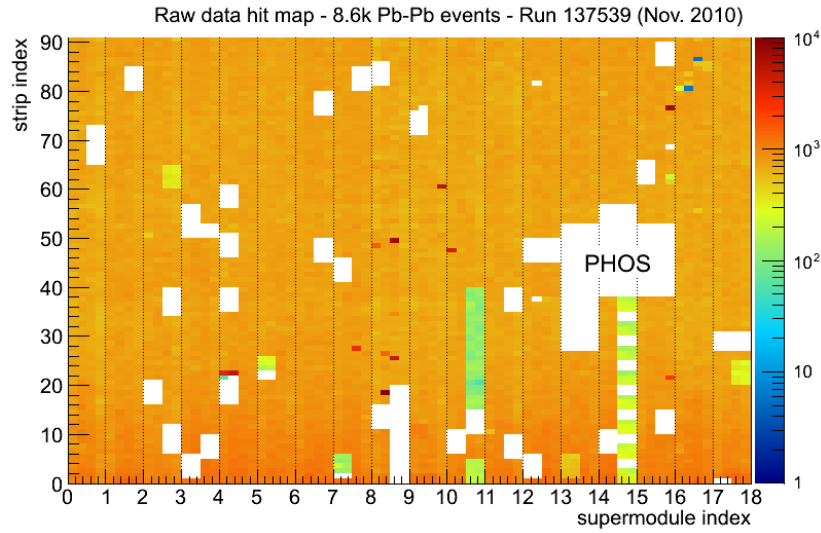


**Figure 3.13** Hit map relative to a subsample of  $8.6 \times 10^3$  events from the Pb–Pb physics run 137539 taken on the 14 November 2010. Each bin groups hits from the 24 channels read by a FEA.

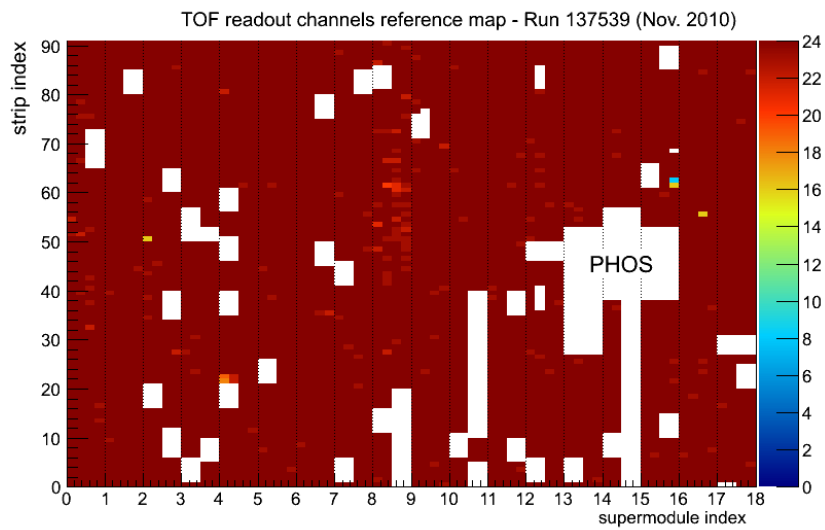


**Figure 3.14** Reference TOF readout channels map for the Pb–Pb physics run 137539. The map shows only the channels that are enabled, efficient and not noisy.

tected change in the readout or DAQ configuration (if run online) or a problem in the propagation of the channel status information to the OCDB. In both cases, it triggers some action by the detector experts.

The TOF DQM tools monitor the relative time alignment of the readout equipment, as in fig. 3.15, where the raw hit time per TRM is reported. The peak of the time distribution falls between 200 and 250 ns. Within each crate, the plots show a time delay, that is increasing with the TRM index, due to the length of the cables that bring the signal from the FEE to the readout boards. A few TRMs have been found to be de-synchronized with respect to the others by a BC but this shift is re-absorbed during the calibration phase.

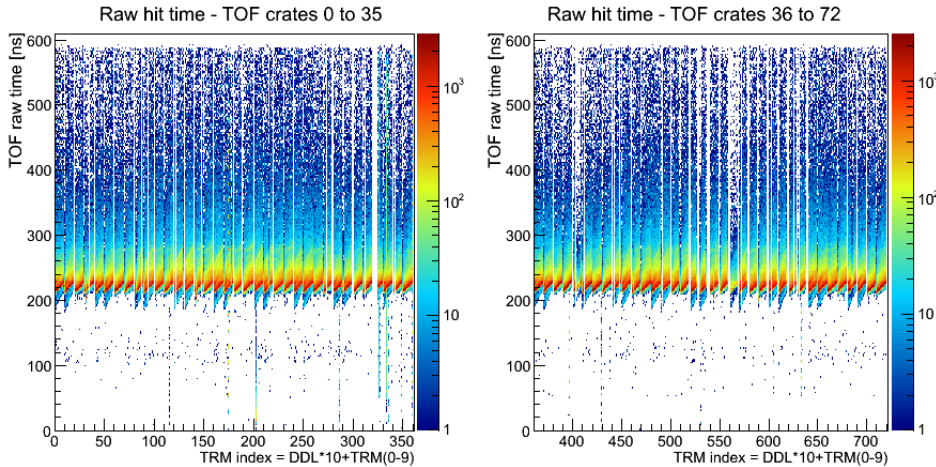


**Figure 3.15** TOF raw time signal as function of the TRM index for the crates from 0 to 35 (left) and 36 to 71 (right).

### 3.2.3 Electronics noise monitoring

The noisy channels are flagged during dedicated “noise scan” runs that are performed during the beam energy ramp-up phase of each LHC fill<sup>7</sup>, when the TOF strips are supplied with 0.5 kV power, much lower than the nominal HV of 13.5kV. A 1 kHz trigger signal is issued by the TOF LTU to all the readout elements. The hits recorded by the readout are noise from the electronics. The TOF Detector Algorithm (DA) processes the data in search for noisy channels and flags them for the OCDB reference object, from which the map in fig. 3.16 is obtained. When a channel is found to be pathologically noisy, that is if it is flagged as noisy in more than 50% of the noise scans during a given period (from two to four weeks, depending on the data taking activity) it is disabled from the acquisition. The fraction

<sup>7</sup>A fill starts when protons or ions are injected in the LHC. The beam lifetime is related to the bunch intensity, luminosity and beam conditions, but normally is between 6 and 12 hours.

of disabled TOF noisy channels, of the order of  $\sim 8 \times 10^{-4}$ , has been stable during the first three years of ALICE operations.

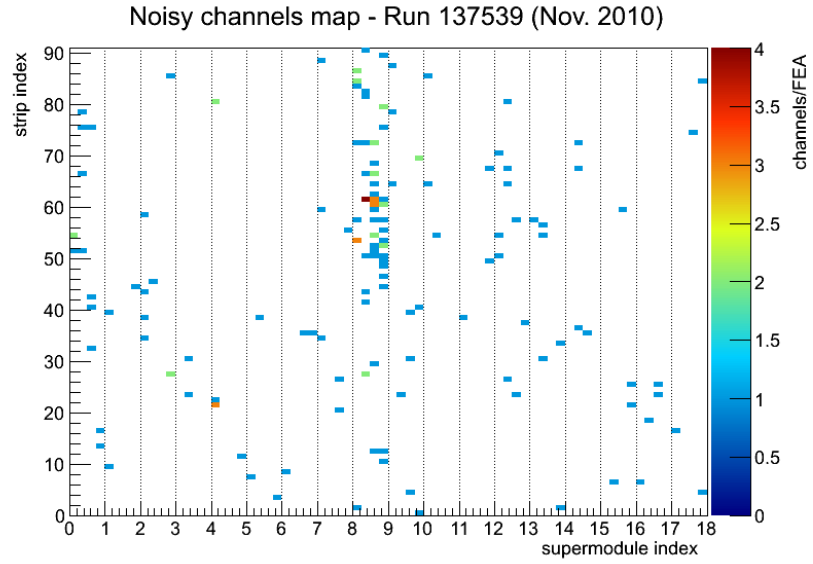


**Figure 3.16** Example of the map of noisy TOF channels relative to Pb–Pb physics run 137539.

## Chapter 4

# TOF data quality assurance, performance and PID

The main goal of the Time-Of-Flight particle identification (PID) is to extend the ALICE  $\pi$ /K and K/p discrimination power to higher  $p_t$  with respect to the TPC. The time-of-flight technique and the requirement to obtain such a separation, only briefly summarised in the previous chapter, are treated now more extensively. The following ingredients are of fundamental importance for the TOF performance:

- the TPC-TOF matching efficiency,
- optimal calibration of the TOF signal,
- knowledge of the interaction time ( $t_0$ ) per event with the best possible resolution.

The matching efficiency reflects the probability that a track is associated to a hit on the TOF sensitive area, therefore it represents the first requirement to attempt identification via time-of-flight. A good calibration of the TPC *per se* is important to have the best possible resolution on the momentum  $p$  and the track length,  $L$ . The time calibration and the  $t_0$  information are needed to achieve the best possible overall resolution on the time-of-flight measurements.

One of the possible PID strategies that exploit TOF is based on the discriminating variable  $N_{\sigma,i}^{TOF}$  defined as

$$N_{\sigma,i}^{TOF} = \frac{t - t_0 - t_{exp,i}}{\sigma_{PID,TOF}} \quad (4.1)$$

where  $i$  indicates the particle species ( $i = \pi, K, p, \dots$ ),  $t$  is the measured TOF hit time,  $t_0$  is the interaction time,  $t_{exp,i}$  is the expected time of flight computed during the central tracking procedure (also called “integrated time”). The total resolution,  $\sigma_{PID,TOF}$ , is the sum of the following contributions:

$$\sigma_{PID,TOF} = \sqrt{\sigma_{TOF}^2 + \sigma_{timeZero}^2 + \sigma_{trk}^2} \quad (4.2)$$

The expected times depend on the mass hypothesis, but also on the measurement of the particle momentum and the track length during the tracking procedure. These globally contribute with  $\sigma_{trk}$ . The resolution of the interaction time,  $\sigma_{timeZero}$ , depends on how the  $t_0$  is measured in ALICE, among three possible ways: as the average event time of the fill, with the T0 detector or with an algorithm involving tracks with hits on TOF (details are given in section 4.3). In eq. 4.1 this contribution has been distinguished from  $\sigma_{TOF}$  (while it was included in eq. 3.4) because if the first two strategies are used, the resolution is independent of the TOF performance. Finally,  $\sigma_{TOF}$  is the resolution on the time measurement, for which the TOF design has been optimized in order to get  $\sigma_{TOF} \lesssim 100$  ps. This contribution is neither event nor track dependent but strictly related to the TOF detector, so that it can be refined with a proper calibration.

The ALICE calibration scheme consists of a multiple steps procedure: each phase (or “pass”) implies a partial reconstruction of the data that is the input for the calibration tasks and is followed by very basic routines for Quality Assurance (QA) controls. Each detector verifies the success of its calibration procedure through the QA analysis and TOF among the others. The TOF QA task is meant to provide already at the first reconstruction pass a realistic picture of the detector performance and a preliminary estimate of the main quantities that are relevant for particle identification with TOF. After a brief introduction on the calibration strategy, the settings and cuts applied in the TOF QA analysis are briefly listed in section 4.1. In the following sections, the TOF detector performance and PID are discussed by means of the QA histograms for pp and Pb–Pb collisions in terms of matching efficiency (section 4.2) and PID (section 5.1.3). The attention is drawn in particular to the detector behaviour during the 2010 Pb–Pb data taking, whose sample has been analysed to study the  $K^{*0}$  production presented in chapter 5.

## 4.1 Strategy for calibration and QA

The ALICE calibration scheme is a multiple-step procedure, as mentioned before. A partial reconstruction of a sub-sample of high-multiplicity minimum bias events devoted to calibration, is carried out during the cpass0, the name standing for “calibration pass 0”. The output ESDs are the input for the calibration routines, that determine the calibration parameters to be stored in the OCDB. If present, the pre-existing objects<sup>1</sup> are updated, otherwise new ones are created for the actual run. A first measurement of the  $t_{0,fill}$  is derived by TOF at cpass0 by fitting the  $(t-t_{exp})$  distribution of the tracks. Any further refinement of this estimate needs a more precise knowledge of the track parameters, therefore it relies on the TPC calibration that can be available only at cpass1. At cpass1, the same subsample of data is reconstructed by using the updated version of the OCDB containing the new parameters. The calibration procedure is run in parallel to the QA checks on the cpass1 ESDs.

---

<sup>1</sup>For some of the parameters, such as the vertex position, a version of the OCDB object was created online by the DA and migrated to the Grid by the SHUTTLE.

The TOF QA task at cpass1 looks at the time alignment before the full calibration and at the matching efficiency after the TPC cpass0 calibration. The output of cpass1 calibration triggers a second update of the OCDB. In case of failure of the automatic calibration procedure or in case of available improvements of the calibration parameters, the OCDB can be updated manually before the reconstruction and QA chain run once more during the so-called “validation pass” (vpass). The full reconstruction starts only when the calibration is satisfactory for all the participating detectors.

### TOF time calibration

The difference between the measured TOF time and the expected time calculated during reconstruction for a given particle species, defines the PID variable according to eq. 4.1. If TOF was an ideal detector<sup>2</sup>, the  $(t - t_{exp})$  should be centered at zero. The time associated to a TOF hit is obtained from the raw time as described in section 3.2.1, by subtracting the latency common to all channels. Besides, the signals coming from different channels are desynchronized for several reasons as explained below. Let  $t_{true}$  be the actual time signal, and  $t$  the hit time measured by TOF, then

$$t - t_{true} = t_{0,fill} + t_{calib} + t_{slewing} + t_{extra}. \quad (4.3)$$

The first contribution is common to all channels and comes from  $t_{0,fill}$ , which is isolated during cpass0 by extracting the gaussian mean of the  $(t - t_{exp,\pi})$  distribution (see section 4.3). Because the  $t_{exp}$  depends on a mass hypothesis and given the fact that pions are mostly produced in the collisions, the pion mass is used (and  $t_{exp,\pi}$ ). Other sources of delay ( $t_{calib}$ ) between different channels are the different length of the cables connecting the front-end and the readout cards, or due to the clock signal propagation to the crates (Bunch Crossing – BC correction). It was shown in fig. 3.15 that the raw time signal of channels belonging to adjacent TRMs is shifted. The cable lengths were measured in laboratory before the TOF assembly, while the BC correction was determined during the commissioning phase.  $t_{calib}$  is then known and can be subtracted from the time measurement of each channel. The time-slewing channel-dependent effect ( $t_{slewing}$ ) has been studied during the detector commissioning and it has been determined by fitting the distribution of TOF time as function of the ToT with a 5th order polynomial. Any residual contribution ( $t_{extra}$ ) to the uncalibrated signal can be determined considering that after the calibration

$$t_{true} - t_{exp} = t - t_{0,fill} - t_{calib} - t_{slewing} - t_{extra} \quad (4.4)$$

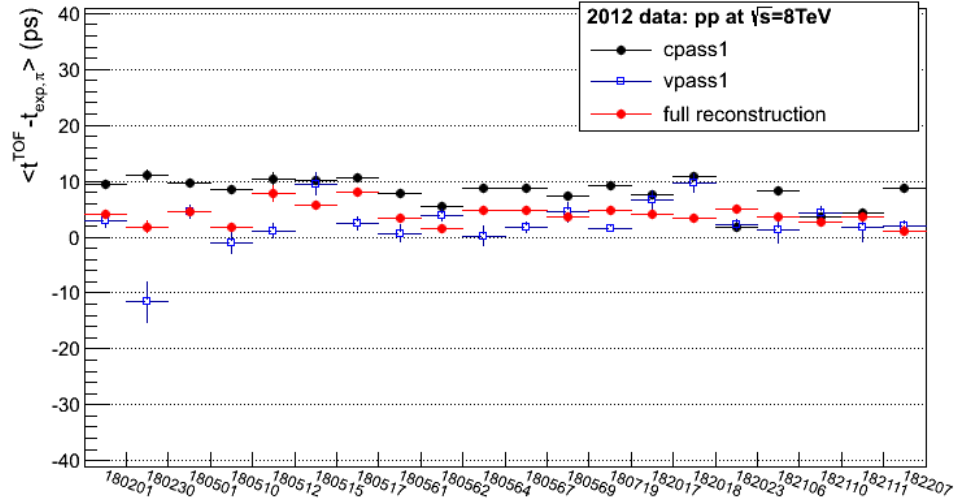
should be centered around 0. A channel-by-channel gaussian fit of the  $(t - t_{exp})$  distribution gives  $t_{extra}$ .

Fig. 4.1 shows the TOF  $(t - t_{exp,\pi})$  alignment for a set of 2012 pp runs at  $\sqrt{s} = 8$  TeV,

---

<sup>2</sup>It is also assumed that the particle energy loss along the track is correctly taken into account by the tracking procedure when calculating the integrated times.

from cpass1 to the full reconstruction: as the calibration is refined, the time alignment gets more uniform, while the average difference stays close to 0. For quality assurance purposes, an offset of  $\pm 20$  ps is tolerated, but the distribution shown that the times are aligned well within  $\pm 10$  ps. During the analysis when possible, the  $t_{0,fill}$  is substituted with an event-by-event estimate of  $t_0$  by the T0 detector or the TOF algorithm, whose more precise measurement can further reduce this shift.



**Figure 4.1** Trending distribution showing the  $(t-t_{exp,\pi})$  alignment for 20 runs taken with pp collisions at  $\sqrt{s} = 8$  TeV in 2012, obtained by the QA analysis. The values at calibration pass 1 (black full circles), validation pass (empty blue squares) and after the full reconstruction (full red circles) are compared. Each value is obtained from a gaussian fit of the  $(t-t_{exp,\pi})$  distribution.

## 4.2 The TOF matching efficiency

The ALICE tracking algorithm has been described in section 2.4. After the propagation through TPC and TRD, the tracks are extrapolated to the TOF sensitive layer. A geometrical matching window of 3 cm (for Pb–Pb collisions) or 10 cm (for pp collisions) is opened around the intercept of the extrapolated track with the TOF sensitive layer. The algorithm looks for TOF clusters within this matching window and if any is found, the closest hit to the crossing point is associated to the track. The “matched” track is then propagated to the TOF layer. In Pb–Pb the geometrical matching window is also widened to the pp value to increase the TOF matching efficiency in (very low multiplicity) Ultra-Peripheral Collisions (UPC). The quality of the tracking is monitored by looking at the distance (or residual) in the pad reference frame between the extrapolated track-point at the TOF layer and the center of the pad containing the matched hit. The residual along the  $x$  direction,

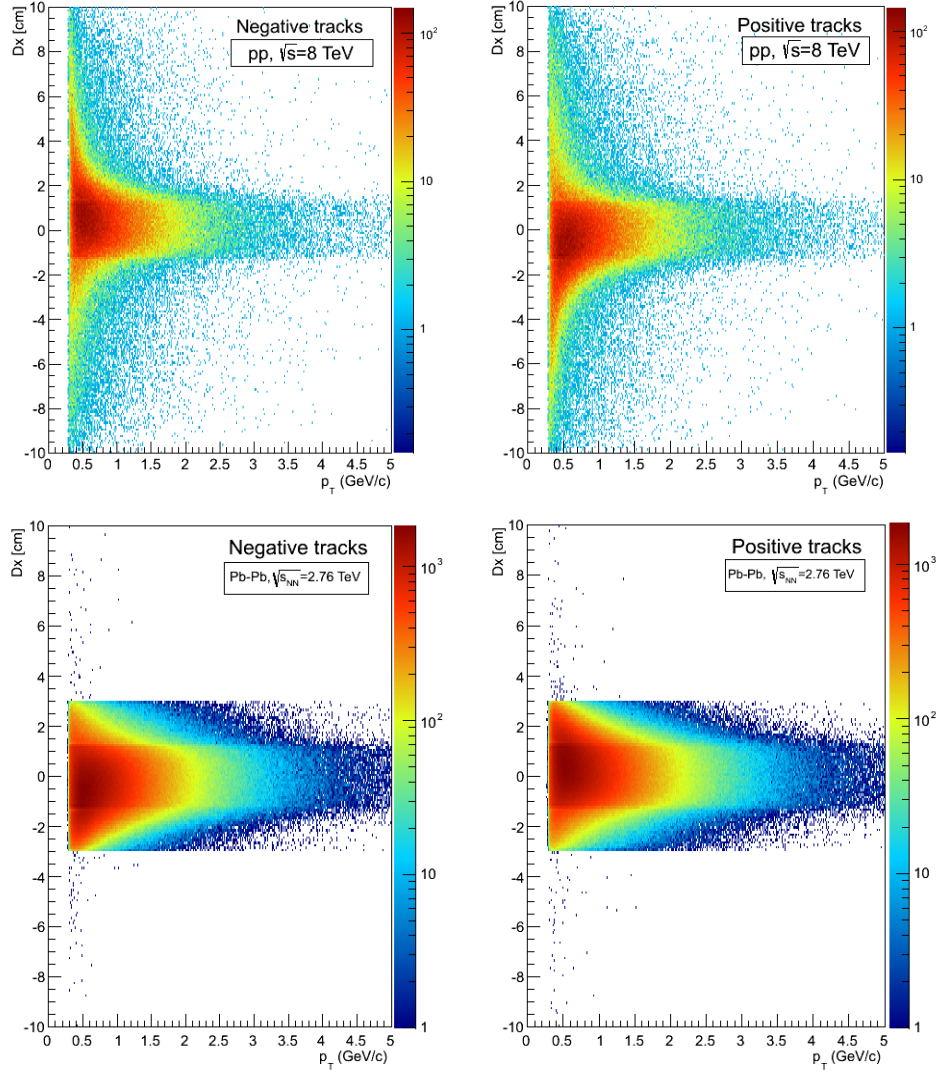


**Figure 4.2** TOF residuals along the  $x$  direction,  $Dx$ , as function of the reconstructed  $p_t$ , for negative (left) and positive (right) tracks with  $|\eta| \leq 0.8$ , in  $pp$  at  $\sqrt{s} = 8\text{ TeV}$  (top row) and  $Pb-Pb$  at  $\sqrt{s_{NN}} = 2.76\text{ TeV}$  (bottom row) collisions. The pad edges at  $Dx = \pm 1.25\text{ cm}$  can also be distinguished. In  $pp$  collisions the geometrical matching window is 10 cm, while for  $Pb-Pb$  collisions it is 3 cm. The latter shows also entries for  $Dz > 3\text{ cm}$  because the geometrical matching window is widened to the  $pp$  value to increase the TOF matching efficiency in (very low multiplicity) Ultra-Peripheral Collisions.

$D_x$ , depends on the transverse momentum of the track and is reported in fig. 4.2 for positive and negative tracks, in pp and Pb–Pb collisions. The distributions are centered at zero but also exhibit a small accumulation point positioned at the edge of the pad, that is symmetrical with respect to zero for positive and negative particles, because of the effect of the magnetic field on particles with opposite charge. In the Pb–Pb case most of the hits populate the  $|D_z| \pm 3$  cm range, reflecting the geometrical matching window used by the algorithm. The few exceptions are hits coming from UPC-triggered events. The residuals along the  $z$  direction,  $D_z$ , depend on

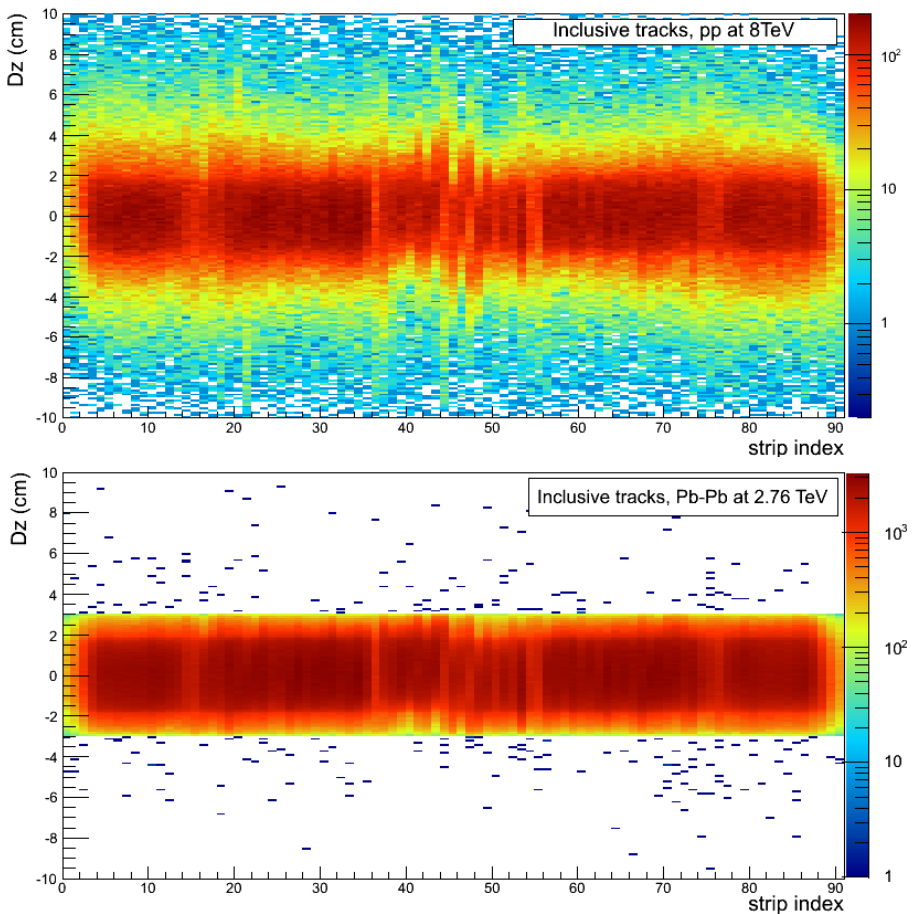


**Figure 4.3** TOF residuals along the  $z$  direction,  $D_z$ , as function of the strip index for all (inclusive) tracks with  $|\eta| \leq 0.8$ , in pp at  $\sqrt{s} = 8$  TeV (top) and Pb–Pb at  $\sqrt{s_{NN}} = 2.76$  TeV (bottom) collisions. The pad edges at  $D_z = \pm 1.75$  cm can also be distinguished as the borders of the dark red central band. In pp collisions the geometrical matching window is 10 cm, while for Pb–Pb collisions it is 3 cm. The bottom plots show also entries for  $D_z > 3$  cm because the geometrical matching window is widened to the pp value to increase the TOF matching efficiency in (very low multiplicity) Ultra-Peripheral Collisions.

the longitudinal component of the particle momentum and its reconstruction in the

tracker.  $Dz$  is reported in fig. 4.3 as function of the strip index<sup>3</sup>. Because the TPC is divided in two drift regions by the cathodic plane (placed at  $z=0$ ) with non-perfectly uniform electric field, the quality of the TPC calibration and measurement of the longitudinal momentum affects the residuals along the  $z$  direction. The  $Dz$  distribution is symmetrical with respect to the strip index 45, that is at  $z=0$ , and also the TOF modules structure is visible. Except the track multiplicity and the geometrical matching window, there is no difference between pp and Pb–Pb collisions.

The matching efficiency is defined as

$$\epsilon_{match} = \frac{\text{reconstructed tracks with a TOF hit}}{\text{reconstructed tracks}}. \quad (4.5)$$

Mismatched tracks are those matched with a wrong TOF hit. Clearly the interest is to have the TOF track matching efficiency as high as possible, while keeping the number of mismatched tracks as small as possible.

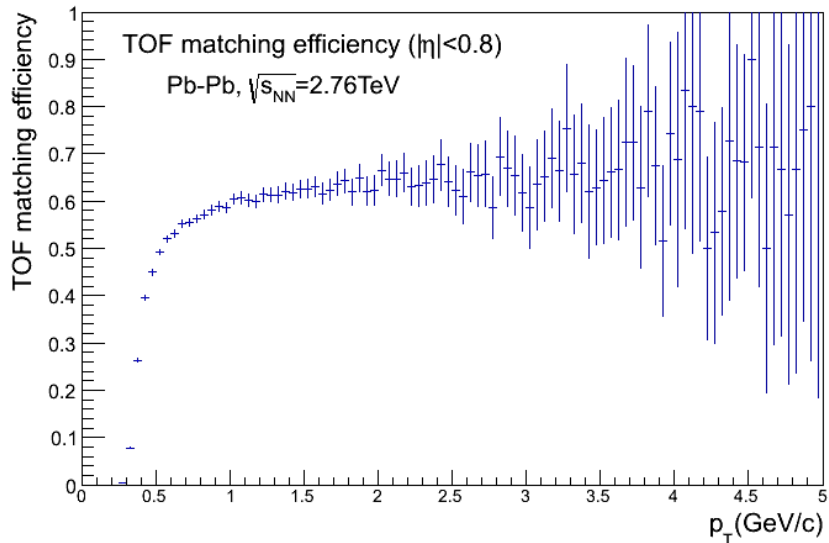


**Figure 4.4** TOF Matching efficiency as function of the reconstructed  $p_t$ , for tracks with  $|\eta| \leq 0.8$ . The sample refers to a 2010 Pb–Pb run.

The TOF matching efficiency as measured Pb–Pb collisions for  $|\eta| \leq 0.8$  is reported in figs. 4.4, 4.5, 4.6 as function of the particle transverse momentum, pseudorapidity and azimuthal angle measured at the primary vertex. Tracks with  $p_t < 0.3$  GeV/c do not reach the TOF due to the trajectory curvature in the magnetic field. For  $p_t > 0.3$  GeV/c  $\epsilon_{match}$  is rapidly increasing until it saturates for  $p_t > 1$  GeV/c. The matching efficiency depends on the detector readout efficiency: in figs. 4.5 and 4.6, where a cut on  $p_t \geq$  GeV/c has been applied, the variations with respect to the saturation value are due to the readout elements that are disabled or

<sup>3</sup>The strip index increases going from the A-side (positive  $z$ ) to the C-side (negative  $z$ ).

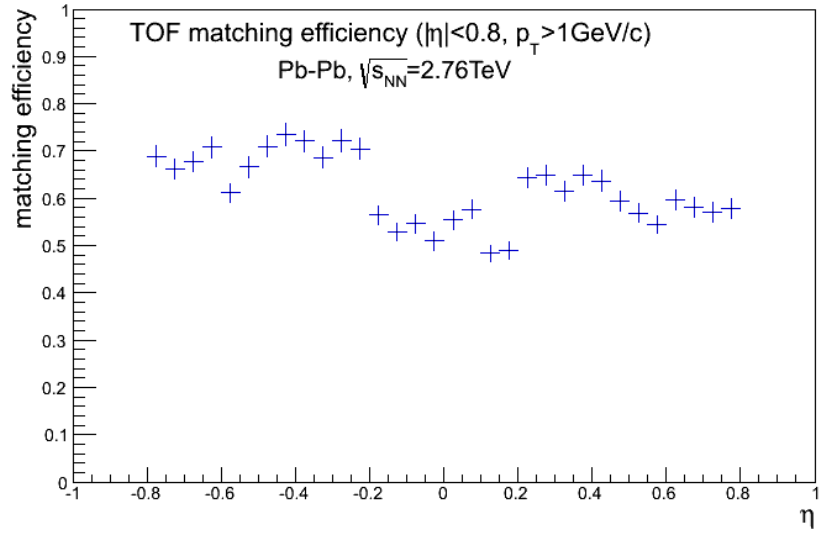


**Figure 4.5** TOF Matching efficiency as function of pseudorapidity ( $\eta$ ), for tracks with  $|\eta| \leq 0.8$  and  $p_t > 1\text{GeV}/c$ . The sample refers to a 2010 Pb–Pb run.

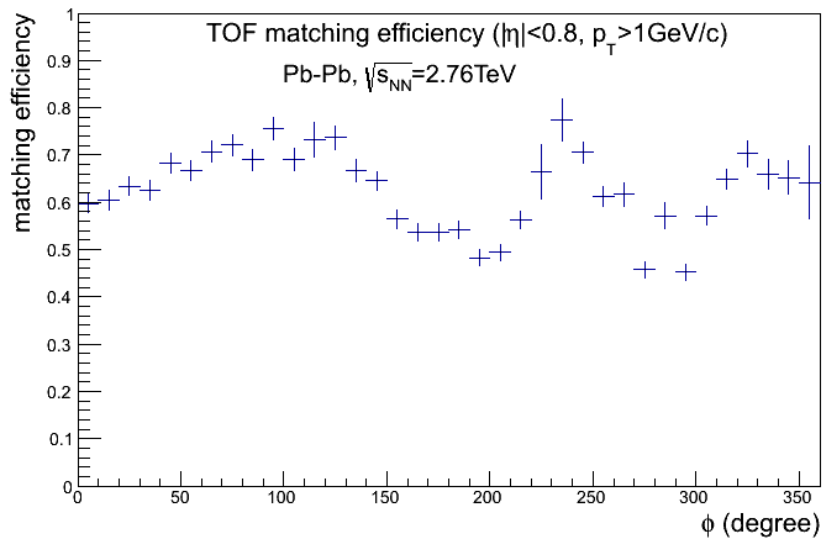


**Figure 4.6** TOF Matching efficiency as function of azimuthal angle ( $\phi$ ), for tracks with  $|\eta| \leq 0.8$  and  $p_t > 1\text{GeV}/c$ . The sample refers to a 2010 Pb–Pb run.

off. In particular, the depletion for  $|\eta| \leq 0.2$  is caused by the fact that the central modules of three SMs are not installed. One needs to take into account the number of active good channels before comparing  $\epsilon_{match}$  for different runs. This is done by normalising the efficiency to the fraction of good TOF channels from the OCDB reference maps, analogous to those of fig. 3.14. The normalised efficiency is indicated as  $\epsilon_{match}^N$ . The trending plot of the average matching efficiency for tracks with  $p_t > 1.0 \text{ GeV}/c$  (from a constant fit of the plateau of the  $\epsilon_{match}$  versus  $p_t$ ) is reported for several 2010 Pb–Pb runs in fig. 4.7, where the comparison between  $\epsilon_{match}$  and  $\epsilon_{match}^N$  is carried out. The normalisation levels the differences between runs with different readout configuration. Any further discrepancy from the trend is usually investigated at the QA level, as it may be due to issues with the TPC calibration or the primary vertex determination, that however are not to be discussed here. The

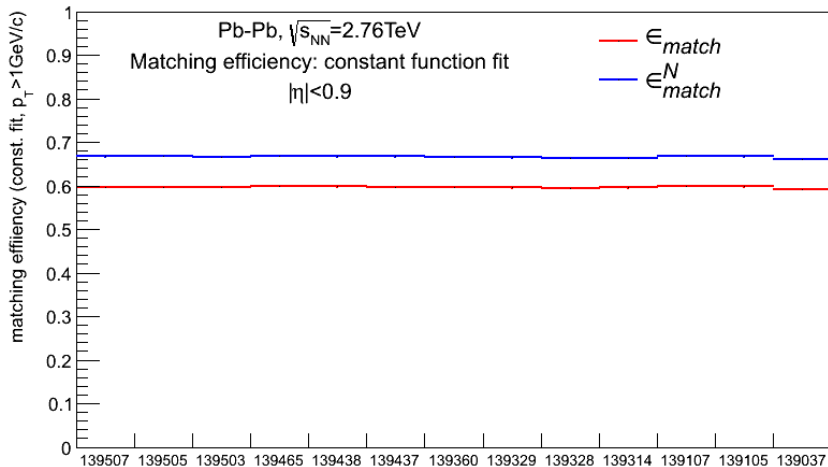


**Figure 4.7** Trending distribution for the TOF matching efficiency for different 2010 Pb–Pb runs. Tracks are here selected in the interval  $|\eta| \leq 0.9$ . The values result from the fit with a constant function of the distribution of the matching efficiency vs.  $p_t$ , for  $p_t > 1 \text{ GeV}/c$ . The red points represent  $\epsilon_{match}$ , while the blue ones represent the matching efficiency normalised to the ratio of good TOF channels,  $\epsilon_{match}^N$ .

efficiency of the matching algorithm is larger than 95% but the measured normalized saturation value is  $\epsilon_{match}^N \sim 70\%$  because of the interaction of the particles with the material in front of the TOF, the intrinsic MRPC efficiency and finally, the dead zones in the detector which reduce the geometrical acceptance.

Fig. 4.8 reports the matching efficiency as function of azimuthal angle at the outer TPC radius<sup>4</sup>,  $\phi_{out}$ . The modulation in  $\phi$  of the efficiency follows the presence

<sup>4</sup>The angle at the last track point before the TRD, namely at the TPC outer radius, is used, because the angle at the vertex does not allow to predict in which module the track will cross the TOF surface. One TOF sector covers  $\Delta\phi \sim 20^\circ$  but it has to be kept in mind that the correspondence between  $\phi_{out}$  and the TOF sector is not perfect

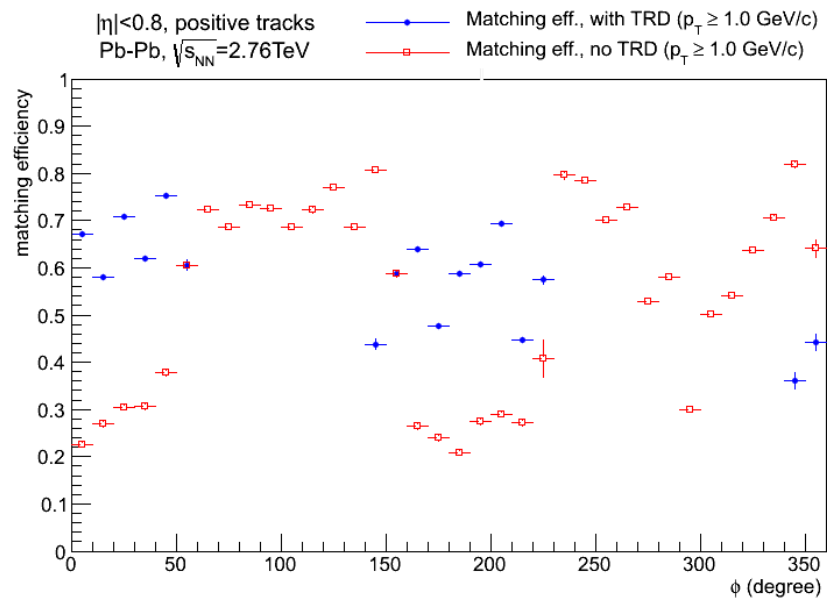


**Figure 4.8** TOF Matching efficiency as function of the azimuthal angle at the TPC outer radius, for positive tracks with  $|\eta| \leq 0.8$  and  $p_t > 1 \text{ GeV}/c$ . The sample refers to a Pb–Pb run of 2010. Red points refer to tracks that do not cross the TRD, blue points to tracks that do cross it.

of the TRD modules in front of the TOF. For the azimuthal sectors where the TRD is present (blue points in fig. 4.8), the material budget crossed by the particles before reaching the TOF is higher and so is the effect of multiple scattering, leading to a few percent lower matching efficiency. The curvature in the magnetic field for opposite charged particles causes a different behaviour for positive and negative particles at the edges of the TRD-free range. The lower values of  $\epsilon_{match}$  for  $260^\circ < \phi_{out} < 320^\circ$  are due to the fact that the central module is missing in SMs 13, 14 and 15 in correspondence of the PHOS region.

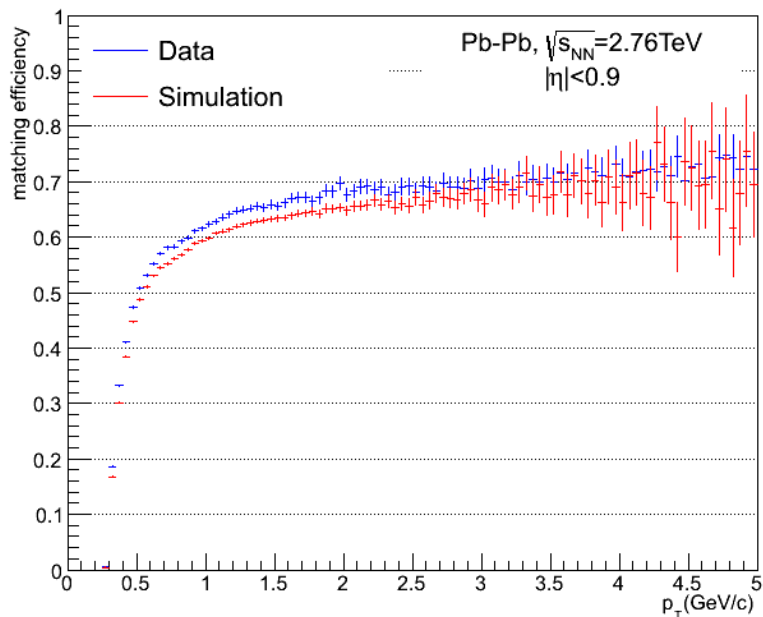


**Figure 4.9** TOF Matching efficiency as function of the reconstructed  $p_t$ , for tracks with  $|\eta| \leq 0.9$ . The red curve refers to Pb–Pb simulated events, the blue one to the data corresponding to the anchored run.

Finally, the matching efficiency has to be reproduced correctly in the Monte Carlo simulation, to reflect the detector response and be used as correction factor for any analysis on particle production. It has been verified that the Monte Carlo matching efficiency for positive and negative particle, reproduces the measured one within a few percent. In fig. 4.9, referring to a HIJING production anchored to 2010 Pb–Pb data, it is shown that  $\epsilon_{match}$  in data is a few percent (2–4%) higher than in the simulation. This is due to the fact that the pad efficiency was simulated as 2% lower than the real one. This effect has been lately corrected but it is still present in fig. 4.9, where MC is anchored to 2010 Pb–Pb data. For 2010 data analysis this contribution has to be included in the systematic error.

### 4.3 Determination of the interaction time

The determination of a particle time-of-flight requires the knowledge of the interaction time, that may differ from the nominal beam crossing by an amount related to the finite size of the bunches. In fact, the information of which particles in the bunch have collided is not available. Because the TOF detector measures the time with respect to the LHC clock, the event time,  $t_0$ , has to be measured on event-by-event basis and subtracted to the measured TOF time. This is done in three different ways in ALICE, each with a different resolution,  $\sigma_{timeZero}$ :

- as average interaction time of the LHC fill ( $t_{0,fill}$ ), that especially in pp collision can vary considerably event by event,
- by the T0 detector ( $t_{0,T0}$ ): the resolution coincides with that of the T0 detector,  $\sigma_{timeZero}=\sigma_{TZERO}$ , and can differ event by event if only one between T0A or T0C is available;
- by the TOF detector, when a sufficient amount of tracks ( $\geq 2$ ) is available ( $t_{0,TOF}$ ): in this case the resolution is event and track dependent.

#### Event time as average $t_0$ of the fill

The LHC clock and the bunches circulating in the accelerator are perfectly synchronized in the radiofrequency cavity, but they propagate in the optical fibre and in vacuum, respectively. Since the radiofrequency cavity is quite far from ALICE, they are no more synchronized when they reach ALICE. Moreover, the difference in the arrival times is not constant but it is function of the temperature. This shift, common to all TOF channels, is taken into account by subtracting the  $t_{0,fill}$  from the TOF times during the calibration stage (see section 4.1) to realign them to the LHC clock. The  $t_{0,fill}$  varies slightly within a fill but is estimated on a run basis during cpass0 and cpas1. Practically  $t_{0,fill}$  is defined as the mean of the gaussian fit to the  $t-t_{exp}$  distribution. The uncertainty associated to it,  $\sigma_{t0,fill}$ , is related to the average bunch size in the fill and can be extracted from the longitudinal spread of the vertex ( $\sigma_z/c$ ). The  $\sigma_{t0,fill}$  varies fill by fill, with dependency from the beam conditions.

The value of the  $t_{0,fill}$  is used as event time when no more precise computation is possible.

#### Event time by T0 detector

The T0 detector (see section 2.2.5) has been designed to provide the interaction time information by measuring the arrival time of particles produced in an event synchronous with the LHC clock, that travel from the IP to its photomultipliers (PMTs). The detector consists of two arrays of 12 Cherenkov counters each, T0A and T0C, placed along the beam axis at 375 cm and -72.7 cm from the interaction point, respectively. Each array provides a time measurement, indicated as  $t_{0,A}$  and

$t_{0,C}$ , that are the first signals in time detected by the counters of each side. When T0 is calibrated, the interaction time can be extracted by combining the two measurements as  $t_{0,AC} = (t_{0,A} + t_{0,C})/2$ . If only one measurement by T0A or T0C is available, due to the multiplicity of the event, the efficiency and the noise rate of the T0 detector, the event time is calculated from  $t_{0,A}$  or  $t_{0,C}$  in combination with the known  $z$  position of the primary vertex. In the following paragraphs,  $t_{0,T0}$  is used to indicate any of the  $t_{0,A}$ ,  $t_{0,C}$  or  $t_{0,AC}$ . The T0 information is used to estimate the interaction time only if  $t_{0,T0} < t_{0,cut}$ , with  $t_{0,cut} = 3\sigma_{t_{0,filt}}$ . This upper cut is applied to reject any contribution from noise and satellite collisions.

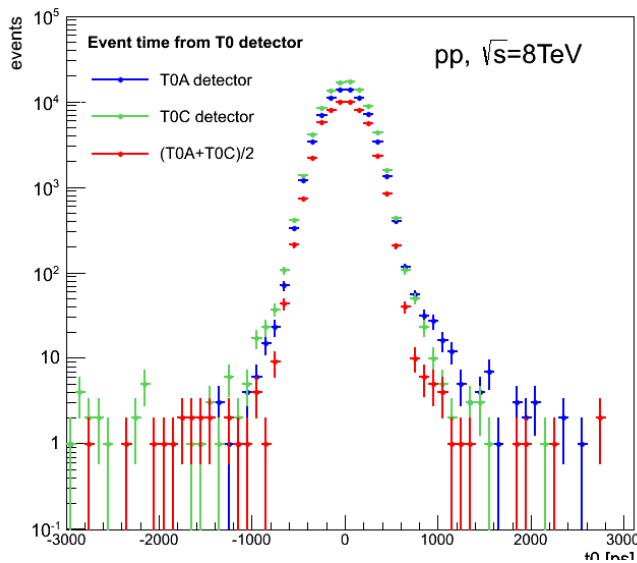


**Figure 4.10** Event time from the T0A and T0C detector,  $t_{0,A}$  (green), and  $t_{0,C}$  (blue), and the combined measurement,  $t_{0,AC}$  (red). The distributions refer to a 2012 pp run.

The distributions of  $t_{0,A}$ ,  $t_{0,C}$  and  $t_{0,AC}$  are reported in fig. 4.10 for pp collisions (2012 data taking): they are all centered around zero, as expected. Of course, the alignment of the three measurements is the primary goal of the T0 calibration. Fig. 4.11 shows the trend of  $t_{0,AC}$  for a set of 2012 pp runs after cpass1, as monitored by the TOF QA task. Each of the values reported here is the mean of the gaussian fit of the  $t_{0,AC}$  distribution, while the error bars are set to represent the gaussian width of the signals. As the result of the calibration, the time measurements are aligned within 5 ps around zero, while the spread is of the order of 200 ps.

The resolution on  $t_{0,AC}$  ( $\sigma_{AC}$ ) can be derived from the gaussian spread of the  $(t_{0,A} - t_{0,C})/2$  distribution, where  $t_{0,A}$  and  $t_{0,C}$  are corrected for the primary vertex position and the mentioned cut is applied. From fig. 4.12 one can see that the T0 detector has a resolution of  $< 40$  ps.

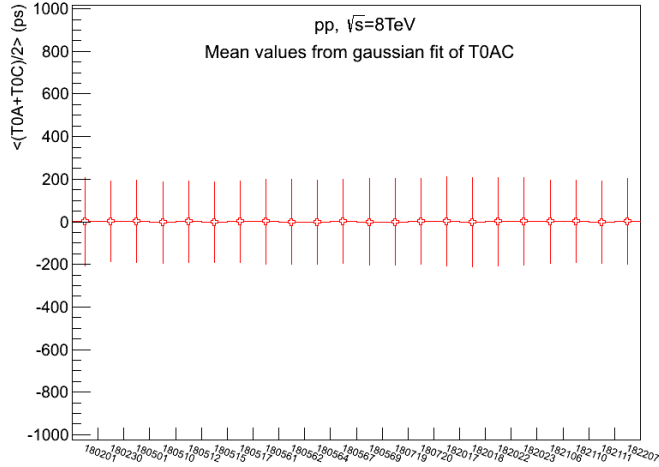


**Figure 4.11** Trend of the gaussian mean of the  $t_{0,AC}$  measurements for a set of 2012 pp runs. The error bars represent the sigma from the gaussian fit of  $t_{0,AC}$ .

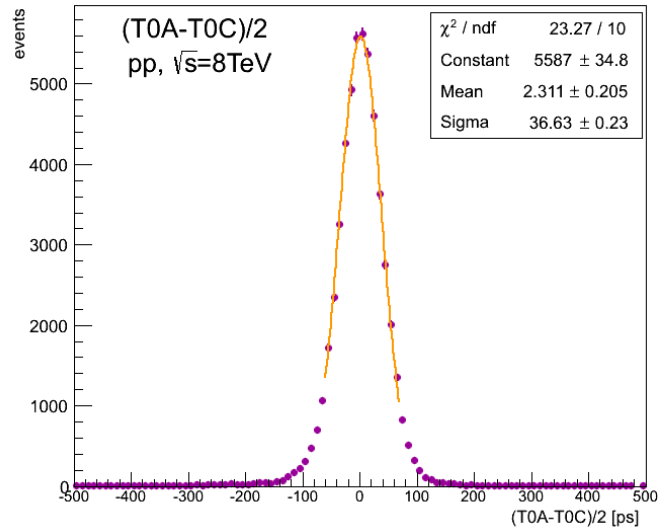


**Figure 4.12** Distribution of  $(t_{0,A}-t_{0,C})/2$  from a 2012 pp run. The gaussian fit allows to extract the  $t_{0,AC}$  resolution as the gaussian width, that here is of  $\sim 37$  ps.

### Event time by T0-TOF algorithm

When the number of tracks matching TOF is greater than 2, the event time can be computed through a combinatorial algorithm that uses the time information of the tracks matching with the TOF detector. The algorithm is totally independent from the T0 detector measurements (and calibration) and for sufficiently high track multiplicity, it leads to an important improvement of the resolution of the interaction time. In the following sections the  $t_0$  measured in this way is indicated as  $t_{0,TOF}$ , while the uncertainty associated to it is  $\sigma_{t0,TOF}$ .

In each event, the algorithm selects the tracks that satisfy the standard cuts and have a hit on TOF and groups them by maximum 10 tracks per subset. Let indicate  $N$  the number of tracks in a subsample. A mass hypothesis, most likely pion, kaon or proton, can be associated to each track, indicated with a index  $i$ , so that the possible track-species combinations are  $3^N$ . The event time offset for track  $i$ ,  $t_{0,i}(m_i)$  can be obtained as the difference between the expected time for the given mass hypothesis,  $t_{exp,i}(m_i)$ , and the TOF hit time,  $t_i^{TOF}$ :

$$t_{0,i}(m_i) = t_{exp,i}(m_i) - t_i^{TOF}. \quad (4.6)$$

The corresponding error is the combination of the uncertainties deriving from the tracking and the resolution on the TOF time,

$$\sigma_i^2 = \sigma_{trk}^2(\beta(m_i, L_i)) + \sigma_{TOF,i}^2 \quad (4.7)$$

for a total 90 ps in average. The algorithm searches for the mass hypothesis combination ( $C^*(m_1, \dots m_N)$ ) that minimizes the  $\chi^2$  defined as

$$\chi^2(C) = \sum_{i=1}^N \frac{[t_{0,i}(m_i) - \langle t_0(C) \rangle]^2}{\sigma_i^2}. \quad (4.8)$$

If a track gives a too high  $\chi^2$  contribution it is excluded from the set and the  $\chi^2$  computation is repeated. The average time zero and the corresponding error can be obtained as

$$\langle t_0(C) \rangle = \frac{\sum_{i=1}^N t_{0,i}(m_i) / \sigma_i^2}{\sum_{i=1}^N 1 / \sigma_i^2}. \quad (4.9)$$

$$\sigma(\langle t_0(C) \rangle) = \sqrt{\frac{1}{\sum_{i=1}^N 1 / \sigma_i^2}}. \quad (4.10)$$

for the combination  $C$ , so that the event time measurement finally associated to the track subset is  $\langle t_0(C^*) \rangle$ . This procedure is repeated for all the subsets. The final event time ( $t_{0,TOF}$ ) is set to the mean of the computed  $\langle t_0(C^*) \rangle$  in each set, weighted by its error  $\sigma(\langle t_0(C^*) \rangle)$ .

In order to avoid biases when doing particle identification with TOF, it is important that the track to be identified is excluded from the track sample used to evaluate the  $t_{0,TOF}$ . To this purpose, the single event track sample is divided in 10 momentum bins between 0.3 and 3.0 GeV/c. If a track belongs to the momentum interval  $j$ , the algorithm described above is applied to all tracks in the event except those in the momentum bin  $j$ . Depending on the track multiplicity of the event and on the particle  $p$  spectra, it can happen that the procedure for  $t_{0,TOF}$  is successful only for some  $p$  intervals. If this is the case, the event time is set to  $t_{0,T0}$  or  $t_{0,fill}$  with the relative uncertainty for all tracks in the remaining bins. The same obviously holds in the case that the algorithm is not able to compute  $t_{0,TOF}$  for the full track set. The  $t_{0,TOF}$  algorithm efficiency is shown in fig. 4.13 as function of the number of tracks matching with TOF, for minimum bias Pb–Pb events: the efficiency for events with at least two track matching the TOF is >50% and increases as expected with multiplicity, up to 100%.

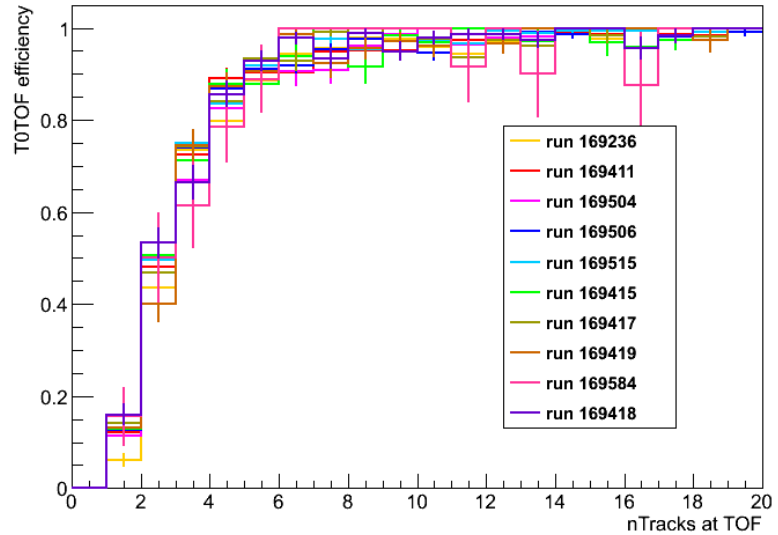


**Figure 4.13** Efficiency of the  $t_{0,TOF}$  algorithm as function of the number of TOF-matching tracks for ten different Pb–Pb runs (2011 data).

## 4.4 Particle identification performance

The measurement of the time-of-flight allows to discriminate particles by extracting their mass, as from eq. 3.1), or  $\beta = v/c$  as function of the particle momentum. The overall TOF resolution is better in Pb–Pb collisions ( $\sim 85$  ps) with respect to pp ( $\sim 120$  ps). The intrinsic MRPC resolution is fixed and so are the contributions

coming from the readout electronics. One can also consider that higher track multiplicity per event helps the calibration for the extra channel-dependent time shift (see section 4.1). The main difference however, comes from the fact that higher multiplicity Pb–Pb events lead to a more precise estimate of the event time. This is reflected into a different separation power between the species. The plots of fig. 4.14 show the comparison between the mass distributions for pp and Pb–Pb collisions, while fig. 4.15 reports  $\beta$  as function of the particle momentum. As one can see, the three particle species  $\pi$ , K and p can be clearly distinguished, together with a hint of deuterium particles in the Pb–Pb case. The continuous distribution represents instead the mismatched tracks, more abundant in Pb–Pb given the overall higher particle multiplicity per event.

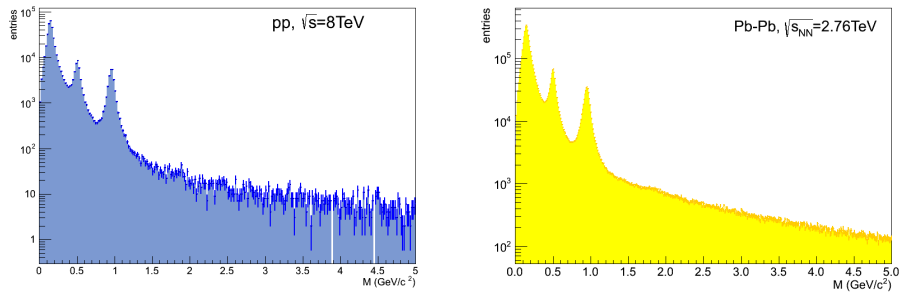


**Figure 4.14** Particle mass extracted from the time-of-flight measurement in pp (left) and Pb–Pb (right) collisions for tracks in the central pseudorapidity region, as seen from the QA analysis. The peaks relative to pions, kaons and protons (from left to right) are well distinguishable. The continuous underlying distribution is mainly due to the mismatched tracks.

It is worthy to recall now the definition of the TOF PID discriminating variable,  $N_{\sigma,i}^{TOF}$ , given in the introduction:

$$N_{\sigma,i}^{TOF} = \frac{t - t_0 - t_{exp,i}}{\sigma_{PID,TOF}}.$$

It essentially depends on the difference between the measured time-of-flight and the expected arrival time for a given mass hypothesis.  $t_{exp,i}$ ,  $i=\pi, K, p, \dots$  are also referred to as the integrated times, because they are calculated during the track reconstruction procedure as

$$t_{exp,i} = \sum_k \Delta t_{i,k} = \sum_k \frac{\sqrt{p_k^2 + m_i^2}}{p_k} \Delta l_k, \quad (4.11)$$

that is the sum of small time increments  $\Delta t_{i,k}$ , needed by the particle of mass  $m_i$  and momentum  $p_k$  to travel along the distance  $\Delta l_k$  during the track propagation step  $k$ . Because at each step the track parameters are updated, the integrated times

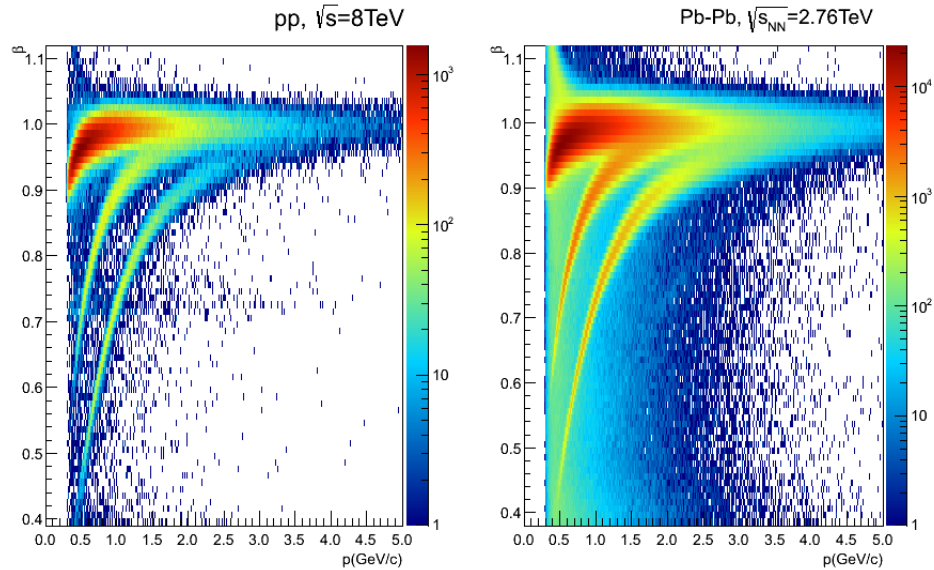


**Figure 4.15** Particle  $\beta$  as function of particle momentum  $p_t$  in pp (left) and Pb–Pb (right) collisions for tracks in the central pseudorapidity region, as seen from the QA analysis.

take into account the variations in the momentum along the trajectory due to the particle energy loss and interaction with the material.

The  $(t-t_{exp,i})$  distributions are compared with the  $(t-t_{exp}^{th})$ , that is the time difference between the measured time and the expected time-of-flight in vacuum, in fig. 4.17. The effect of accounting for energy loss during the tracking clearly improves the resolution at low  $p$ , where particles are more sensitive to material budget. It has to be specified that in fig. 4.17 the event time is not subtracted, which explains why the main bands are not perfectly aligned around zero and the resolution is not optimal.

The  $N_{\sigma,i}^{TOF}$  for the three species as function of the particle momentum are reported in fig. ?? for pp collisions and in fig. ?? for Pb–Pb. There the  $t_0$  is subtracted. For every momentum interval,  $N_{\sigma,i}^{TOF}$  corresponding to the right mass hypothesis has to be centered around zero and have a standard deviation close to unity. This ensures that the detector response in terms of observed detector resolution for a given particle species is reproduced correctly. The tracks for which the mass hypothesis is correct fill the central horizontal band. At low momenta the three bands of pions, kaons and protons are clearly distinguishable. They start to superimpose as  $p$  increases, due to the reduced separation power of the TOF detector at higher momentum. The PID selection in terms of  $N_{\sigma}^{TOF}$  for the  $K^{*0}$  reconstruction will be shown in chapter 5.

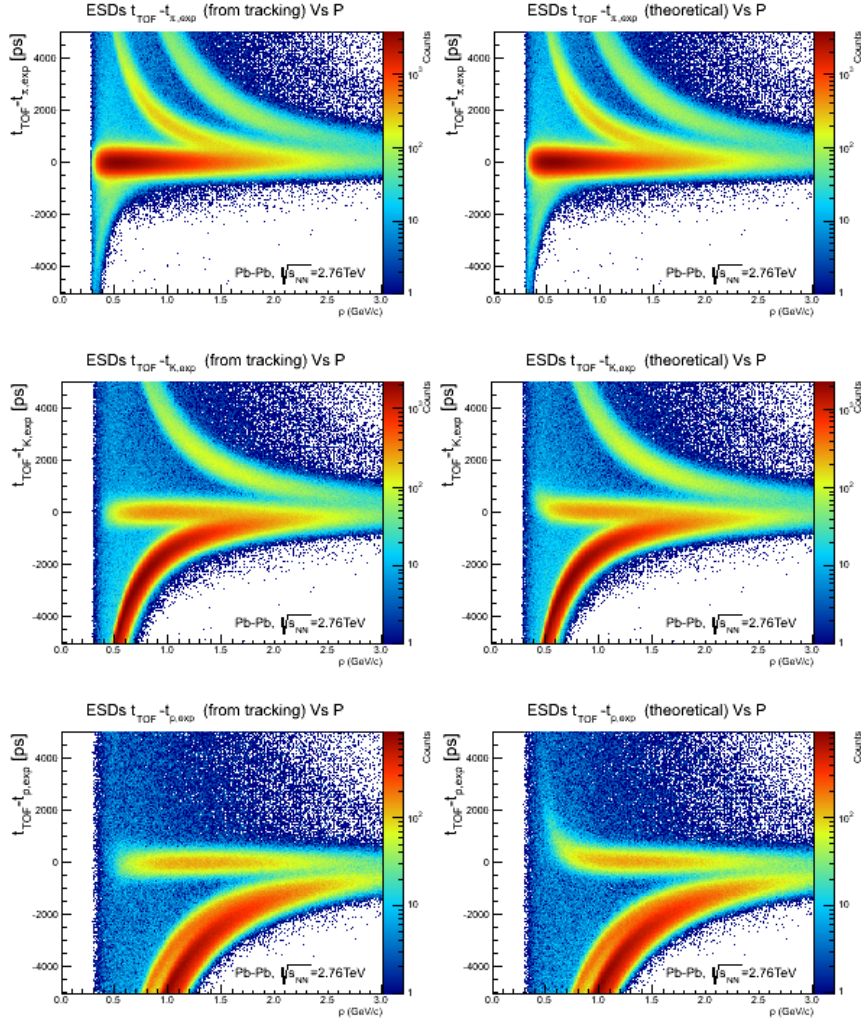


**Figure 4.16** The plots in the left column show  $(t-t_{exp,i})$  as function of  $p_t$  for  $\pi$  (top),  $K$  (middle),  $p$  (bottom). On the right, the distributions of  $(t-t_{exp,i}^h)$  for the corresponding species are reported.  $t_{exp,i}^h$  represent the expected time-of-flight for a given mass hypothesis in vacuum, while  $t_{exp,i}$  are the integrated times determined by the ALICE tracking procedure. Data are from a 2010 Pb–Pb run.

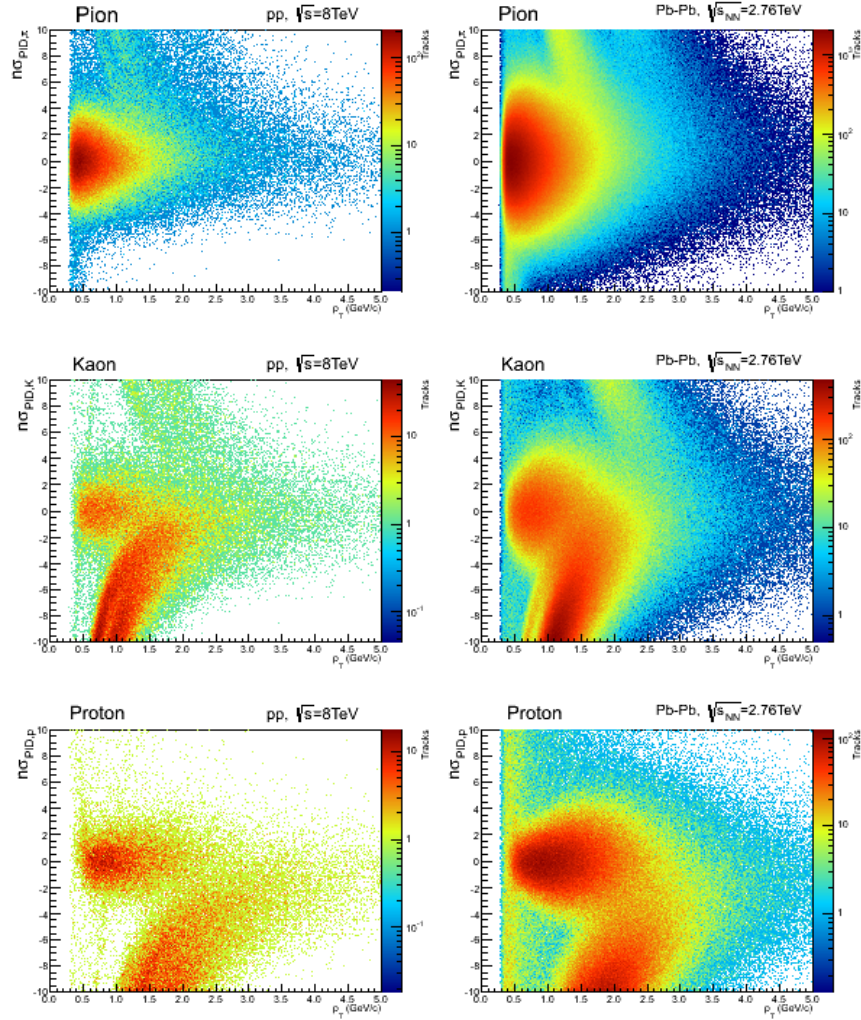


**Figure 4.17** Distribution of  $N_{\sigma,i}^{\text{TOF}}$  for  $\pi$  (top),  $K$  (middle),  $p$  (bottom) in  $\text{pp}$  (left) and  $\text{Pb-Pb}$  collisions (right). Data are processed within the QA analysis. In particular, the same track cuts have been applied at this level for the  $\text{pp}$  and  $\text{Pb-Pb}$  case.

## Overview

In the previous sections all the ingredients that are needed to ensure good performance of the TOF particle identification have been discussed. The matching efficiency must be as high as possible. Despite the fact that the matching algorithm efficiency is  $\sim 95\%$ , the actual  $\epsilon_{match}$  is limited to lower values by the readout efficiency, the material budget in front of the TOF modules, the magnetic field and the detector dead zones. It has been showed that taking into account the number of good readout channels the average matching efficiency is around  $\epsilon_{match}^N \sim 70\%$  (see 4.2).

The channel-by-channel calibration is of fundamental importance to achieve the best resolution possible for the TOF hit time. The intrinsic MRPC resolution, smaller than 50 ps has to be considered together with the contribution from the readout electronics, that is  $\sim 40$  ps. The overall time-of-flight resolution is then partially determined by the uncertainty on the measurement of the event time, as described in section 4.3. Depending on the strategy used to obtain  $t_0$ , the resolution may vary between few tenths of ps to  $\sim 90$  ps if  $t_{0,TOF}$  is available, or be  $\sim 50$  ps if the information from the T0 detector is available, or, in the worst case, it can be determined as the spread of the  $t_{0,full}$ , that is of the order of 200 ps, determined by  $\sigma_z/c$ . In Pb–Pb collisions, given the high particle multiplicity,  $t_{0,TOF}$  is available in almost 99% of the events, that makes it suitable to be used as  $t_0$  estimator for the analysis presented in the next chapter.

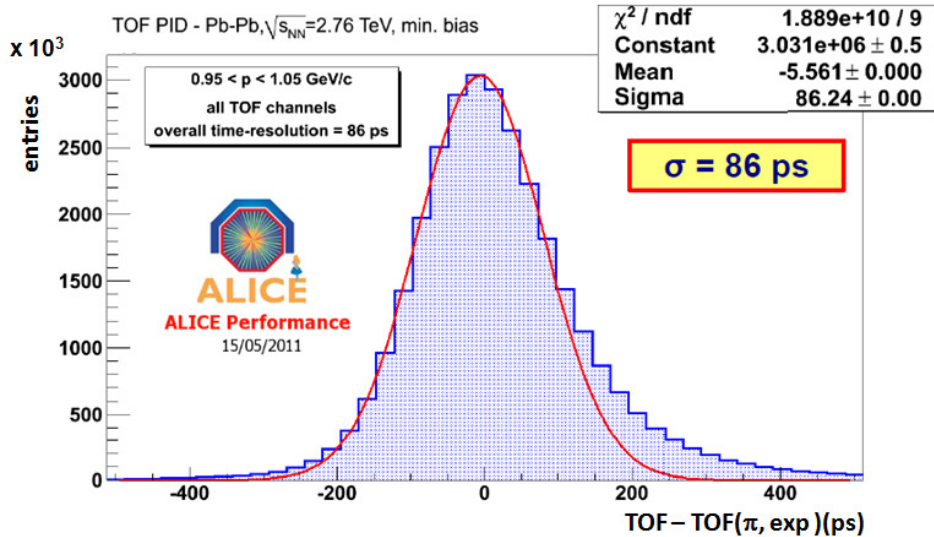


**Figure 4.18** TOF overall resolution measured in 2010 Pb–Pb collisions. The event time has been estimated with the TOF algorithm as discussed in the text.

The overall TOF resolution has been measured in Pb–Pb collisions, for events

where  $t_{0,TOF}$  was available, and it is reported in figure 4.18. The average value is  $\sigma_{TOF} \sim 86$  ps, very close to the design target ( $\sim 80$  ps). As a consequence, a  $2\sigma$  separation of  $\pi$  from K and K from p is possible up to 3.0 GeV/c and 4.5 GeV/c respectively, as shown in fig. 4.19. Starting from these considerations, the TOF PID is well suited to be exploited in the resonance analysis, and especially for the  $K^{*0}$  production study through its hadronic decay channel ( $K^{*0} \rightarrow K^\pm \pi^\mp$ ) where the kaon identification is crucial.

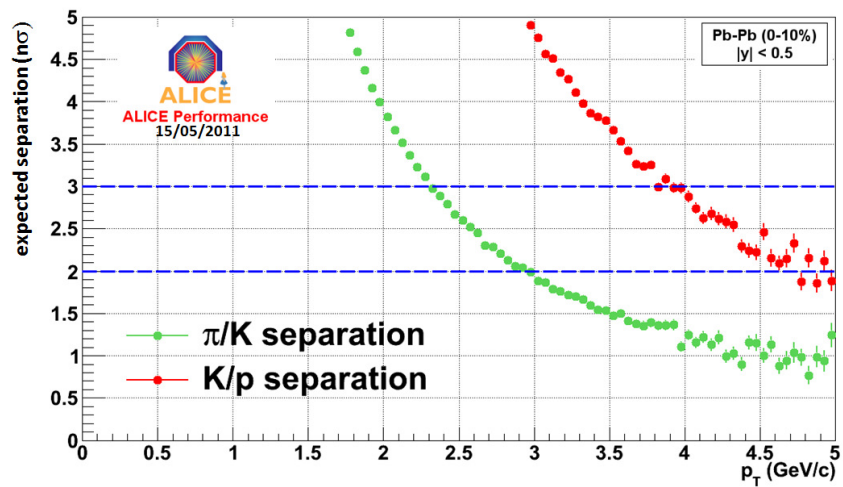


**Figure 4.19** Expected  $\pi$ /K and K/p separation in Pb–Pb collisions as function of the particle transverse momentum.

## Chapter 5

# Measurement of $K^{*0}$ production in Pb–Pb collisions

The measurement of resonance production in ultra-relativistic heavy-ion collisions provides information on the properties of the hadronic medium and different stages of its evolution. The measurement of the short-lived resonances allows to estimate the time span in the hadronic phase between the chemical and the kinetic freeze-out. The  $K^*(892)$  resonance production at central rapidity ( $|y| \leq 0.5$ ) is measured in Pb-Pb collisions at  $\sqrt{s_{NN}} = 2.76$  TeV with the ALICE experiment, via the reconstruction of its hadronic decay into  $K\pi$ . For this measurement, up to intermediate  $p_t$ , the particle identification with the Time-Of-Flight has been exploited. The TOF PID allow to extend the reach in transverse momentum of the measured spectra and to reduce the systematic uncertainty on the extracted resonance parameters at intermediate  $p_t$ . The resonance spectra will be presented as a function of centrality.

### 5.1 $K^{*0}$ reconstruction in Pb–Pb collisions

The  $K^{*0}$  production in Pb-Pb interactions at  $\sqrt{s_{NN}} = 2.76$  TeV at midrapidity has been studied with data collected in November and December 2010 by ALICE in four different centrality classes (see section 5.1.1), from very central to peripheral collisions. The analysis strategy is based on the invariant mass study of the reconstructed pairs (referred to as the candidates) whose provenance could be the decay of a  $K^{*0}$  meson into charged particles. The decay products (also called daughters in the text) are identified as oppositely charged pions and kaons among the tracks reconstructed in the central barrel. The track selection and the particle identification strategy is described. The raw signal yield is extracted by fitting the background-subtracted invariant mass distribution in several transverse momentum intervals. In order to extract the  $p_t$ -dependent cross section, these yields are corrected for efficiency. The  $p_t$ -dependent correction due to the detector acceptance and reconstruction efficiency,  $(\text{Acc} \times \epsilon_{rec})(p_t)$ , is computed from a Monte Carlo simulation, that describes at the relative per cent level the detector geometry and response. The

reconstruction efficiency, in particular, comprises the contribution of the tracking and candidates selection cuts. An additional  $p_t$ -independent efficiency factor that accounts for the PID of the daughters,  $\epsilon_{PID}$ , is applied. The absolute normalisation is then performed, by dividing for the number of the total events,  $N_{evt}$ . In summary, the yields can be computed from the formula:

$$\frac{dN_{K^{*0}}}{dp_t} \Big|_{|y|<0.5} = \frac{1}{2} \frac{1}{N_{evt}} \frac{1}{\Delta y \Delta p_t} \frac{N_{K^{*0}}(p_t)}{(Acc \times \epsilon_{rec})(p_t) \cdot \epsilon_{PID} \cdot B.R.} \quad (5.1)$$

After the efficiency unfolding, the corrected yield is divided by the branching ratio (B.R.) of the decay channel of  $K^{*0}$  into charged particles, in order to extract the total number of  $K^{*0}$  mesons. The measurement of the yields (or the cross sections) is performed for both particles and antiparticles, so that an additional factor 1/2 has to be considered to take into account particles only.

### 5.1.1 Data sample and event selection

During 2010 heavy-ions data taking the most used trigger setup for the central barrel was the minimum bias selection, where the main detectors involved are SPD and V0: a trigger was issued if there was at least one signal in one of the two V0 sides, or if one fast-or chip of the SPD was fired. At the beginning of the data taking the same trigger as in pp minimum bias collisions was used, to allow to collect very peripheral and ultra-peripheral collision events as well. Later, the trigger was tightened to reduce electromagnetic background that is two orders of magnitude bigger than the hadronic interaction rate and the trigger logic became the requirement of two out of three signals including the two signals of the V0 detector and one fast-or of the SPD. In the third phase of the data taking the AND logic of V0A and V0C was used and in the last period all the three signals (V0A, V0C and SPD fast-or) were required simultaneously. With this trigger setup ALICE collected about  $30 \times 10^6$  minimum bias Pb–Pb events in 2010.

For this analysis a sample of  $17 \times 10^6$  minimum bias Pb–Pb events has been processed, from a selection of the runs where ITS, TPC and TOF performance were validated by the QA chain and declared as optimal. Out of this sample,  $\sim 12 \times 10^6$  events satisfy the following selection criteria and have been actually used for the analysis:

- primary vertex information available from the SPD or TPC tracks, with the  $z$  coordinate of the primary vertex ( $V_z$ ) falling within  $\pm 10$  cm from the interaction point,
- centrality between 0 and 80%.

The distribution of the vertex  $z$  position of the accepted events is reported in fig. 5.1. Events with  $|V_z| < 10$  cm have been used to ensure a uniform acceptance in the central pseudorapidity region,  $|\eta| < 0.8$ , where the analysis is performed. This cut reduces the total number of events to  $\sim 15 \times 10^6$ , that is the  $\sim 88\%$  of the initial

sample. A gaussian fit of the distribution shows that the vertex is centered around 0.5 cm along the z axis, in average.

The centrality is defined as the percentage of the total hadronic Pb–Pb cross section and it is estimated in different ways in ALICE [13]. For this analysis the centrality value is taken from the analysis of the V0 scintillator measured amplitudes. A small fraction ( $\leq 0.1\%$ ) of events, falling in the centrality range 0–1% have been discarded because the centrality value estimated from V0 amplitudes is not compatible with the measurement of centrality through track multiplicity. Fig. ?? reports the centrality distribution for the accepted events in the centrality range between 0 and 80%, which looks flat as expected. The events in the range 90–100% have not been considered for the analysis, being contaminated by background events and being triggered with efficiency lower than 100%. The analysis could be extended to the most peripheral centrality bin 80–90%, which has not been considered for the study presented here due to statistics limitations. The remaining selected  $12 \times 10^6$  events are binned in four centrality intervals, according to the following: 0–20%, 20–40%, 40–60%, 60–80%. The number of accepted events per each centrality bin is reported in table 5.1 and is used for the absolute normalisation of the yields.

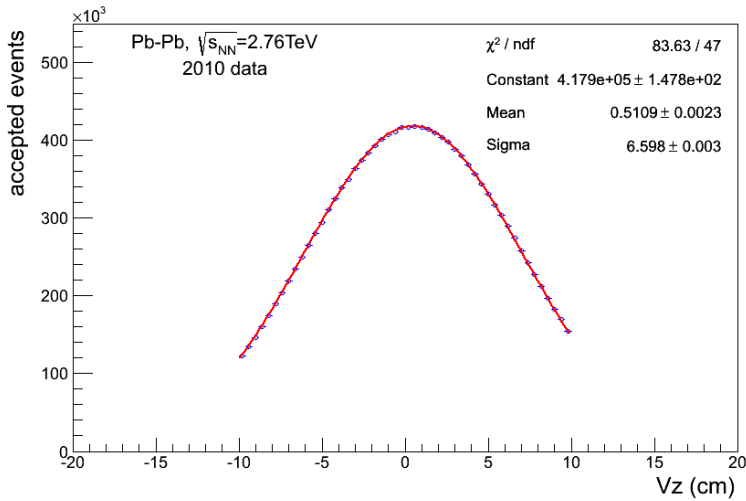


**Figure 5.1** Vertex  $z$  coordinate distribution of the accepted events in the full centrality range, 0–100%. The red continuous line represents the result of a gaussian fit of the distribution.

The reaction plane is defined by the beam axis  $z$  and the impact parameter direction. The angle of the reaction plane,  $\psi_R$ , is measured from the global tracks and is defined as:

$$\psi_R = \frac{1}{2\sqrt{N}} \arctan \frac{\sum_{i=1}^N \sin(2\phi_i)}{\sum_{i=1}^N \cos(2\phi_i)} \quad (5.2)$$

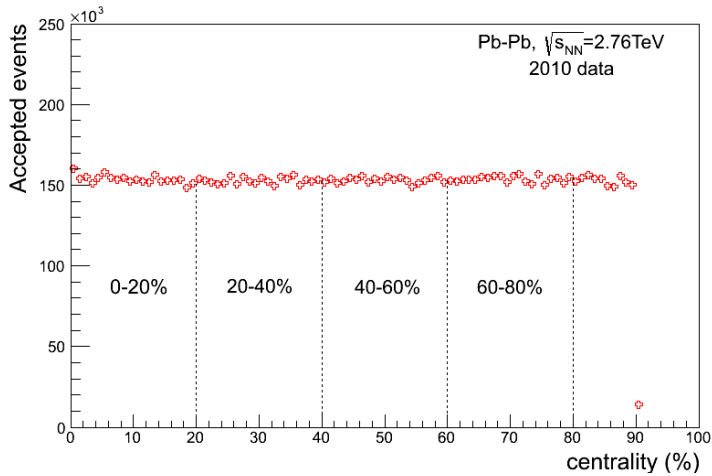


**Figure 5.2** Centrality distribution of the accepted events in the range 0–100%. The dashed lines and the labels define the four intervals in which the analysis is performed.

Centrality	Accepted events
0-20%	$3.069377 \times 10^6$
20-40%	$3.055345 \times 10^6$
40-60%	$3.059987 \times 10^6$
60-80%	$3.073845 \times 10^6$

**Table 5.1** Number of accepted and analysed events per centrality interval.

where  $N$  is the number of tracks and  $\phi$  their azimuthal angle. The distribution of the reaction plane angle, reported in fig. 5.3, is flat, as expected if the event plane reconstruction by the detector is homogeneous, that is important to avoid a bias on the event selection. No cuts on the reaction plane angle have been applied for the event selection itself, but the event plane information is used for the event-mixing background technique (see section 5.1.4), where one wants to compute invariant mass pairs from different events that have similar “shape”.

### 5.1.2 Track selection

The  $K^{*0}$  is studied by reconstructing its hadronic decay into charged particles  $K^\pm\pi^\mp$  (B.R. = 66.6%). Because of its very short lifetime of  $\sim 4$  fm/c, the resonance decays early after its production and does not make it out of the beampipe. The selection of the candidate daughters is a challenge for the  $K^{*0}$  reconstruction, because the produced kaon and pion are undistinguishable from the charged primary particles produced in the “bulk”.

The candidate resonance daughters with  $0.15 < p_t < 20.0$  GeV/c in the pseudorapidity interval  $|\eta| < 0.8$ , are first of all selected by applying cuts on the quality of

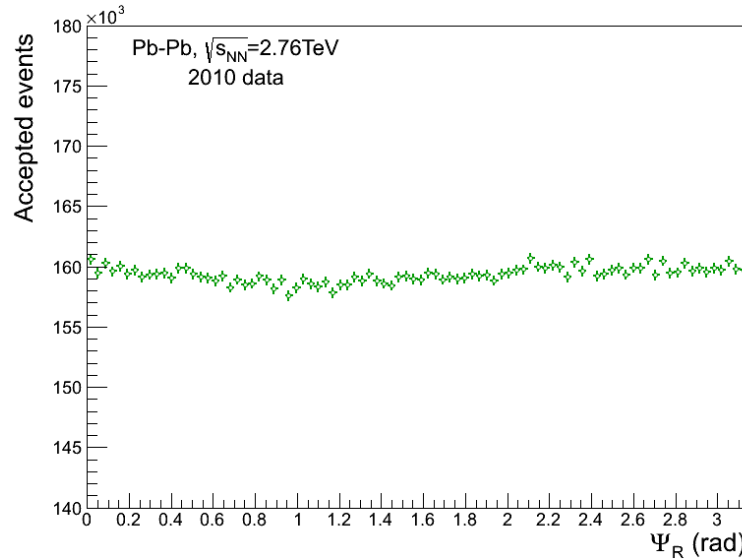


**Figure 5.3** Reaction plane angle distribution of the accepted events in the range 0-100%.

the reconstruction, related to:

- the number of clusters associated to the track in the TPC,  $N_{cls} \geq 70$ ,
- the quality of the track fitting (done using the Kalman algorithm),  $\chi^2 / \text{cluster} \leq 4.0$ ,
- successful refit of the reconstruction algorithm, from the outer layer of the detector to the primary vertex, through TPC and ITS.

In order to select only the tracks that point to the primary vertex, defined as primaries, it is required that they have at least one associated cluster in one of the two layers of the SPD and additional cuts are imposed on the distance of closest approach (DCA), that is related to the impact parameter. The DCA is the minimum distance between two tracks trajectories, that is ideally zero if the two tracks come from the same point. The resolution on the DCA is determined by the detector resolution on the track position measurement. For this analysis it is required that the component in the direction parallel to the beam is  $DCA_z \leq 2.0$  cm, while the component in the radial direction must satisfy the relation  $DCA_r(p_t) \leq 0.0182 + 0.0350 p_t^{-1.01}$ , that takes into account the deflection of the trajectories in the magnetic field. Kink<sup>1</sup> daughters are rejected. The cuts listed above define the “standard quality cuts”.

Finally, a cut on the reconstructed pair rapidity is applied, in order to select only the resonance candidate produced at midrapidity, that is with  $|y| < 0.5$ .

<sup>1</sup>The kaon decays such as  $K^\pm \rightarrow \mu^\mp \nu$  inside the active volume of the detectors are defined “kinks”.

### 5.1.3 Particle identification with Time Of Flight

For the  $K^{*0}$  analysis presented here, particle identification is mandatory to identify the kaon and to remove as much as possible the combinatorial background coming from the association of two pions into a candidate pair. As discussed in section 2.2, ALICE provides several methods to identify particles, among which the measurement of the energy loss in the TPC and that of time-of-flight in TOF. One of the possible PID strategies is the “ $n\sigma$ -cut” method. Let  $i$  indicate the detector used for PID ( $i = \text{TPC}, \text{TOF}$ ) and  $j$  the particle species hypothesis. This method is based on the definition of a discriminating variable  $n_{i,j}^{\sigma PID}$  as

$$n_{i,j}^{\sigma PID} = \frac{X_j - X_{i,j}^{\exp}}{\sigma_{i,j}^{\sigma PID}} \quad (5.3)$$

where  $X_j$  is a measured observable in the detector  $i$ ,  $X_{i,j}^{\exp}$  is the prediction of that observable’s value in the mass hypothesis  $j$  and  $\sigma_{i,j}^{\sigma PID}$  is the resolution on the measurement. Particle identification is then performed by applying an appropriate cut on the discrimination variable. If one intends to exploit the TPC,  $X_{\text{TPC}}$  is the particle energy loss,  $dE/dx$ . With TOF,  $X_{\text{TOF}}$  is the measured time and the above definition 5.3 reads as 4.1. The TPC and TOF response for kaon hypothesis are reported in fig. 5.4 for the tracks selected with the standard cuts, from the full dataset used for the  $K^{*0}$  analysis. The response of the TPC is plotted in terms of the  $n_{\text{TPC},K}^{\sigma PID}$  as function of the momentum reconstructed at its inner radius,  $p_{\text{TPC}}^2$ , while the TOF response is given by  $n_{\text{TOF},K}^{\sigma PID}$  as function of  $p$ . A  $2\sigma$  cut (dashed bold lines on the plots) on the TPC signal allows to separate K from  $\pi$  for  $p_{\text{TPC}} < 0.6\text{--}0.7 \text{ GeV}/c$ , while using the TOF information it is possible to go up to  $p \sim 2.5 \text{ GeV}/c$ . The  $\pi/K$  separation power of TOF is shown in fig. 4.19 as function of the particle transverse momentum.

The particle identification strategy for the analysis presented in this work exploits the capabilities of the TOF for the kaon identification, aiming to extend the  $K^{*0}$  measurement to higher  $p_t$  than possible by using the TPC PID only (see section 1.3.2). Here, the TPC PID is also used as veto in order to reject the main contribution to the combinatorial background from low-momentum mismatched tracks, as described also later. Because of the natural kinematic cutoff of low momentum particles ( $p_t < 0.3 \text{ GeV}/c$ ) that do not reach TOF,  $K^{*0}$  with  $p_t < 1 \text{ GeV}/c$  cannot be reconstructed with TOF PID only.

#### TOF matching and PID cuts

In order to identify reconstructed tracks that have a signal in the TOF it is necessary to impose the TOF-matching requirement. As mentioned before, because of the magnetic field and the distance of the TOF from the beam pipe, particles with

---

<sup>2</sup>The energy loss in the TPC depends on the momentum of the particle when it first enters the detector, therefore at the inner radius.  $p$  indicates instead the momentum reconstructed at the vertex.

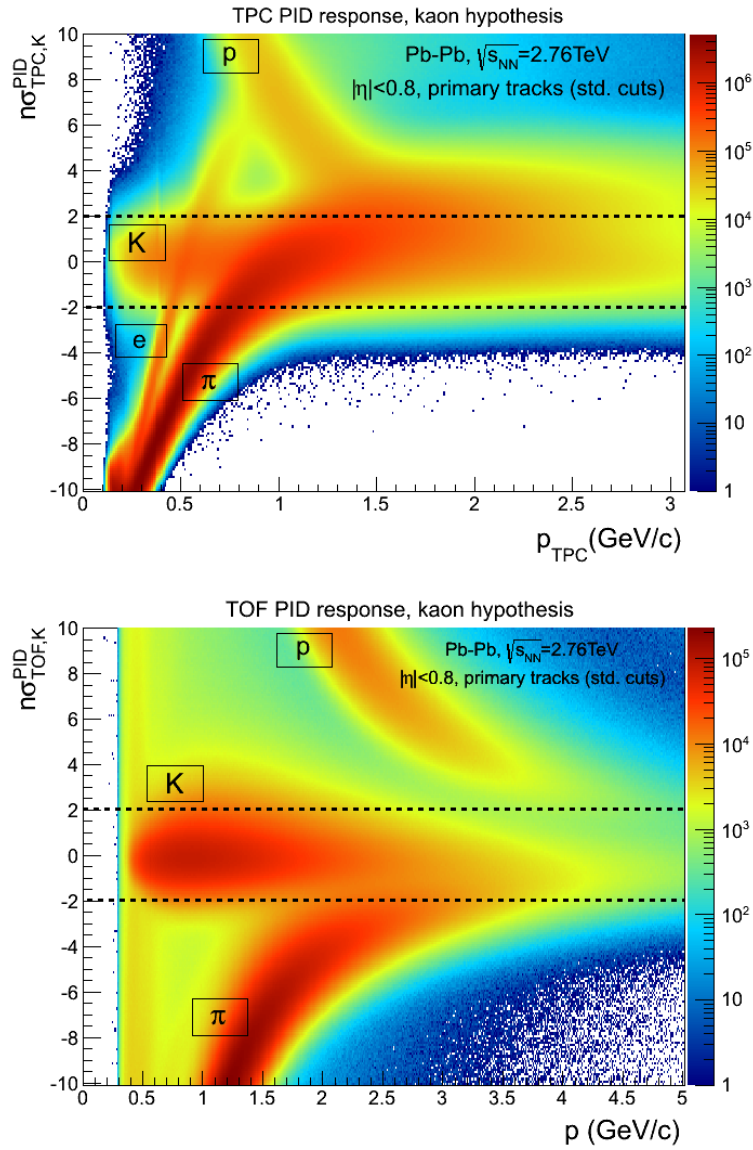


**Figure 5.4** TPC (top) and TOF (bottom) response for kaon hypothesis in terms of  $n_{\sigma}^{\text{PID}}_{\text{TPC},K}$  as function of the particle momentum at the inner radius of the TPC and  $n_{\sigma}^{\text{PID}}_{\text{TOF},K}$  as function of the particle momentum at the vertex, respectively. The black dashed lines mark a  $2\sigma$  selection.

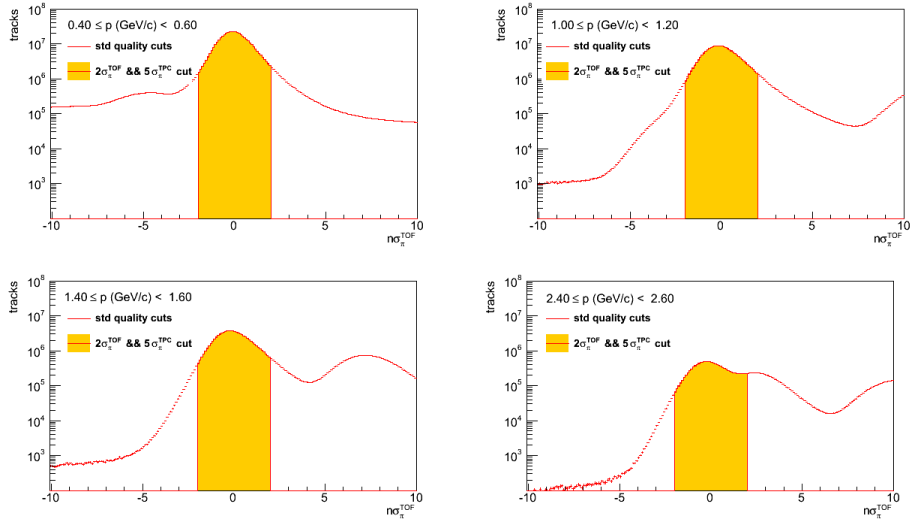


**Figure 5.5** Example of TOF PID cut for four different momentum interval for the pion hypothesis. The  $5\sigma$  cut on the TPC PID to exclude mismatched tracks is also applied.

transverse momentum below 300 MeV/c do not reach the detector, so the TOF match effectively implies an additional cut on the daughters  $p_t$ .

The candidate  $K^{*0}$ 's daughters are  $\pi$  and K identified via a  $2\sigma$  cut on the TOF signal in the full  $p_t$  range. The total TOF time resolution is determined by three contribution (see section 4.1), the intrinsic time resolution of the detector and associated electronics, the tracking and the start time. The start time of the event has been computed with the TOF algorithm, so that  $t_0 = t_{0,TOF}$  (see section 4.3). The overall TOF resolution is found to be about 85 ps for pions with  $p_t=1$  GeV/c. In order to reduce the contribution of the mismatched tracks, an additional  $5\sigma$  cut on TPC energy loss has been applied. A track identified within  $2\sigma$  as a pion (or a kaon) by TOF is rejected if it is not identified as a pion (or a kaon) also by a  $5\sigma$  cut on the TPC signal. The coloured bands in figs. 5.5 and 5.6 represent the tracks surviving the PID selection for the pion and kaon hypothesis, respectively, for different transverse momenta. The contribution of the mismatch is relevant for low momentum tracks, up to 1.0 GeV/c. The effect of this cut is particularly evident in the top left distribution of fig. 5.6, that is the case of  $0.4 < p < 0.6$  GeV/c kaons: in the  $\pm 2\sigma_{TOF,K}^{PID}$  range, the mismatch cut discards  $\sim 8\%$  of the particles identified by TOF as K, because their identity is not compatible with that found by the TPC.

The ratio of primary tracks that are identified as pions and kaons as described above as function of the single-track transverse momentum is reported in fig. 5.7. For  $p_t > 3.5$  GeV/c the ratios for pions and kaons are comparable, suggesting that a  $2\sigma$ -cut on TOF signal is not sufficient to separate sharply the two species and that above this momentum the contamination of pions to kaon identification may not be negligible.

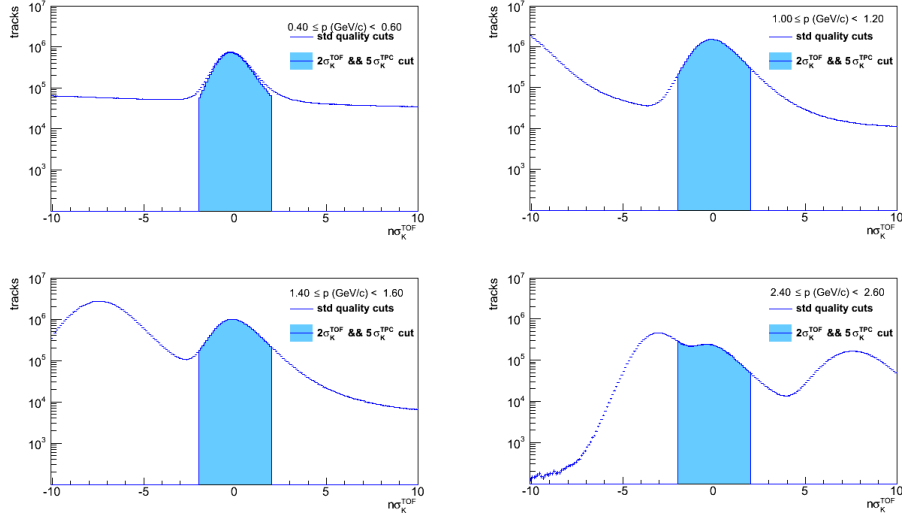


**Figure 5.6** Example of TOF PID cut for four different momentum interval for the kaon hypothesis. The  $5\sigma$  cut on the TPC PID to exclude mismatched tracks is effective for  $p_t < 1.0 \text{ GeV}/c$ .

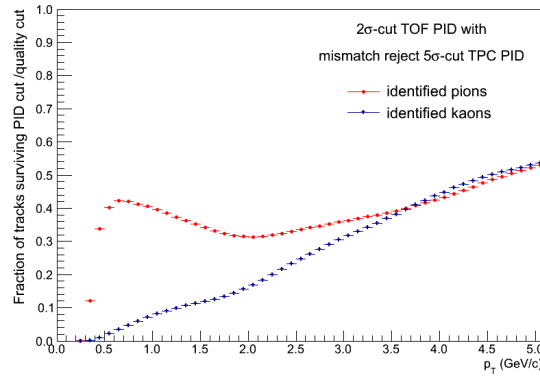


**Figure 5.7** Ratio of tracks that are selected by the PID cuts (including TPC mismatch reject cut) for the pion (red) and kaon (blue) hypothesis over the tracks that pass the quality cuts for primary particles as function of their transverse momentum.

### 5.1.4 Signal extraction

The candidate resonance invariant mass ( $M_{inv}$ ) distribution is obtained from the combination of primary identified kaons and pions from the same events into unlike-sign pairs, as a function of the event centrality and the resonance transverse momentum. The distributions for  $K^+ \pi^-$  and  $K^- \pi^+$  are obtained separately and then summed bin by bin to obtain the total signal for  $K^{*0}$  and  $K^{*0}$ . In the following sections these distributions are indicated as US(-+) and US(+), respectively, while US indicates the sum of the two. The  $K^+ \pi^-$  and the  $K^- \pi^+$  invariant mass distributions and their ratio are reported in fig. 5.8 for the most central events (0–20%) and resonance in the range  $1.0 \leq p_T \leq 10.0$  GeV/c<sup>2</sup>. The ratio exhibits a slight  $M_{inv}$  dependence and it decreases from 8 to 6% towards higher  $M_{inv}$  values. This effect could be related to the different abundance of reconstructed  $K^+$  and  $K^-$  that are combined into pairs. In order to extract the  $K^{*0}$  signal it is necessary to remove or,

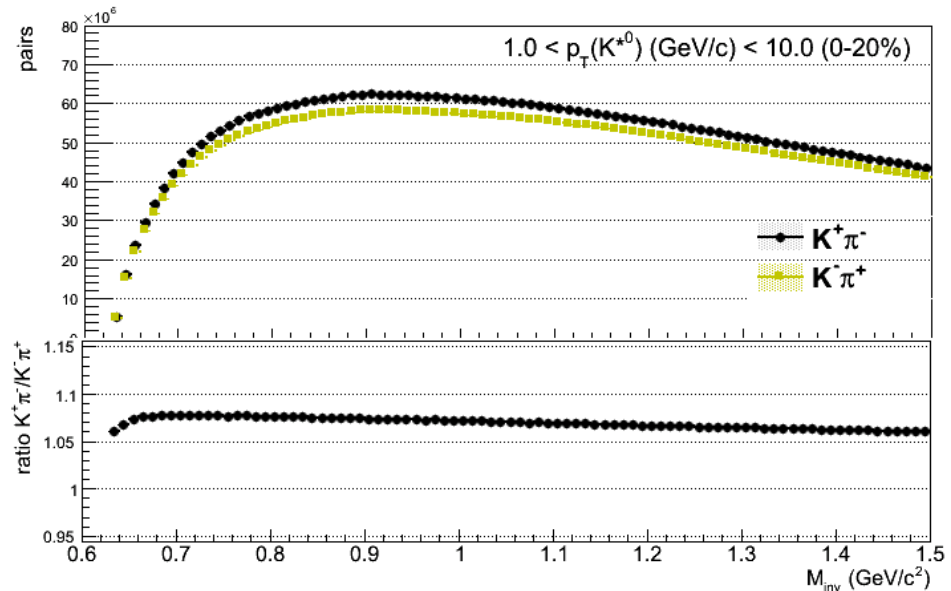


**Figure 5.8** Unlike-sign charge particle pairs distribution for  $K^+ \pi^-$  and  $K^- \pi^+$  (top) and their ratio (bottom) for pairs with  $1.0 \leq p_T \leq 10.0$  GeV/c, for events with 0 to 20 % centrality.

at least reduce, the combinatorial background. For this analysis, this has been done with the event mixing (EM) technique: the background invariant mass distribution is built by combining uncorrelated unlike-sign charged identified kaons and pions from different events. When applying this method, it is important to combine pairs from events with similar topology and multiplicity, to reproduce satisfactorily the kinematics properties of the combinatorial background. The events for the mixing have been selected by applying the "similarity" criteria listed below:

- difference in the z coordinate of the primary vertex position,  $\Delta z_{vtx} \leq 1.0$  cm
- difference in centrality,  $\Delta C \leq 10$
- difference in the reaction plane angle,  $\Delta \Psi_R \leq 20^\circ = 0.35$  rad.

A maximum of 5 events at the time have been considered for mixing and the same criteria have been applied for the primary tracks selection and PID. The background distributions for  $K^+ \pi^-$  (EM(+-)) and  $K^- \pi^+$  (EM(-+)) have been obtained separately and then summed, as done for the signal US distribution. The distributions  $K^+ \pi^-$  and  $K^- \pi^+$  differ by a 7% due to the lower abundance of  $K^-$  with respect to  $K^+$ , both in same event and event mixing. The total event mixing invariant mass distribution has to be normalised to the US distribution before subtraction, because the statistics of the EM distribution is higher as consequence of the number of mixed events. The normalisation range  $1.3 \leq M_{inv} \leq 1.5$  GeV/c<sup>2</sup> was chosen, because far from the signal peak. Bottom panel of fig. 5.9 shows that the ratio between the US and EM pairs from the same event and mixed events (after normalisation) respectively, is close to 1 within 0.5% and is the same for  $K^+ \pi^-$  and  $K^- \pi^+$ . This justifies the sum of the  $K^+ \pi^-$  and  $K^- \pi^+$  distributions, to take into account particle and anti-particle.

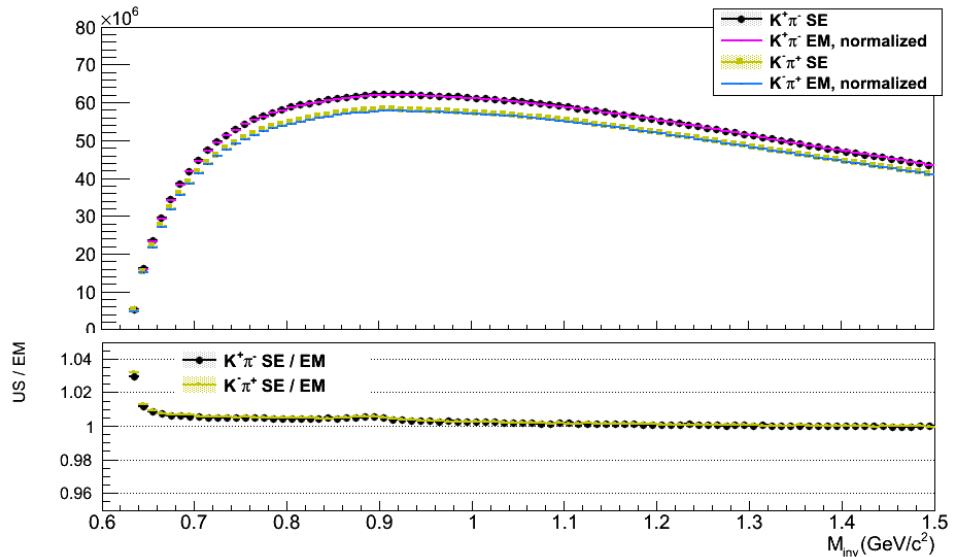


**Figure 5.9** Unlike-sign charge particle pairs distribution for  $K^+ \pi^-$  and  $K^- \pi^+$  from same event and event mixing (on the top) and their ratio (on the bottom) for pairs with  $1.0 \leq p_t \leq 10.0$  GeV/c, in the 0 to 20 % centrality events.

After the background subtraction, the resulting distribution exhibits the characteristic peak of the resonance signal and a residual background, which are fitted in order to extract the raw yield and the resonance parameters. The strength of the

signal can be expressed in terms of the statistical significance,  $\mathbb{S}$

$$\mathbb{S} = \frac{S}{\sqrt{S+B}} = \sqrt{S} \frac{1}{\sqrt{1+1/R}} \quad (5.4)$$

where  $R = S/B$  is the ratio between the integral of the signal and that of the background in a common range around the signal peak. The significance quantifies how much the signal stands out from the statistical fluctuations of the background and it is intimately related to the signal over background ratio, that depends on the power of the selection cuts. The integrated signal for  $1.0 \leq p_t \leq 10.0$  GeV/c in the 0 to 20 % most central collisions (see fig. 5.10) has a significance of nearly 800.

### 5.1.5 Invariant mass fit

The fit of signal distribution is performed after event mixing background normalisation and subtraction, with the RooFit package [?] which uses MINUIT [?]. The resonance peak is shaped with a non-relativistic Breit-Wigner function, while Chebychev polynomial function was chosen to fit the residual combinatorial background,  $bg(M_{K\pi})$ . The total fit function is the sum of the Breit-Wigner and  $bg(M_{K\pi})$ :

$$f(M_{K\pi}) = \frac{Y}{2\pi} \frac{\Gamma_0}{(M_{K\pi} - M_0)^2 + \frac{\Gamma_0^2}{4}} + bg(M_{K\pi}) \quad (5.5)$$

The mass parameter of the Breit-Wigner fit ( $M_0$ ) is left free within the fit range, which may vary for different  $p_t$  bins, without however being bigger than  $M_{PDG} - 1.6\sigma \leq M_{K\pi} \leq M_{PDG} + 3.5\sigma$ . Here  $M_{PDG}$  indicates the Breit-Wigner mass quoted by the PDG and  $\sigma$  is 2.35 times the resonance width,  $\Gamma_{PDG}$ . This range thus corresponds to  $M_{PDG} - 4.0\Gamma_{PDG} \leq M_{K\pi} \leq M_{PDG} + 8.0\Gamma_{PDG}$ . The lower edge has been chosen in such a way to avoid the fit of the steep descending slope of the distribution at low  $M_{inv}$ , resulting from the kinematical cuts on the daughters. The fitted width is fixed to the PDG value,  $\Gamma_0 = \Gamma_{PDG}$ . Depending on the centrality, the fit of the residual background has been performed with first (“poly1”), second (“poly2”), third (“poly3”) degree polynomial functions. A second and third degree polynomials both allow a better fit of the residual background shape for centralities up to 60%, while for the most peripheral bin the best result was achieved by using a second order polynomial. The result of the fit for  $1 \leq p_t \leq 10$  GeV/c ( $K^{*0} + \bar{K}^{*0}$ ) with a Breit-Wigner and a third degree polynomial is shown in fig. 5.10 for the 0 to 20% centrality bin.

The signal is then studied in 8  $p_t$  bins for each of the four centrality bins mentioned in section 5.1.1: 1.0–1.5, 1.5–2.0, 2.0–2.5, 2.5–3.0, 3.5–4.0, 4.0–5.0, 5.0–7.0, 7.0–10.0 GeV/c. Different solutions for the binning in  $p_t$  have been tried and in particular, the bins 5.0–6.0 and 6.0–7.0, as well as the 7.0–8.0 and 8.0–10.0 have been merged in order to increase the statistics, to reduce the statistical error and to attempt to extend the measurement to 10 GeV/c.

As a result of the fit, a measurement of the  $K^{*0}$  mass is provided as function of  $p_t$  for the different centralities, as shown in fig. 5.11 for the case in which  $bg(M)$

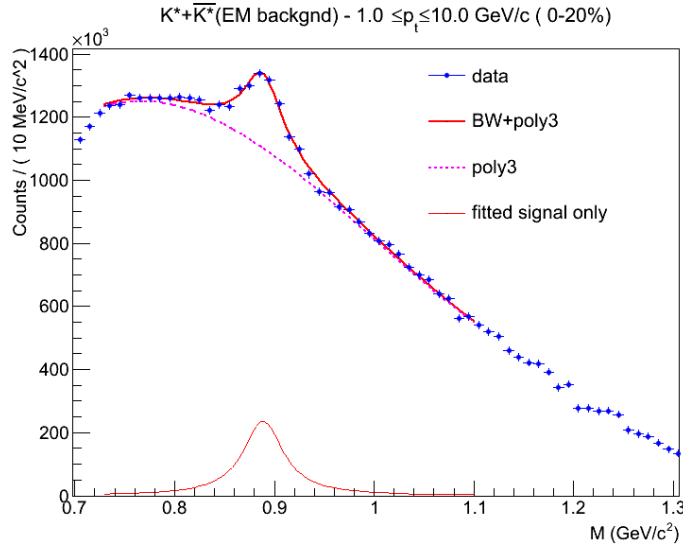


**Figure 5.10**  $K^{*0} + \bar{K}^{*0}$  signal with  $1.0 \leq p_t \leq 10.0$  GeV/c, in the 0 to 20 % centrality events, after subtraction of the event-mixing background. The signal is fitted with Breit-Wigner function, while the residual background is shaped via a third degree Chebychev polynomial (dashed line). The solid line represents the total fit function.

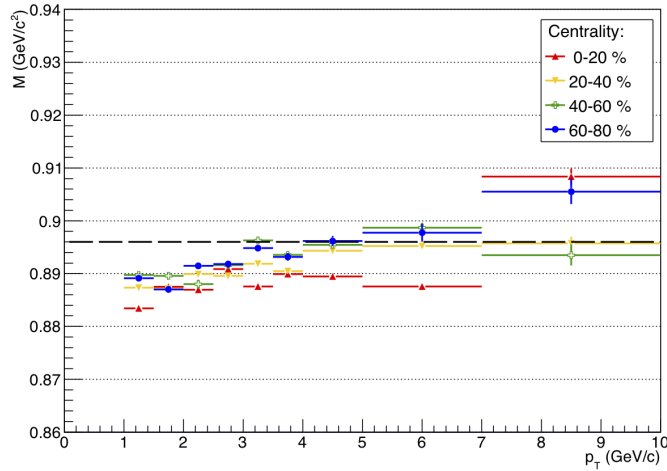


**Figure 5.11**  $K^{*0}$  mass obtained from the fit of the Breit-Wigner peak and a second degree polynomial residual background. Only the statistical error is reported. The black dashed line indicates the PDG value for the  $K^{*0}$  mass.

is a second degree polynomial and the fit range is  $0.74 \leq M_{inv} \leq 1.10$  GeV/c $^2$ . At low  $p_t$ , the mass is lower than the PDG value by <0.7% or <10 MeV/c $^2$ , as also measured in pp collisions [53]. This discrepancy is thought to be due to a detector effect and will be subject of future investigations. It however does not affect the measurement of the yield.

The  $K^{*0}$  raw yields have been extracted from the fit for the four centralities, as reported in fig. 5.12. For each bin, several fitting solutions have been attempted (see also 5.3). The best solution, defined by having  $\chi^2 \leq 2$  and the best visual agreement with the residual background shape outside the peak region, has been chosen to provide the raw yield measurement. The fit of the invariant mass distribution is shown at the end of the chapter for each centrality and  $p_t$  bin.

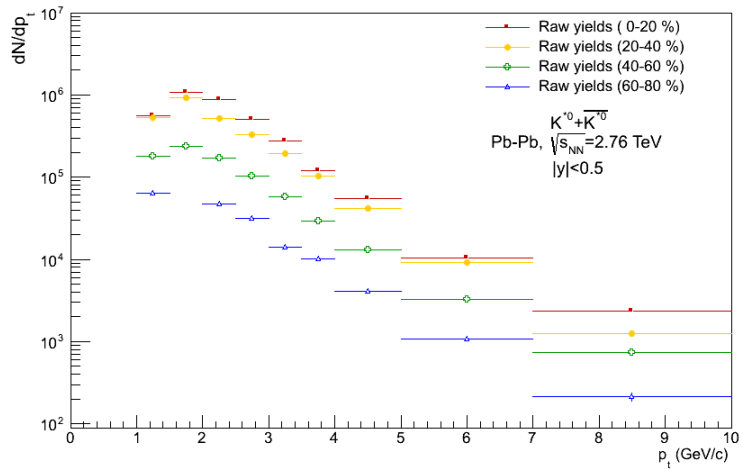


**Figure 5.12**  $K^{*0} + \bar{K}^{*0}$  raw spectra obtained from the fit of the Breit-Wigner peak and a Chebychev polynomial residual background for different centralities. Only the statistical error is reported.

## 5.2 Efficiency correction

The total  $K^{*0}$  efficiency is the product of three main contributions:

$$\epsilon_{tot} = (Acc \times \epsilon_{rec}(p_T) \times \epsilon_{K^{*0}}^{match} \times \epsilon_{PID}) \quad (5.6)$$

where

- $(Acc \times \epsilon_{rec})(p_t)$  is the  $p_t$ -dependent correction due to the detector acceptance ( $Acc$ ) and reconstruction efficiency ( $\epsilon_{rec}$ ), including the contribution of the tracking and candidates selection cuts (this is also referred to as TPC-only contribution);

- $\varepsilon_{K^{*0}}^{\text{match}}$  is the  $p_t$ -dependent TOF matching efficiency for the resonance, that is the convolution of the single-track matching efficiency of each daughter;
- $\varepsilon_{\text{PID}}$  is a constant factor that accounts for PID of the daughters performed with the  $n\sigma$ -cut strategy.

The  $p_t$ -dependent contributions to the efficiency, in particular, have been estimated from simulated HIJING [73] Pb–Pb events, where the detector response is simulated by GEANT3 [74]. The analysed production is anchored to the 2010 runs of the data analysis sample. The efficiencies shown for different centrality bins in the following have been obtained from the analysis of  $1.63 \times 10^6$  events selected with the same criteria of the data analysis, unless differently specified.

### Efficiency $\times$ acceptance

The efficiency  $\times$  acceptance ( $(\text{Acc} \times \varepsilon_{\text{rec}})(p_t)$ ) is defined as the ratio between the number of true reconstructed<sup>3</sup> and generated  $K^{*0}$  ( $G(K^{*0})$ ) and  $\bar{K}^{*0}$  ( $G(\bar{K}^{*0})$ ), which decay into charged  $K\pi$  pairs in the interval  $|y| < 0.5$ . The reconstructed tracks are selected through the standard quality cuts, the same as for the data. At this stage neither the TOF matching nor the PID cuts are applied. In other words, the true pairs are obtained as the  $K^+ \pi^-$  pairs produced by the decay of a  $K^{*0}$  ( $R_T(+-)$ ) or the  $K^- \pi^+$  pairs from the decay of a  $\bar{K}^{*0}$  ( $R_T(-+)$ ), where both daughters are detected within the detector acceptance and pass the standard track selection. The efficiency is then

$$\varepsilon(p_T) = \frac{R_T(+-) + R_T(-+)}{G(K^{*0}) + G(\bar{K}^{*0})} \quad (5.7)$$

The efficiency  $\times$  acceptance contribution, shown in fig. 5.13 is strongly  $p_t$ -dependent but independent of centrality.

The efficiencies for the  $K^{*0}$  ( $K^+ \pi^-$ ) and  $\bar{K}^{*0}$  ( $K^- \pi^+$ ) separately are shown in fig. 5.14 together with their ratio for the 0–20% and 40–60% centrality bins. The behaviour in the two centrality bins is similar. The most significative difference is of the order of 7% relative to the lowest  $K^{*0}$   $p_t$  bin,  $0 \leq p_t \leq 1$  GeV/c, that however is not considered for the analysis as the absolute value of the efficiency is only 10% and reduces to below 1% when the contribution of TOF matching is also included. In the  $1.0 \leq p_t \leq 1.5$  GeV/c bin, the difference between  $K^{*0}$  and  $\bar{K}^{*0}$  efficiency is about 3%, while in the interval  $1.5 \leq p_t \leq 2.5$  GeV/c it is compatible with unity within the statistical errors.

### TOF matching efficiency

The contribution of the TOF matching on the  $K^{*0}$  efficiency has been studied on a subsample of  $3 \times 10^5$  Pb–Pb events from the same Monte Carlo production men-

---

<sup>3</sup>The reconstructed pairs are identified as  $K^{*0}$  or  $\bar{K}^{*0}$  by using the Monte Carlo information of their PDG code.

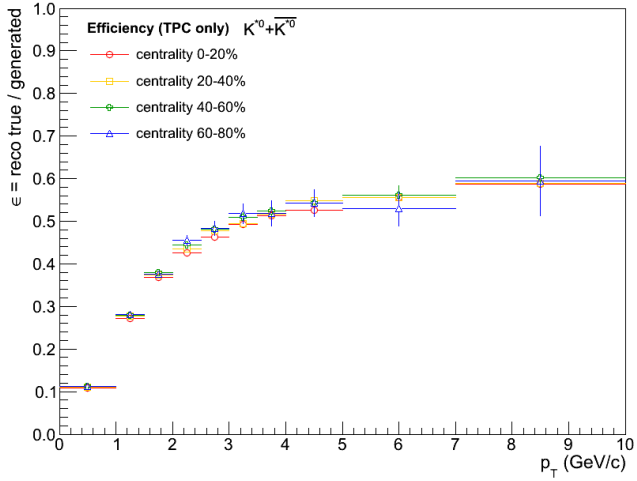


**Figure 5.13**  $K^{*0}$  and  $\bar{K}^{*0}$  efficiency per acceptance (tracking and selection cuts) for different centrality events, as estimated from a HIJING simulation anchored to 2010 Pb–Pb data.

tioned above. The  $K^{*0}$  matching efficiency ( $\epsilon_{K^{*0}}^{match}$ ) is defined as

$$\epsilon_{K^{*0}}^{match} = \frac{\text{true reconstructed pairs with both daughters matching TOF}}{\text{true reconstructed pairs}}. \quad (5.8)$$

It is  $p_t$ -dependent, as the single-track TOF matching efficiency, but it is not simply the direct product of two single-particle TOF matching efficiencies, because of the effect of the detector geometrical acceptance on the detection of both the resonance decay products.

In fig. 5.15 (top) the TPC-only efficiency (red) is compared with the efficiency calculated as  $(\text{Acc} \times \epsilon_{rec})$  but adding the request for TOF matching (blue) to the track selection cuts, for the 0-20% central events. One can see that the TPC-only efficiency is lowered by nearly half by the effect of the resonance TOF-matching efficiency alone, that is reported in fig. 5.15 (bottom). As expected the two-tracks matching efficiency reported there is lower than the typical value for the single-track matching efficiency in Pb-Pb collisions is about 70% for  $p_t \geq 1$  GeV/c and  $|\eta| < 0.8$  once that the TOF readout efficiency has been taken into account (see section 4.2).

The green curve in fig. 5.15 (top) represents the case in which the additional  $5\sigma$  cut on TPC PID is applied to reduce the mismatch. As already discussed in section 5.1.3, the mismatch cut has no particular effect at intermediate  $p_t$  and above, instead it is expected to play a bigger role at low  $p_t$  and in most central events where the track multiplicity is higher.

The total  $p_t$ -dependent contribution to the efficiency, that is  $(\text{Acc} \times \epsilon_{rec})(p_T) \times \epsilon_{K^{*0}}^{match}$ , is reported for all centrality bins in fig. 5.16.

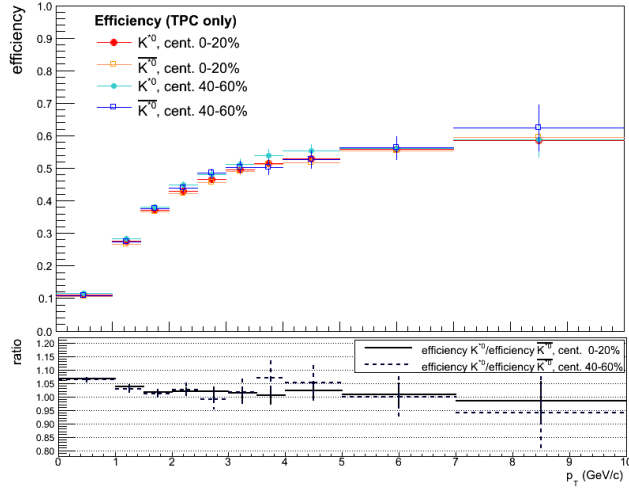


**Figure 5.14** Efficiency per acceptance (tracking and selection cuts) for  $K^{*0}$  and  $\bar{K}^{*0}$  separately (top) and their ratio (bottom), for events in the 0–20% and 40–60% centrality bins.

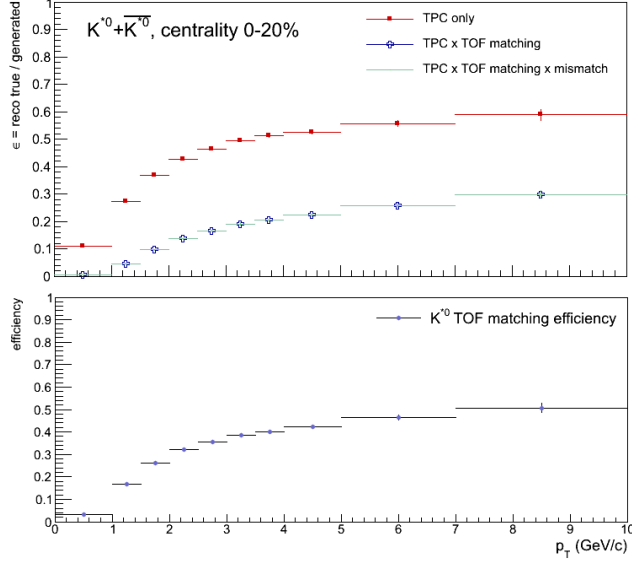


**Figure 5.15** Comparison between  $K^{*0}$  efficiency with and without TOF matching requirement (top) and TOF matching efficiency for  $K^{*0} + \bar{K}^{*0}$  (bottom). The matching efficiency for the  $K^{*0} + \bar{K}^{*0}$  is obtained as the ratio between the blue and red curve in the top histogram. The efficiency is shown for events in the 0-20% centrality bin.

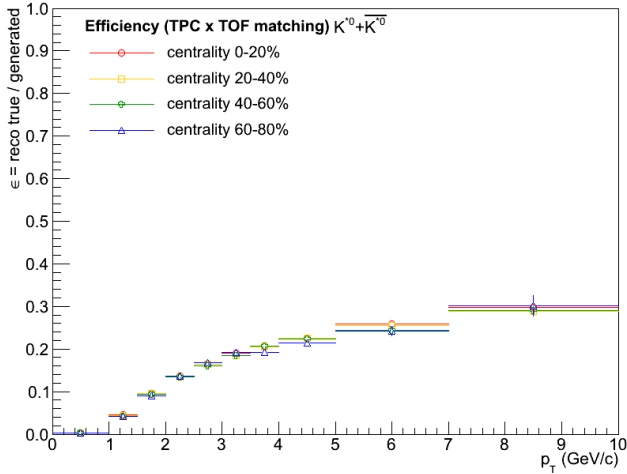


**Figure 5.16**  $K^{*0}$  and  $\bar{K}^{*0}$  efficiency for different centralities, as estimated from a HIJING simulation anchored to 2010 Pb–Pb data. The efficiency includes the efficiency per acceptance (tracking and selection cuts, TPC only) and the TOF matching requirement for both resonance daughters.

### PID correction factors

In order to obtain the total correction, the efficiency has to be scaled by a  $p_t$ -independent factor that accounts for the  $2\sigma$  cut on TOF signal and the  $5\sigma$  cut on TPC energy loss (mismatch cut) for the two daughters. This factor is  $\varepsilon_{PID} = \varepsilon_{PID,TOF} \times \varepsilon_{PID,TPC}$ , with  $\varepsilon_{PID,TOF} = 0.9594 \times 0.9594 = 0.911$  and  $\varepsilon_{PID,TPC} = 0.999 \times 0.999 = 0.9998$ , where the identification efficiencies for the two tracks are considered independent one from the other and therefore multiplied.

## 5.3 Systematic uncertainty on the yields

The measurement of  $K^{*0}$  yields have been checked for systematic effects related to the different steps of the analysis: the background estimation, the fitting procedure, the particle identification and the track selection. The main sources of systematic uncertainties are described in details below, while table 5.2 reports only a summary of the average contributions.

### 5.3.1 Systematic effects related to the yield extraction procedure

The systematic uncertainty related to the yield extraction procedure has been determined by repeating the fit for each centrality and  $p_t$  bin varying the function to fit the residual background and the fit range. Only results from fit with  $\chi^2/\text{dof} \leq 2$  have been considered. For each  $p_t$ , the available measurements obtained by vary-

Source	Syst. uncertainty (%)
Yield extraction: residual background	10
Yield extraction: fit range	5 ÷ 15
Background normalisation	2
Event mixing settings	5
Event mixing settings: reaction plane	3
Tracking	10
Material budget	4
TOF matching	8
PID	5

**Table 5.2** Contribution to the systematic uncertainty on the  $K^{*0}$  yield from various sources, expressed in percentile of the measured yield.

ing one fit setting at the time, are indicated by  $(y_i \pm \sigma_i)$ . Among these, the value closest to the weighted mean of the sample has been chosen as the “central value”, together with its error, and it is indicated as  $y_c \pm \sigma_c$ . In order to verify whether the difference  $(\Delta y)_i = y_c - y_i$  is due to a statistical or systematic effect [86], hence to subtract the statistical contribution from the uncertainty, the following variable is defined

$$\Delta_i = \sqrt{\sigma_i^2 - \sigma_c^2} \quad (5.9)$$

as the difference in quadrature of the statistical errors associated to each of the measurements (indexed with  $i$ ). Then one can compute  $n_i = (\Delta y)_i / \Delta_i$ , that indicates how much the difference is due to statistics. If  $n_i \leq 1.0$  there is no systematic effect, that is the two measurements are compatible within the statistical uncertainties. For this study, the measurements with  $n_i \geq 10.0$  have been discarded. Because every time that a measurement is removed from the sample, the weighted mean changes and the central value may shift, a recursive procedure has been applied to identify the best central value, while keeping only the reliable results. The systematic uncertainty has been determined as  $\delta y_c = (n_{max} - 1) \Delta_i$ , where  $n_{max}$  is the maximum among the  $n_i$  of the final sample.

It has been verified that the fit is very stable when changing within the fit range the allowed interval for the input Breit-Wigner mass parameter. No systematic uncertainty is associated to this effect, as the average shift of the output mass position is of the order of  $10^{-4}$ , compatible with the associated statistical error.

The fit function to shape the residual background has been chosen to be a second or a third degree Chebychev polynomial for the centrality classes 0–20%, 20–40% and 40–60%. For the most peripheral events, the best result was obtained using a second degree Chebychev polynomial and a Landau function has been used to evaluate the systematics. For brevity, in the following text the second and third degree Chebychev polynomials will be referred to as polynomials, or “poly2” and “poly3” respectively. The linear and the exponential functions have been discarded

because they do not reproduce satisfactorily the background shape and lead to a systematic overestimate of the yields for all bins with respect to the other functions.

For each fit function, the lower ( $m_{low}$ ) and upper ( $m_{up}$ ) edge of the fit range have been displaced respectively within  $0.7 \leq m_{low} \leq 0.78 \text{ GeV}/c^2$  and  $1.1 \leq m_{up} \leq 1.2 \text{ GeV}/c^2$ , corresponding to variations between 10% and 30% from the smallest invariant mass interval considered. For each  $p_t$  bin, a minimum of 3 and a maximum of 8 values of the yield have been compared to determine the systematic uncertainty. The systematic uncertainty is  $p_t$ -dependent and, in average, between 5 and 15 %.

An example of the fit with a second and third degree polynomial is shown in fig. 5.22 left. The ( $K^{*0} + \bar{K}^{*0}$ ) yields for the centrality class 20-40% obtained with poly2 and poly3 are also reported in fig. 5.22 right. Noteworthy is that for each bin the two functions have been compared by using the same fit range. The resulting spectra are compatible within <10%, and similarly for the other centrality bins.

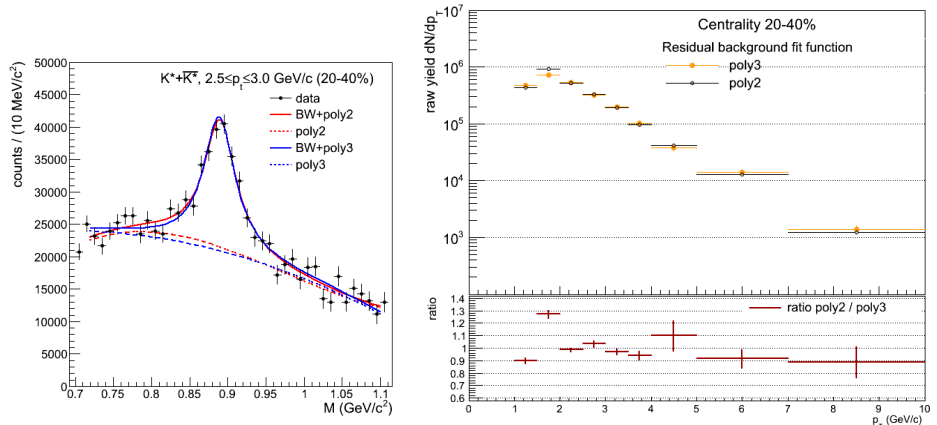


**Figure 5.17** ( $K^{*0} + \bar{K}^{*0}$ ) raw yield for centrality class 20-40% obtained with two different functions, Chebychev polynomials of second and third degree respectively, for the residual background. Only statistical errors are reported.

### 5.3.2 Systematic effects related to the background

A measurement of the yield for each centrality and  $p_t$  bin has been performed by varying independently each of the following settings for the event-mixing background estimation:

- event-mixing background normalisation range,
- number of mixed events,
- event plane binning.

In addition, the analysis has been performed by computing the like-sign background (like-sign pairs from the same event), as discussed in the next section more extensively.

In the final analysis the EM background has been normalised to the US distribution in the range  $1.3 \leq M_{inv} \leq 1.5 \text{ GeV}/c^2$ , as described in 5.1.4. The analysis has been repeated by reducing this interval to  $1.4 \leq M_{inv} \leq 1.5 \text{ GeV}/c^2$  to evaluate the presence of any possible systematic effect due to the choice of the normalisation range. The systematic uncertainty associated to this has been estimated to be 2%. The settings of the event mixing were checked for systematic effects by varying the number of events to be used to compute the background between 3 and 5. This difference affects the coefficients deriving from the normalisation of the EM distribution to the US. A difference of the order of 5% has been found between the raw yields, in each centrality class. Furthermore, the event mixing without using the

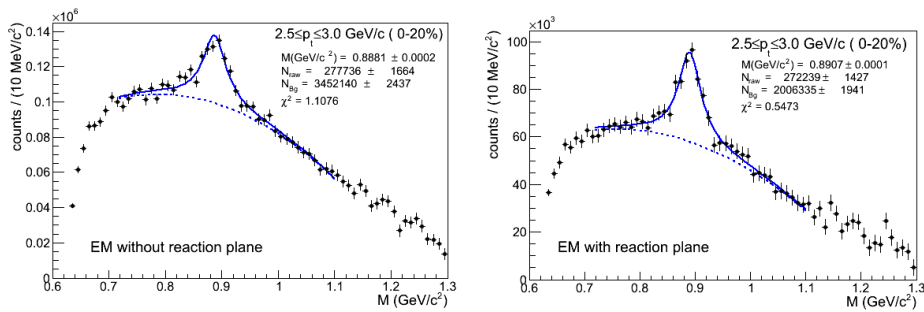


**Figure 5.18** Comparison between the  $K^{*0} + \bar{K}^{*0}$  signal after background subtraction in the 0-20% most central events and  $2.5 \leq p_t \leq 3.0 \text{ GeV}/c$ . The left plot is obtained after subtraction of the EM distribution where no selection on the reaction plane is applied or the events for the mixing. The right plot is obtained from EM background where the events in each mixing bin are required to satisfy  $\Delta\Psi_R=20^\circ$ . The measured raw yields differ of  $\sim 2\%$ , while the background under the signal peak is nearly twice as bigger when the reaction plane information is not used.

event plane information has been attempted. The EM technique implies that the events are grouped in similarity classes to mix only those with similar topology. The event plane information contributes to characterise the “shape” of the events and practically it results in an additional binning of the events. The raw spectra obtained with 5 mixed events when no event plane information is used and when a binning of  $\Delta\Psi_R=20^\circ$  is applied have been compared and found to differ of about 3%. The fitted signal after background subtraction for  $(K^{*0} + \bar{K}^{*0})$  with  $2.5 \leq p_t \leq 3.0 \text{ GeV}/c$  in the most central class is shown in the two cases in fig.???: when the reaction plane information is used, the background under the peak region is reduced by nearly a factor 2, improving the significance of the signal.

### Study on like-sign background

The like-sign (LS) technique for the background estimation has been used to perform a cross-check on the yield extraction.  $K^+ \pi^+$  and  $K^- \pi^-$  pairs from the same event have been built separately and then combined into a geometric mean<sup>4</sup>, according to the formula:

$$LS = 2\sqrt{y_{++}y_{--}}, \quad \delta LS = \sqrt{\frac{y_{++}^2(\delta y_{--})^2 + y_{--}^2(\delta y_{++})^2}{y_{++}y_{--}}}$$

where  $y_{\pm\pm}$  and  $\delta y_{\pm\pm}$  are the entries in each  $M_{inv}$  bin for the  $K^+ \pi^+$  and  $K^- \pi^-$  distributions and their statistical errors, respectively. The total like-sign background is not normalised.

The background from event-mixing has been preferred for the final analysis, because the LS background distribution leads to a depletion at low invariant mass after background subtraction. Since this effect has to be investigated and fully understood, the LS background is used as a check on the yield extraction for the most peripheral (60-80%) events only, where the effect is smaller compared to other centralities.

The result of the fit to the background-subtracted distribution is shown in fig. 5.19 for each  $p_t$  bin, while the raw yields with like-sign and event mixing technique are compared in fig. 5.20 for the most peripheral events. The spectra are compatible within 10% for  $p_t < 3.5$  GeV/ $c$  and within 20% above.

Despite the quite satisfactory outcome of the cross-check in the 60-80% centrality class, it has been chosen not to use the LS technique for the systematic error evaluation, since the background shape cannot be fully trusted for the signal extraction in most of the  $p_t$  and centrality bins.

### Tracking, PID and other systematic effect sources

The systematic uncertainty related to the tracking efficiency and the track selection (PID excluded) is known to be approximately 6% for single tracks, independent of  $p_t$  in the region of interest for this analysis. This has been estimated in various ALICE central barrel analysis that use the same single-track standard cuts (see for example [?]). This factor is doubled to account for the fact that two tracks are used to reconstruct each  $K^{*0}$  meson, for a total 12% effect. Similarly, a contribution to the systematic uncertainty of 4% per single track comes from the discrepancy between the TOF matching efficiency in data and Monte Carlo (see section 4.2), for a total 8% effect. From the  $\phi$  and  $K^{*0}$  meson analysis in pp collisions [53], a 4%  $p_t$ -independent systematic uncertainty must be considered to account for the contribution of the detector material budget in the central barrel.

Another source of systematic uncertainty is particle identification: besides the strategy chosen for the analysis, that is a  $2\sigma$ -cut on the TOF signal, the yield extraction

---

<sup>4</sup>The geometric mean helps minimising the bin-by-bin fluctuations due to the difference in the number of positively and negatively charged particles.

has been repeated by using a  $1.5\sigma$ -cut TOF PID. The extracted yields have been compared by fixing any other parameter (single-track non-PID cuts, settings for EM background, background normalisation range, fit function and range) and a 5% systematic uncertainty contribution has been found for most  $p_t$  bins and centrality. The ratios between the yields obtained with  $1.5\sigma$  and  $2.0\sigma$  PID cut are shown in fig. ?? for different centralities. As the only exception, a 30% difference is found for  $1.0 \leq p_t \leq 1.5$  GeV/c in the most central events. For this bin, this is the largest systematic effect and it may be a consequence of the contamination at low  $p_t$  by pions of the kaon sample.

The total systematic uncertainty is the quadrature sum of all the sources mentioned and summarised in table. 5.2.

## 5.4 $K^{*0}$ transverse momentum spectra

The raw yields shown in fig. ?? have been corrected for efficiency as described in section ???. The measured spectra for  $(K^{*0} + \bar{K}^{*0})/2$  are reported in figure 5.23. The statistical and systematic uncertainties are reported respectively as the error bars and the shaded rectangles on the plot. We notice that the measured points for central collisions (0-20% and 20-40%) for  $1.0 < p_t < 2.0$  GeV/c superimpose within the errors. It has to be considered that the systematic uncertainty for these points is large and the main contributions are the choice of the function used to shape the residual background and the PID. Considering in addition, that the total  $K^{*0}$  efficiency in these bins is low (below 10%), we have arguments to suggest a more detailed study of this momentum range with increased statistics.

As shown in section 1.3.2, a preliminary analysis of the  $K^{*0}$  production in Pb–Pb collisions has been carried out by exploiting the TPC PID only. That analysis provides a measurement of the resonance spectra in the  $p_t$  range  $0.15 < p_t < 5.0$  GeV/c, due to the limits of the particle identification via energy loss in the TPC. The analysis presented in this thesis was initially meant to understand the possible role of TOF PID in the identification of the resonance decay products, and in particular of the kaon. In central Pb–Pb collisions the extraction of the signal is particularly difficult, given the high particle multiplicity and the consequent large amount of combinatorial background. Particle identification cuts are of fundamental importance to reduce as much as possible this background. Given the actual performance of the TOF detector, the TOF PID has been demonstrated to be in fact a valid tool to help the  $K^{*0}$  signal reconstruction. Thanks to TOF PID, that allows  $\pi/K$  separation to higher momenta with respect to the TPC, it has been possible to attempt the measurement of the  $K^{*0}$  up to 10 GeV/c for four centrality classes, between 0 and 80%. The TPC measurement is still of fundamental importance in the low momentum range ( $p_t < 1$  GeV) where TOF cannot provide a measurement due to the fact that particles with  $p_t < 0.5$  GeV/c do not reach its surface. Future developments of the analysis include a measurement of the mass of the resonance with its systematic uncertainty and a refinement of the presented results. The possibility

of applying a more sophisticated PID selection that combines TOF and TPC will be also taken into consideration. The combination of this analysis with the TPC results will be also carried out in the superposition region, in view of a possible unified publication.

In conclusion, the TOF analysis of  $K^{*0}$  production reveals to be a good candidate to complement the existing TPC-only analysis by extending the  $p_t$  reach and improving the significance of the measurement.

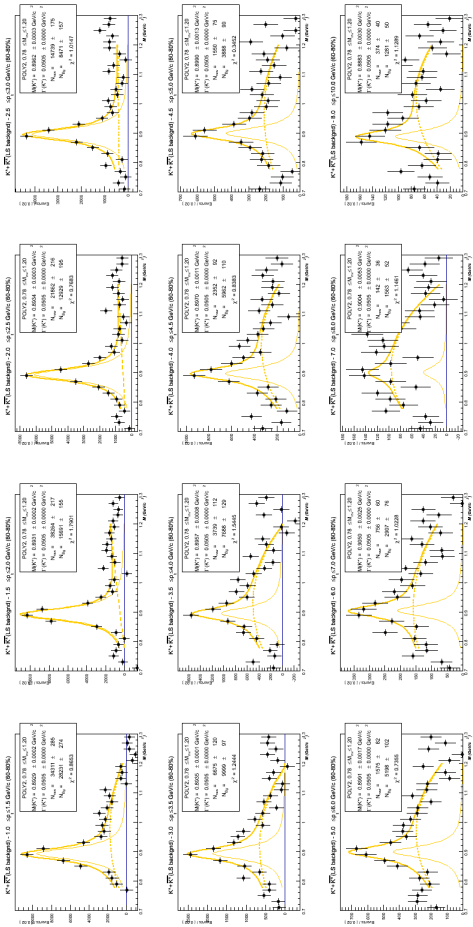


**Figure 5.19** Result of the fit on the like-sign background-subtracted invariant mass distribution (black points) with a non-relativistic Breit-Wigner for the signal (solid line) and a second degree polynomial (dashed line) to shape the residual background. The fit is performed for all  $p_t$  bins in the range  $0.74 \leq M_{inv} \leq 1.10$  GeV/c<sup>2</sup>. The Breit-Wigner width is fixed to the PDG value, and the width of each bin is 10 MeV/c<sup>2</sup>.

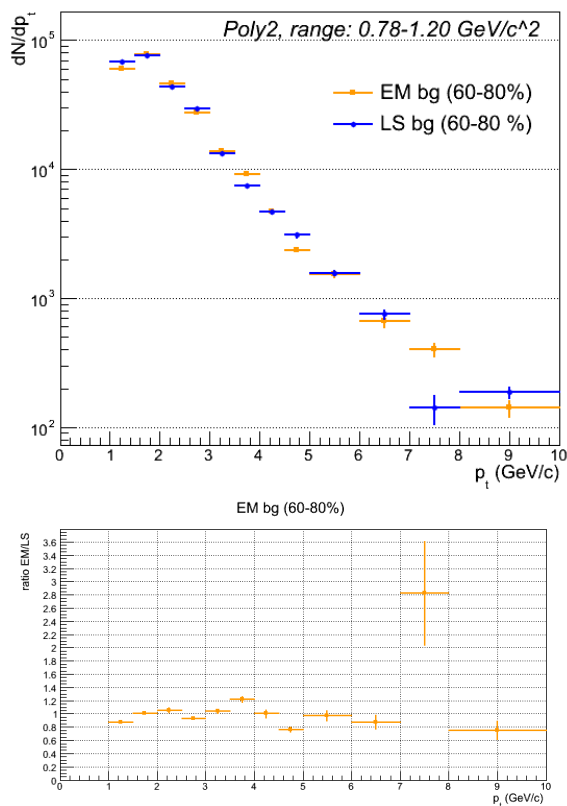


**Figure 5.20** Comparison between the  $K^{*0} + \bar{K}^{*0}$  raw yields in the 60-80% central events, obtained after subtraction of the like-sign background from the same event (blue line) and the unlike-sign background from the event mixing (orange line). On the bottom plot the ratio between the spectrum with like-sign and that from event mixing is reported.

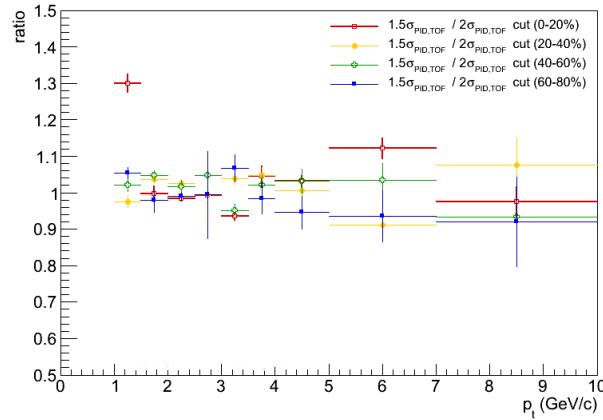


**Figure 5.21** Ratio between ( $K^{*0} + \bar{K}^{*0}$ ) raw yields obtained with  $1.5\sigma$  and  $2.0\sigma$  PID cut for all centrality classes.

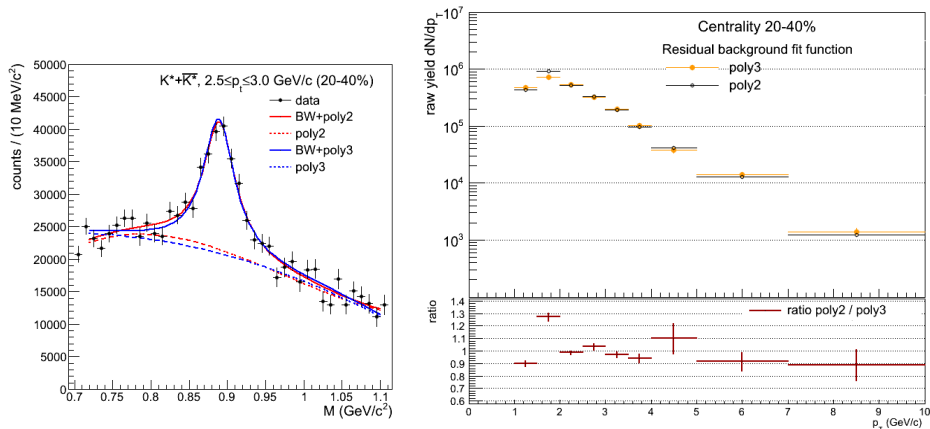


**Figure 5.22** ( $K^{*0} + \bar{K}^{*0}$ ) raw yield for centrality class 20-40% obtained with two different functions, Chebychev polynomials of second and third degree respectively, for the residual background. Only statistical errors are reported.

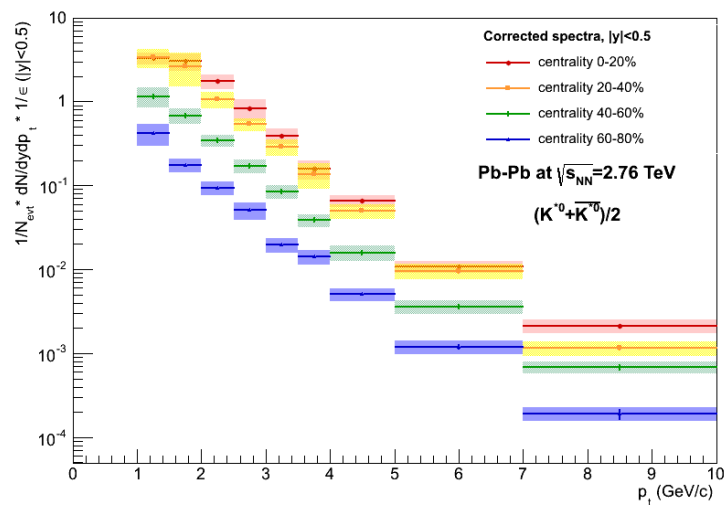


**Figure 5.23**  $(K^{*0} + \bar{K}^{*0})/2$   $p_t$  spectra corrected for efficiency and detector acceptance. The error bars (shaded areas) indicate the statistical (systematic) uncertainties.

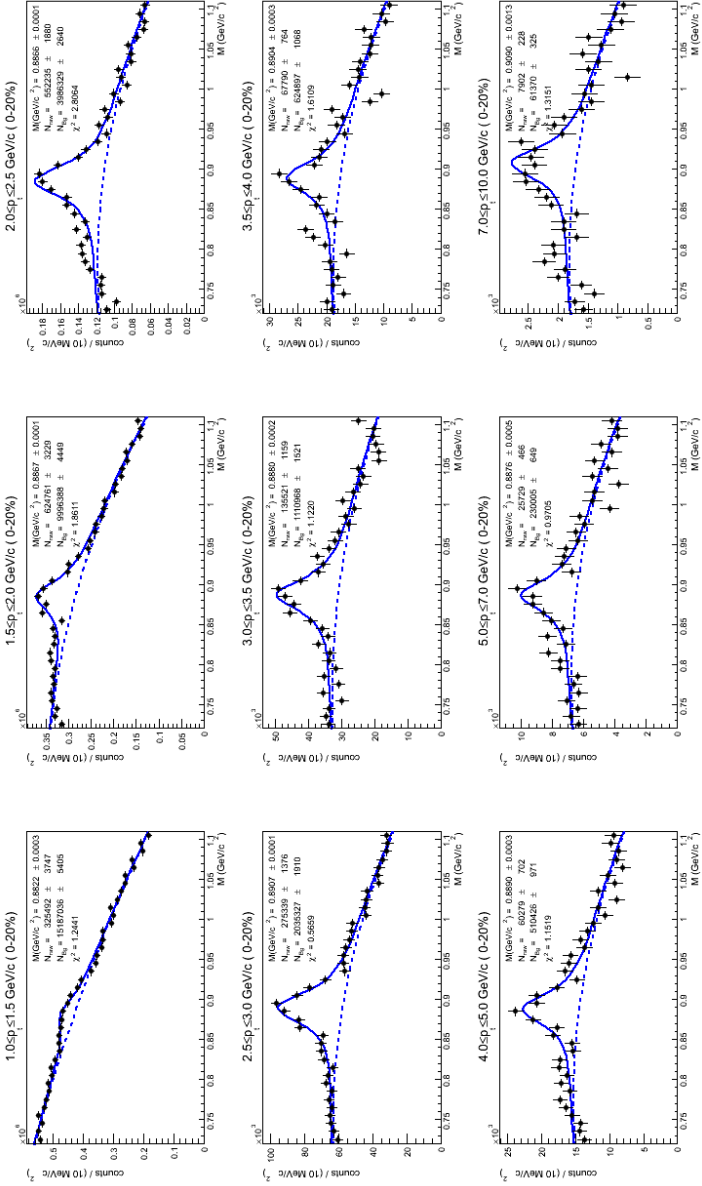


**Figure 5.24** Result of the fit to the  $K^{*0} + \bar{K}^{*0}$  signal and residual background for the 0-20% central events. The signal is shaped with a non-relativistic Breit-Wigner, while for the residual background a second order Chebychev polynomial is used.

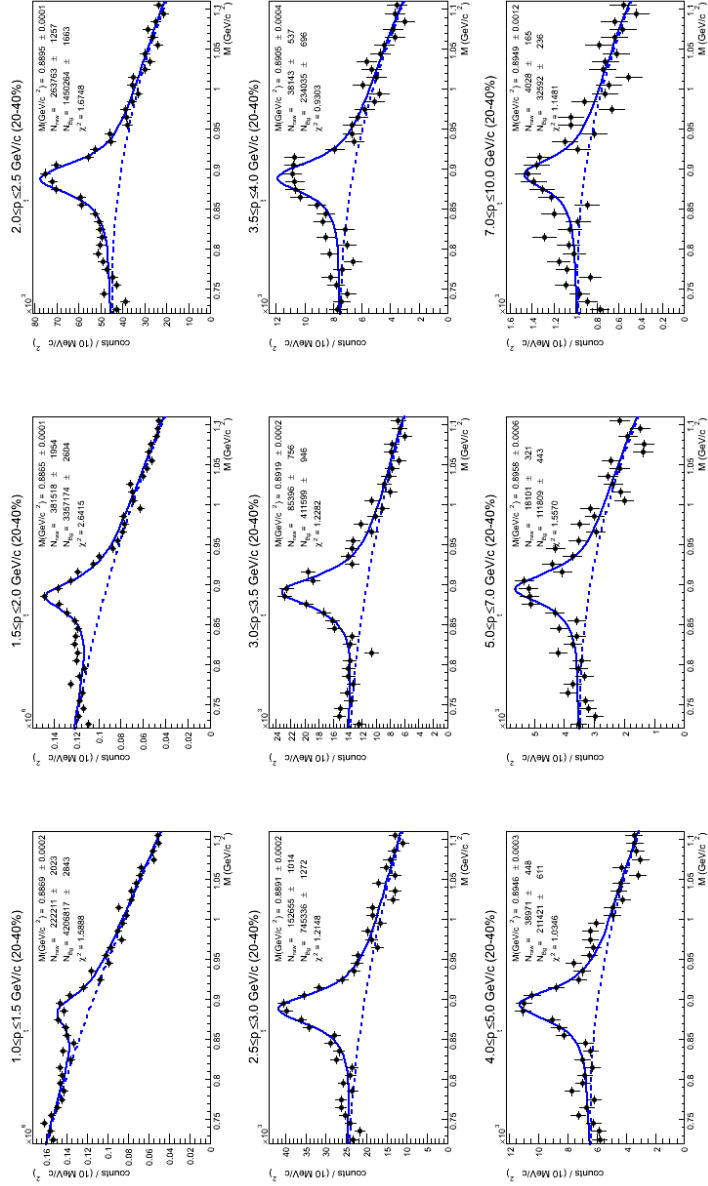


**Figure 5.25** Result of the fit to the  $K^{\ast 0} + \bar{K}^{\ast 0}$  signal and residual background for the 20-40% central events. The signal is shaped with a non-relativistic Breit-Wigner, while for the residual background a second order Chebychev polynomial is used.

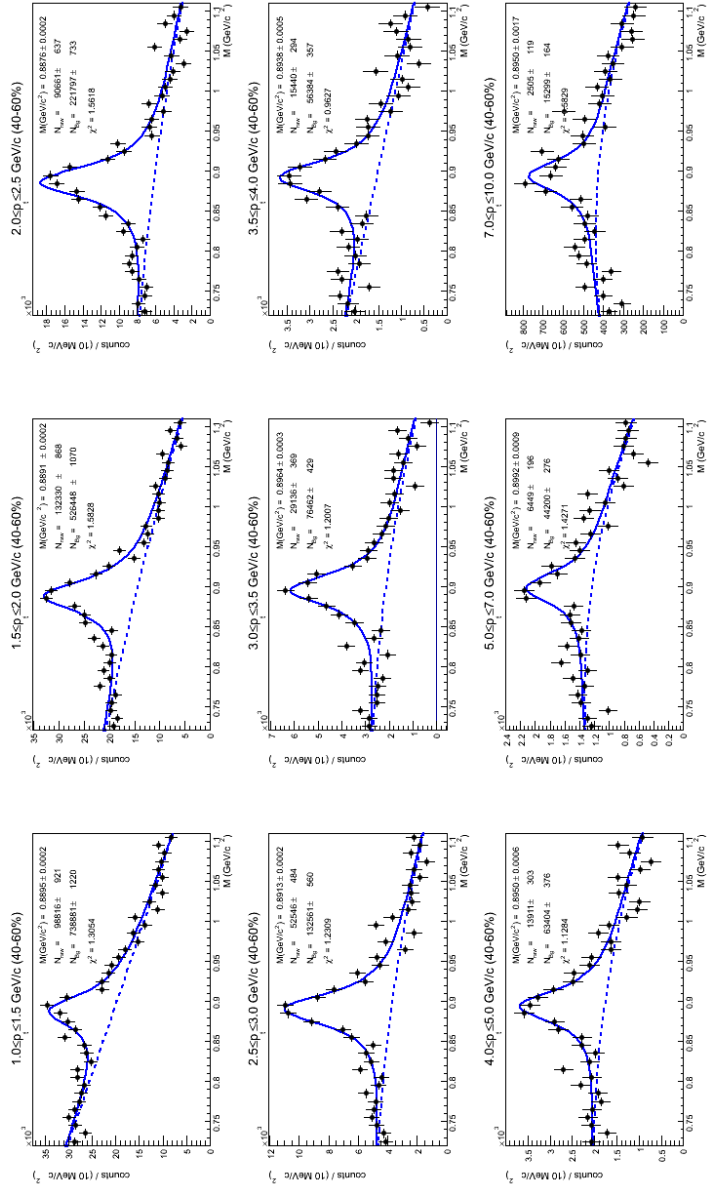


**Figure 5.26** Result of the fit to the  $K^{*0} + \bar{K}^{*0}$  signal and residual background for the 40-60% central events. The signal is shaped with a non-relativistic Breit-Wigner, while for the residual background a second order Chebychev polynomial is used.

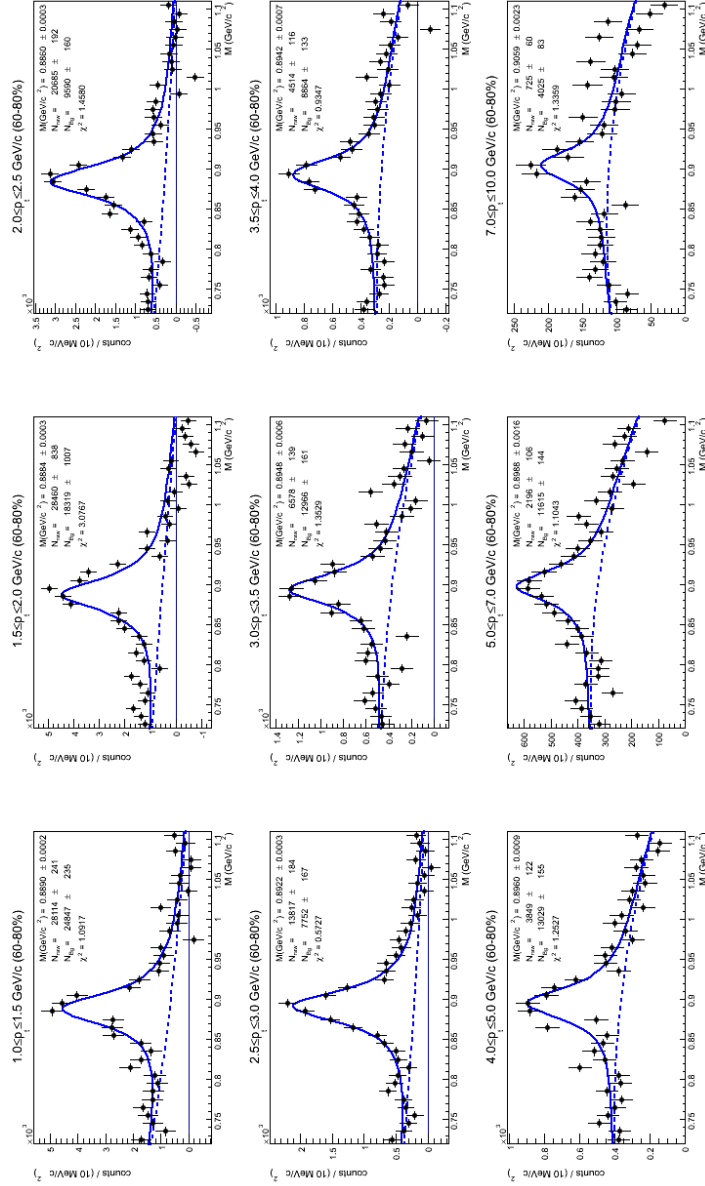


**Figure 5.27** Result of the fit to the  $K^{*0} + \bar{K}^{*0}$  signal and residual background for the 60-80% central events. The signal is shaped with a non-relativistic Breit-Wigner, while for the residual background a second order Chebychev polynomial is used.

# Conclusions

In this thesis the analysis of the  $K^*(892)$  resonance yield as function of transverse momentum in Pb–Pb collisions at  $\sqrt{s_{\text{NN}}} = 2.76$  TeV has been presented. The analysis is motivated by the interest in the measurement of short-lived resonances production that can provide insights on the properties of the medium produced in heavy-ion collisions both during its partonic and hadronic phase. This particular analysis exploits particle identification with the ALICE Time-Of-Flight detector, aiming to extend the reach of the resonance  $p_t$  spectrum measured by a preliminary analysis, where PID via energy loss measurement has been applied (TPC only).

After an introduction on the ALICE experiment, the focus has been on the Time-Of-Flight system. The aspects of calibration and data quality control have been discussed in detail, while illustrating the excellent and very stable performance of the system in different collision environments at the LHC. It has been shown that TOF PID allows a  $2\sigma$  separation between  $\pi$  and  $K$  up to  $3.0$  GeV/c, suggesting that the particle identification technique is well suited to be used in the study of the  $K^{*0} \rightarrow K^\pm \pi^\mp$  decay, where kaon identification is crucial.

The analysis strategy has been finally described in its stages. The signal is extracted via an invariant mass analysis. The combinatorial background is obtained with the event mixing technique and then subtracted from the unlike-sign pair distribution. The resonance signal appears as a peak sitting on a residual background. The signal and the residual background are appropriately fitted to extract the yields. The terms that contribute to the efficiency have been discussed in detail, as well as the main sources of systematic uncertainty. After applying the efficiency  $\times$  acceptance correction, the transverse momentum spectra of the  $K^{*0}$  have been reported in the range  $1.0 < p_t < 10$  GeV/c. Although not yet final, the results show that the analysis strategy discussed here, including TOF PID, is a valid tool to measure the  $K^{*0}$  up to intermediate momenta, complementary to the TPC-only analysis. Further developments of the analysis are planned, towards the combination of the two results and a final measurement for publication.



# Bibliography

- [1] J. Letessier, J. Rafelski, *Hadrons and Quark-Gluon Plasma*, Cambridge University Press, 2002
- [2] K. Gottfried, V. F. Weisskopf, *Concepts of particle physics, Vol. I-II*, Oxford University Press, 1984
- [3] K.G. Wilson, Phys. Rev. **D** 10, (1974) 2445.
- [4] O. Kaczmarek, F. Zantow, Phys. Rev. **D** 71 114510 (2005) [hep-lat/0503017].
- [5] P. Petreczky, J. Phys. G **39**, 093002 (2012) [arXiv:1203.5320 [hep-lat]].
- [6] V. Koch, *Aspects of Chiral Symmetry*, (2002)
- [7] A. M. Polyakov, Phys. Lett. B 72 (1978) 477.
- [8] R. D. Pisarski and F. Wilczek, Phys. Rev. D 29 (1984) 338.
- [9] J. Pearson, <http://www/jpoffline/com/physicsdocs/y3s6/nuclearphysiclsn.pdf>
- [10] Miller, M. L., Reygers, K., Sanders, S. J., and Steinberg, P. Ann. Rev. Nucl. Part. Sci. 57, 205-243 (2007).
- [11] Heinz, U. W. , arXiv:hep-ph/0407360v1 (2004)
- [12] Aamodt, K. e. a. Phys. Rev. Lett. 105, 252301 Dec (2010)
- [13] Phys. Rev. Lett. 106, 032301 (2011)
- [14] J. Rafelski and B. Muller, Phys. Rev. Lett. 48, 1066 (1982)
- [15] Rafelski, J., Letessier, J., and Torrieri, G. Phys.Rev. C64, 054907 (2001)
- [16] Tounsi, A. and Redlich, K. (2001), arXiv: 0111159[hep-ph]
- [17] Armesto N, et al., J.Phys.G 35:054001 (2008), 0711.0974.
- [18] PHOBOS Collaboration, Back BB, et al., Nucl. Phys. A757:28 (2005), nucl-ex/0410022.

- [19] BRAHMS Collaboration, Arsene I, et al., Nucl. Phys. A757:1 (2005), nucl-ex/0410020.
- [20] PHENIX Collaboration, Adcox K, et al., Nucl. Phys. A757:184 (2005), nucl-ex/0410003.
- [21] STAR Collaboration, Adams J, et al., Nucl. Phys. A757:102 (2005), nucl-ex/0501009.
- [22] A. Andronic *et al.*, Nucl. Phys. A 772 (2006), 167.
- [23] C. Shen, U. W. Heinz, P. Huovinen, and H. Song, Phys. Rev. C 84, 044903 (2011).
- [24] Y. Karpenko and Y. Sinyukov, J. Phys. G: Nucl. Part. Phys. 38, 124059 (2011).
- [25] P. Bozek, Phys. Rev. C85, 034901 (2012), arXiv:1110.6742 [nucl-th]
- [26] B. I. Abelev *et al.* (STAR Collaboration), Phys. Rev. C 79, 034909 (2009).
- [27] S. S. Adler *et al.* (PHENIX Collaboration), Phys. Rev. C 69, 034909 (2004).
- [28] S. Bass *et al.*, Prog. Part. Nucl. Phys. 41, 255 (1998).
- [29] B. Abelev *et al.* (ALICE Collaboration), arXiv:1208.1974v1 [hep-ex], *to appear in Phys. Rev. Lett.*
- [30] E. Schnedermann, J. Sollfrank and U. W. Heinz, Phys. Rev. C 48, 2462 (1993).
- [31] M. Nicassio, Acta Phys. Polon. Supp 5, 237 (2012).
- [32] A. Andronic *et al.*, Phys. Lett. B 673, 142 (2009).
- [33] E. Andersen *et al.* (WA97 Collaboration), Phys. Lett. B 449, 401 (1999).
- [34] F. Antinori *et al.* (WA97/NA57 Collaboration), Nucl. Phys. A 698,118c (2002)
- [35] B. I. Abelev *et al.* (STAR Collaboration), Phys. Rev. C 77, 044908 (2008)
- [36] J. Adams *et al.* (STAR and STAR-RICH Collaborations), arXiv:0601042 [nucl-ex]
- [37] S. Schuchmann (ALICE Collaboration), J. Phys. G: Nucl. Part. Phys. 38 (2011) 124080
- [38] I. Belikov (ALICE Collaboration), J. Phys. G: Nucl. Part. Phys. 38 (2011) 124078

- [39] R. C. Hwa and B. C. Yang, Phys. Rev. C 75, 054904 (2007)
- [40] Abelev, B. et al. (ALICE Collaboration), (2012) arXiv:1205.5761[nucl-ex ]
- [41] Adams, J. et al. (STAR Collaboration) Phys.Rev. C72, 014904 (2005)
- [42] Aamodt, K. et. al. (ALICE Collaboration), Phys. Rev. Lett. 105, 252302 Dec (2010)
- [43] Horowitz, W. and Gyulassy, M. Nucl.Phys. A872, 265-285 (2011)
- [44] Aamodt, K. et. al. (ALICE Collaboration), Phys. Rev. Lett. 107, 032301 Jul (2011)
- [45] Voloshin, S. Nucl.Phys. A715, 379-388 (2003)
- [46] Molnar, D. and Voloshin, S. A. Phys.Rev.Lett. 91, 092301 (2003)
- [47] Bass, S., Dumitru, A., Bleicher, M., Bravina, L., Zabrodin, E., et al. Phys.Rev. C 60, 021902 (1999)
- [48] Torrieri, G. and Rafelski, J. Phys.Lett. B 509, 239-245 (2001).
- [49] Markert, C., Torrieri, G., and Rafelski, J. , 533-552 (2002).
- [50] C. J. Beringer et al. (Particle Data Group), Phys. Rev. **D** 86, 010001 (2012)
- [51] Markert, C., Bellwied, R., and Vitev, I. Phys.Lett. B669, 92-97 (2008).
- [52] Renk, T., Schneider, R., and Weise, W. Phys. Rev. C 66, 014902 Jul (2002).
- [53] Abelev, B. et al. Eur. Phys. J. C 72, 2183 (2012).
- [54] Sjostrand, T., Mrenna, S., and Skands, P. (2006).
- [55] Singha, S. (ALICE Collaboration) (2012), arXiv:1211.0187[hep-ex]
- [56] Knospe, A. (ALICE Collaboration) (2013), arXiv:1301.1644 [nucl-ex]
- [57] O. S. Broning et al., *LHC Design Report*, (2004)
- [58] L. Evans (ed.), P. Bryant (ed.), JINST 3, S08001 (2008)
- [59] CERN, *Report on the 18 spetember incident at the LHC*, (2008)
- [60] M. Lamont, *Comparison of integrated luminosities*, Chamonix (2010)
- [61] J. M. Jowett et. al., *First run of the LHC as a heavy ion collider*, CERN, (2011).
- [62] Aamodt, K. et. al. JINST 3, S08002 (2008).

- [63] Carminati, F. E. et al. (ALICE Collaboration), *ALICE: Physics performance report, volume I*, J. Phys. G30, 1517-1763 (2004).
- [64] LHC Tech. Proposal, (1995) *ALICE: technical proposal for A Large Ion Collider Experiment at the CERN LHC*, CERN (1995)
- [65] *ALICE DATE V3.5 User's Guide* ALICE-INT-1999-46. CERN, Geneva, (1999).
- [66] Zampolli, C., Carminati, F., and Colla, A. (ALICE Collaboration), PoS ACAT2010, 066 (2010).
- [67] Chapeland, S. and Roukoutakis, F. Journal of Physics: Conference Series 119(2), 022017 (2008).
- [68] Von Haller et al. (ALICE collaboration), B. Journal of Physics: Conference Series 219(2), 022023 (2010).
- [69] Brun, R. and Rademakers, F. , Nucl. Instr. Meth. A: 389(12), 81-86 (1997).
- [70] Gaspar, , Gaspar, C., and Donszelmann, M. In CERN - DELPHI 94-4 DAS 148, 811, (1993).
- [71] <http://aliweb.cern.ch/Offline/>
- [72] Saiz, P. et. al (ALICE Collaboration), Nucl. Instr. and Meth. A: 502(2-3), 437-440(2003).
- [73] Wang, X.-N. and Gyulassy, M. Phys.Rev. D44, 3501-3516 (1991).
- [74] <http://wwwasd.web.cern.ch/wwwasd/geant/index.html> (1993)
- [75] S. Agostinelli et al., Nucl. Instr. and Meth A 506(3), 250 - 303 (2003).
- [76] A. Fass et al., <http://www.slac.stanford.edu/econf/C0303241/proc/papers/MOMT004.PDF>
- [77] Billoir, P. Computer Physics Communications 57(1-3), 390-394 (1989).
- [78] B. Batyunya, a. Y. B. and Safarik, K. (1997), ALICE-INT-97-24 (1997).
- [79] Bruna, E., Dainese, A., Masera, M., and Prino, F., ALICE Internal Note 2009-018, Nov (2009).
- [80] Caffarri, PhD thesis, Scuola di Dottorato di Ricerca in Fisica dell'Università di Padova, (2011).
- [81] Rossi, A. PoS VERTEX2010, 017 (2010).
- [82] Cortese, P. et al. (2000). *ALICE: technical design report of the Time Of Flight system (TOF)*, CERN-LHCC-2000-012 (2000)

- [83] E. Cerron Zeballos et al., Nucl. Instr. and Meth A 374(1), 132-135 (1996).
- [84] Akindinov, A., Alici, A., Antonioli, P., Arcelli, S., Baek, Y., et al., Nucl. Instr. Meth. A602, 658-664(2009).
- [85] Akindinov, A. et. al., Nucl. Instrum. Meth. A602, 709-712 (2009).
- [86] R. Barlow, hep-ex/0207026.